

# The dynamic response of a Hyperloop tube embedded in soft soils

Author: J.(Jun) Yuan  
Date: 29 - Nov - 2018



*[This page intentionally left blank]*

# The dynamic response of a Hyperloop tube embedded in soft soils

---



By

J.(Jun) Yuan

In partial fulfillment of the requirements for the degree of

**Master of Science**  
in Structural Engineering

at Delft University of Technology  
to be defended publicly on 29 November, 2018

## THESIS COMMITTEE

University Supervisors:	Prof.dr.A. (Andrei) Metrikine	TU Delft
	Dr.ir. K.N. (Karel) van Dalen	TU Delft
	Ir.M.(Mingjuan) Zhao	TU Delft
	Dr.ir. C.B.M. Blom	TU Delft
Company Supervisors:	Ir.H.(Herke) Stuit	Movares
	Ir.O.(Olivier) Louis	Movares

## AUTHOR INFORMATION

Author: Jun YUAN                      Student Number: 4622693  
Tel.Number: +31 (0)6 49178986      Email Address: yuanjun902@gmail.com

© November 2018, Jun Yuan, Delft, the Netherlands

This report is confidential and cannot be made public until 29 November 2019

A digital version of this thesis is available at <http://repository.tudelft.nl>

*[This page intentionally left blank]*

## Acknowledgements

The research is conducted as my thesis of MSc. specialized in Structural Engineering in the faculty of Civil Engineering and Geosciences at Delft University of Technology, collaborating with Movares Nederland B.V. The sections of Structural Mechanics, Concrete Structures and the Department of Dynamics from Movares have taken care of the supervision.

In my graduation committee, I would like to thank Prof. Andrei Metrikine, for his valuable opinions and suggestions, Kees, for teaching me to look at problems with a strong logic and with a great enthusiasm, Herke, for offering me the opportunity to carry out my research at Movares. I want to thank Karel, for enhancing my understandings of the methods used in the thesis and providing valuable feedback. I am greatly indebted to my daily supervisor from the university, Mingjuan, for her investment of a large amount of time to discuss almost every detail of the thesis, and her patience in constantly guiding me throughout the whole thesis process. Also, I am greatly indebted to my daily supervisor from Movares, Olivier, for his innovative advice in tackling my thesis problems, and more importantly, for teaching me to relate numerical models to the physics.

In addition, I would like to thank my colleagues at Movares, for overcoming the language barrier and the kindness in treating me as one of their colleagues. Especially, I want to express my gratitude to the whole modeling group, without which I would not be able to achieve my work.

Lastly, I would like to thank my family for their silent support on my master study in the Netherlands, and my friends for sharing the joys and sorrows. I want to thank my girlfriend for the company and support throughout the research period.

J.(Jun) YUAN  
Delft, November 2018

*[This page intentionally left blank]*

## Abstract

The hyperloop system is a new transportation mode, which consists a magnetic levitating capsule-like hyperloop pod and a vacuum tube. Due to small air hindrance, the hyperloop pod is conceived to have a maximum speed of 333 m/s. If such a hyperloop system is to be built underground in soft soils, the hyperloop speed can easily reach the wave propagation speeds in the soil. Strong wave radiation is expected when the hyperloop is travelling at wave propagation speeds, which are called the critical speeds.

The first objective is to analyse the dynamic influence from the hyperloop. A linear elastic half-space with an infinitely long concrete tunnel buried at a certain depth has been modeled. The excitation of the system is a hyperloop modeled as a moving constant load acting at the tunnel invert. In this thesis, a so-called indirect boundary element method (BEM) is applied. Indirect boundary integrals are formed which rely on the fundamental solutions for the interior medium, the two-and-a-half dimensional Green's functions. These 2.5D Green's functions are essentially the steady state solutions of the half-space subjected to a spatially varying line load. The space is assumed to be infinitely long and invariant in the direction parallel to the axis of the tunnel.

Before implementing the BEM model, two improvements have been made to the 2.5D Green's functions: a better convergence of the Green's function surface-related terms and a better satisfaction of stress-free boundary conditions at the free surface. The accuracy and correctness of the boundary element model using the improved Green's functions have been verified by intensive case studies. Firstly, the scattering of 3D harmonic seismic P waves by a cavity and a tunnel in a linear elastic half-space is analysed. Results are validated by comparing to those from literature. Secondly, the BEM model is employed for the moving load problem. The embedded concrete tunnel is modeled using the Donnell's theory for thin shells. A coupled form of the indirect boundary integrals is formulated. Using the same model parameters, the results obtained by the BEM are in good agreements with those from literature. Moreover, a parametric study has been conducted to study the effect of moving load velocity, tunnel depth and thickness of concrete lining on the dynamic response.

As a second objective of the current thesis work, the BEM model is compared with a finite element method (FEM) based model, developed by Movares B.V. The models are compared in both accuracy and computational efficiency. In the FEM model, the moving load is considered as a series of consecutive short pulses. The contributions from all the pulses are synthesized using a convolution. Furthermore, since the space is invariant in the direction parallel to the tunnel axis, it is possible to apply just one stationary impulse load in the finite element model. Using this method, a constant moving load and a moving load with acceleration are modeled. The FEM results are found to have close agreements with those by the BEM. Besides the Rayleigh wave speed in the soil, a second critical velocity which is related to the wave propagation in the tunnel is found. Furthermore, the case where a hyperloop runs constantly at the Rayleigh wave speed is more crucial than the case where the hyperloop accelerates and passes the Rayleigh wave speed.





# Contents

<b>Acknowledgements</b>	<b>v</b>
<b>Abstract</b>	<b>vii</b>
<b>1 Introduction</b>	<b>1</b>
1.1 Background . . . . .	1
1.2 Problem statement . . . . .	1
1.3 Research questions . . . . .	3
1.4 Research design . . . . .	3
1.4.1 Research scope . . . . .	3
1.4.2 Research approach . . . . .	4
1.4.3 Report structure . . . . .	5
<b>2 Methods of solution</b>	<b>7</b>
2.1 Indirect boundary element method . . . . .	7
2.1.1 Idea . . . . .	7
2.1.2 Indirect boundary integrals . . . . .	9
2.2 Fundamental solution - 2.5D Green's functions . . . . .	11
2.2.1 Green's functions for a full-space . . . . .	11
2.2.2 Green's functions for a half-space . . . . .	13
2.2.3 Preliminary checks . . . . .	16
2.3 Donnell theory for thin cylindrical shells . . . . .	20
2.3.1 Governing equations . . . . .	20
2.3.2 Green's functions for thin cylindrical shells . . . . .	23
2.4 Summary . . . . .	26
<b>3 Model validation: scattering of P waves by a tunnel embedded in a half-space using indirect BEM</b>	<b>27</b>
3.1 A cavity embedded in a half-space . . . . .	27
3.1.1 Model, governing equations and boundary conditions . . . . .	27
3.1.2 Formulation using indirect BEM . . . . .	28
3.1.3 Convergence tests and results . . . . .	30
3.2 A tunnel embedded in a half-space . . . . .	34
3.2.1 Model, governing equations and boundary conditions . . . . .	34
3.2.2 Half-space domain . . . . .	36

3.2.3	Cylindrical shell domain . . . . .	37
3.2.4	Results . . . . .	38
3.3	Summary . . . . .	41
<b>4</b>	<b>Dynamic response of an embedded tunnel in a half-space subjected to a Hyperloop pod running in the tunnel by indirect BEM</b>	<b>43</b>
4.1	Model description . . . . .	43
4.2	Formulation using indirect BEM . . . . .	44
4.2.1	Loading condition . . . . .	44
4.2.2	Boundary and interface conditions . . . . .	44
4.2.3	Half-space domain . . . . .	46
4.2.4	Cylindrical shell domain . . . . .	46
4.2.5	Coupling equations of the shell and soil medium . . . . .	46
4.3	Frequency domain and time domain response . . . . .	48
4.3.1	Frequency domain . . . . .	48
4.3.2	Time domain . . . . .	49
4.4	Convergence tests and validation . . . . .	50
4.4.1	Convergence tests . . . . .	50
4.4.2	Check of interface conditions . . . . .	51
4.4.3	Validation . . . . .	52
4.4.4	Parametric study . . . . .	55
4.4.5	Full-space approximation . . . . .	63
4.5	Summary . . . . .	66
<b>5</b>	<b>Dynamic response of an embedded tunnel in a half-space subjected to a Hyperloop pod running in the tunnel by FEM</b>	<b>67</b>
5.1	Finite element model . . . . .	67
5.1.1	Model description . . . . .	67
5.1.2	Model parameters . . . . .	68
5.2	The modeling of moving loads . . . . .	71
5.2.1	Stationary impulse loads . . . . .	71
5.2.2	Convolution for constant moving loads . . . . .	74
5.2.3	Convolution for accelerating moving loads . . . . .	76
5.3	Results obtained by the FEM . . . . .	77
5.3.1	Hyperloop a constant speed . . . . .	77
5.3.2	Comparison between FEM and BEM . . . . .	82
5.3.3	Hyperloop with an acceleration . . . . .	89
5.4	Summary . . . . .	93
<b>6</b>	<b>Discussions and Conclusions</b>	<b>95</b>
6.1	Result discussions . . . . .	95
6.2	Limitations . . . . .	99
6.3	Future recommendations . . . . .	99
	<b>References</b>	<b>102</b>

<i>CONTENTS</i>	xi
<b>Appendices</b>	<b>103</b>
<b>A 2.5D Green's functions for a half-space</b>	<b>105</b>
A.1 Full-space terms . . . . .	105
A.1.1 Displacements . . . . .	105
A.1.2 Strains and stresses . . . . .	106
A.2 Surface terms . . . . .	107
<b>B Free field formulations under incident P waves</b>	<b>109</b>
<b>C Convergence tests</b>	<b>111</b>



# List of Figures

1.1	Hyperloop prototype from Elon’s proposal [1] . . . . .	1
1.2	Wave propagation of a conventional high-speed train system[2] . . . . .	3
1.3	Flowchart of the main thesis work . . . . .	6
2.1	Wave field composition . . . . .	7
2.2	The scattered field produced by a number of sources (in red) . . . . .	8
2.3	Sinusoidal harmonic line load acting at the origin of: (a)a full-space; (b)a half-space . . . . .	11
2.4	Wavenumber spectra for the displacement surface term $G_{yy}^{\text{surf}}$ . . . . .	17
2.5	Symmetry property of Green’s functions . . . . .	19
2.6	Coordinate system for three-dimensional cylindrical shell equations showing (a) the principle direction for a piece of shell element; (b) the corresponding displacement components and (c) the corresponding surface traction components . . . . .	20
2.7	(a) In-plane flexural modes corresponding to radial displacement $w$ ; (b) in-plane extensional modes corresponding to tangential displacement $v$ ; and (c) out-of-plane flexural modes corresponding to longitudinal displacement $u$ . [3] . . . . .	22
2.8	Schematic representation of hoop stress $\sigma_{\theta\theta}$ , longitudinal stress $\sigma_{zz}$ and shear stress $\sigma_{zz}$ on a shell element . . . . .	24
3.1	Schematic representation of a cylindrical tunnel embedded in a homogeneous half-space subjected to oblique incident P waves: (a) cross-section of the model; (b) vertical incident angle; (c) horizontal incident angle . . . . .	28
3.2	Normalized radial displacement at the cavity $ U_{r1} $ for different number of sources and receivers . . . . .	30
3.3	Normalized displacement (a) $ U_x $ , (b) $ U_y $ and (c) $ U_z $ at the half-space surface $y = 0$ with a cavity . . . . .	31
3.4	Normalized displacement (a) $ U_{r1} $ , (b) $ U_{\theta1} $ , (c) $ U_z $ and hoop stress $ \Sigma_{\theta1\theta1} $ at the cavity surface $r_1 = R_1$ . . . . .	32
3.5	Normalized displacement $ U_z $ at the cavity surface $r_1 = R_1$ using different number of sources and receivers ( $N_s =$ number of sources, $N_o =$ number of observations) . . . . .	33

3.6	Schematic representation of a cylindrical cavity embedded in a homogeneous half-space subjected to oblique incident P waves: (a) cross-section of the model; (b) vertical incident angle; (c) horizontal incident angle . . .	34
3.7	(a) Position to be occupied by a shell in the half-space; (b) Green's functions for a shell . . . . .	35
3.8	Traction equilibrium and net loading on the shell . . . . .	36
3.9	Normalized displacements: (a) $ U_x $ , (b) $ U_y $ and (c) $ U_z $ at half-space surface $y = 0$ with a tunnel . . . . .	38
3.10	Normalized displacements: (a) $ U_x $ , (b) $ U_y $ and (c) $ U_z $ at the tunnel-soil interface $r = r_o$ . . . . .	39
3.11	Normalized stresses: (a) hoop stress $\Sigma_{\theta\theta}$ at tunnel centerline $r = a$ , (b) longitudinal stress $\Sigma_{zz}$ at tunnel centerline $r = a$ , (c) hoop stress $\Sigma_{\theta\theta}$ at tunnel-soil interface $r = R_2$ from tunnel side, (d) hoop stress $\Sigma_{\theta\theta}$ at tunnel-soil interface $r = R_2$ from soil side . . . . .	40
4.1	Schematic representation of a 3D half-space with an embedded tunnel . . .	43
4.2	(a) Position to be occupied by a shell in the half-space; (b) Green's functions for a shell . . . . .	45
4.3	Traction equilibrium and net loading on the shell . . . . .	47
4.4	Convergence test of $Re\{U_r\}$ at soil-tunnel interface for different number of receivers considering different frequencies and hyperloop speed: (a) $f_0 = 0.2$ Hz , $V = 30$ m/s; (b) $f_0 = 20$ Hz , $V = 50$ m/s . . . . .	50
4.5	Convergence test for amplitude of vertical velocity at point A for different number of receivers considering frequency up to 100 Hz ( $V = 150$ m/s) . . .	51
4.6	$Re\{U_r\}$ at the soil-tunnel interface from the soil side and from the tunnel side for $f_0 = 0.2$ Hz , $c = 30$ m/s . . . . .	51
4.7	Amplitude spectrum comparison of the velocity response at point A due to a moving constant load ( $V = 30$ m/s) . . . . .	52
4.8	Time domain comparison of velocity response at point A on the half-space surface due to a moving constant load ( $V = 30$ m/s) . . . . .	53
4.9	Frequency spectrum comparison for velocity response at point A due to a moving constant load ( $V = 75$ m/s) . . . . .	54
4.10	Time domain comparison of velocity response at point A on the half-space surface due to a moving constant load ( $V = 75$ m/s) . . . . .	54
4.11	Stresses at tunnel invert for subcritical case $V = 30$ m/s and critical case $V = 75$ m/s: (a) hoop stress; (b) longitudinal stress . . . . .	55
4.12	Amplitude spectrum of the vertical displacement response at tunnel invert for different hyperloop speeds . . . . .	56
4.13	Amplitude spectrum of the vertical velocity response at tunnel invert for different hyperloop speeds . . . . .	57
4.14	Amplitude spectrum of the vertical velocity responses at the surface point A for different hyperloop speeds . . . . .	58
4.15	Amplitude spectrum of the vertical velocity response at the free surface point A . . . . .	59

4.16	Amplitude spectrum of the velocity response at the ground surface point A in the case of a shallow tunnel $H = 1.5 R_2$ for $V = c_R, c_s$ and $c_p$ . . . . .	60
4.17	Amplitude spectrum of the velocity response at the ground surface point A in the case of a deep tunnel $H = 10 R_2$ for $V = c_R, c_s$ and $c_p$ . . . . .	60
4.18	Maximum velocity response at the ground surface with varying tunnel depths . . . . .	61
4.19	Stresses at tunnel invert for different tunnel wall thickness ( $V = 30\text{m/s}$ ): (a) hoop stress; (b) longitudinal stress . . . . .	62
4.20	Maximum velocity response at the ground surface with varying lining thickness ( $V = 30\text{m/s}$ ) . . . . .	63
4.21	Amplitude spectra of vertical velocity at tunnel invert for different tunnel depths ( $V = 72 \text{ m/s}$ ) . . . . .	64
5.1	Finite element model . . . . .	68
5.2	Original problem and transformed problem . . . . .	72
5.3	Position and time history of the impulse load . . . . .	74
5.4	Impulse responses exactly at tunnel invert under the load (tunnel modeled using solid elements) . . . . .	77
5.5	Impulse responses exactly at tunnel invert under the load (tunnel modeled using shell elements) . . . . .	78
5.6	Impulse responses at tunnel invert $z < 30\text{m}$ at time instant $t = 0.012\text{s}$ . . . . .	78
5.7	Time domain response of vertical velocity $V_y$ at point A ( $V = 75\text{m/s}$ ) to show (a) effect of time record length; (b) effect of time step ; (c) effect of element size and (d) effect of model length . . . . .	79
5.8	Time domain response of vertical velocity $V_y$ at point A ( $V = 1000\text{m/s}$ ) to show (a) effect of time record length; (b) effect of time step ; (c) effect of element size and (d) effect of model length . . . . .	81
5.9	Time domain comparison of velocity response at point A for different hyperloop velocities (FEM using solid elements) . . . . .	82
5.10	Time domain comparison of velocity response at point A for different hyperloop velocities (FEM using shell elements) . . . . .	83
5.11	Maximum velocity response at point A versus hyperloop speed $V$ . . . . .	85
5.12	Time domain comparison of displacement response at tunnel invert for different hyperloop velocities (using solid elements) . . . . .	86
5.13	Time domain comparison of displacement response at tunnel invert for different hyperloop speeds (using shell elements) . . . . .	87
5.14	Maximum displacement response at tunnel invert versus hyperloop speed $V$ . . . . .	88
5.15	Schematic representation of an accelerating hyperloop . . . . .	89
5.16	Time domain response of vertical displacement at tunnel invert due to an accelerating hyperloop . . . . .	90
5.17	Maximum response of displacement at the tunnel invert (a) with varying acceleration and (b) the corresponding velocity at the observation . . . . .	91
5.18	Maximum vertical displacement at tunnel invert due to an accelerating hyperloop . . . . .	92

C.1	Convergence tests for the real part of radial displacement ( $V = 50$ m/s)	111
C.2	Convergence tests for the real part of radial displacement ( $V = 75$ m/s)	111
C.3	Convergence tests for the real part of radial displacement frequency component ( $V = 100$ m/s) at frequencies: (a) $f = 5$ Hz; (b) $f = 20$ Hz . . . .	112
C.4	Convergence tests for the real part of radial displacement frequency component ( $V = 150$ m/s) at frequencies: (a) $f = 20$ Hz; (b) $f = 50$ Hz . . .	112
C.5	Convergence tests for the real part of radial displacement frequency component ( $V = 200$ m/s) at frequencies: (a) $f = 20$ Hz; (b) $f = 50$ Hz . . .	112
C.6	Convergence tests for the real part of radial displacement frequency component at $V = 300$ m/s . . . . .	113
C.7	Convergence tests for the real part of radial displacement frequency component ( $V = 600$ m/s) at frequencies: (a) $f = 50$ Hz; (b) $f = 100$ Hz . . . . .	114
C.8	Convergence tests for the real part of radial displacement frequency component ( $V = 800$ m/s) at frequencies: (a) $f = 50$ Hz; (b) $f = 100$ Hz . . . . .	114
C.9	Convergence tests for the real part of radial displacement frequency component ( $V = 1000$ m/s) at frequencies: (a) $f = 50$ Hz; (b) $f = 100$ Hz . . . . .	114



# List of Tables

1.1	Typical soil type and shear wave speed in the Netherlands . . . . .	2
2.1	wavenumber values for different velocities . . . . .	16
2.2	stresses at the half-space surface: normal font size denotes the original method; bold font size denotes the improved method . . . . .	18
4.1	Material parameters . . . . .	44
5.1	Material parameters . . . . .	71

*[This page intentionally left blank]*

# Chapter 1

## Introduction

### 1.1 Background

As technology progresses, engineers strive to develop new type of transport modes. Hyperloop is one of the possibilities expected to be the fifth transport mode, after planes, trains, cars and boats. The idea was initially invented by George Medhurst, a British mechanical engineer, in the 18th century. With the updated technology and latest intelligence at hand, the hyperloop idea is now being gradually realized. The hyperloop system is a structure consisting of a hyperloop pod inside a partially vacuum tube. The hyperloop pod is supported by magnetic repulsion and hence does not touch the ground. Due to zero hindrance from the air, the hyperloop pod is capable of travelling at extremely high speeds, which is even faster than airplanes. The prototype of a hyperloop pod quoted from Elon's 57-page white paper is shown in figure 1.1. In the paper [1], the hyperloop pod is conceived to have an average speed of around 600 mph (miles per hour, equal to 970 km/h) and a maximum speed of 760 mph (1200 km/h).

### 1.2 Problem statement

From previous researches on super fast trains, an intense vibration occurs when trains are running at high speeds. As a consequence, the vibration has a great influence on

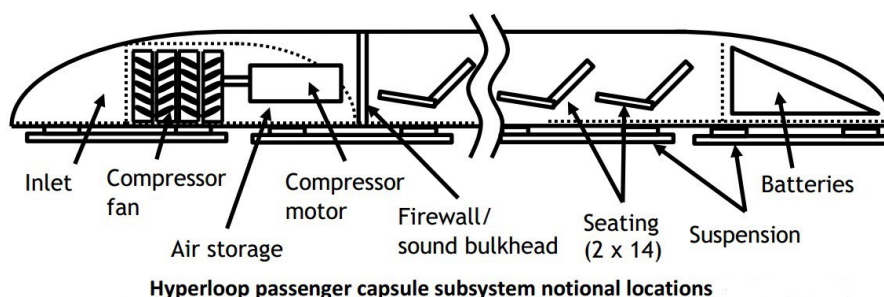


Figure 1.1: Hyperloop prototype from Elon's proposal [1]

human as well as on the environment. For example, instability of the train itself brings great discomfort to the passengers sitting inside. The vibration is annoying to human comfort once the horizontal and vertical acceleration levels are higher than  $0.5 \text{ m/s}^2$  and  $0.10 \text{ m/s}^2$ , respectively [4]. What's worse, horizontal and vertical acceleration levels of  $4.9 \text{ m/s}^2$  and  $9.8 \text{ m/s}^2$  respectively will even cause a dynamic soil settlement in granular and sandy soil [5].

When the hyperloop is moving, waves are generated and radiated from it with a certain speed. If the hyperloop velocity is lower than the wave propagation speeds, waves are simply travelling away from the source and die out within a certain distance, which are called evanescent waves. However, if the hyperloop is travelling at a velocity which is equal to or even larger than this wave speed, strong wave radiation effect can occur, causing a large displacement in the surrounding medium. The corresponding velocity of the hyperloop is referred to the critical velocity. In real life, it once happened that at a location near Ledsgard, Sweden where the Rayleigh wave velocity in the ground was as low as  $45 \text{ m/s}$ , the increase in train speed from  $140$  to  $180 \text{ km/h}$  has led to an amplification by a factor 10 in the generated ground vibration level [6]. Similar phenomenon could take place in the Netherlands where the soil is very soft, meaning that the shear wave speed is also low. Three types of typical soil are listed in table 1.1 with corresponding shear wave speeds.

Type	Peat	Clay	Sand
$c_s[\text{m/s}^2]$	50	75	200

*Table 1.1: Typical soil type and shear wave speed in the Netherlands*

The strong wave radiation effect can easily happen if the hyperloop system is to be built in the Netherlands. The hyperloop pod has a maximum speed of  $270 \text{ m/s}$ , meaning that it can reach and pass the critical speed during normal operation. The case that hyperloop breaks the elastic wave barrier in the soil generates strong vibration. For this reason, we would like to investigate the dynamic response of the tunnel. In the end, we hope to find out how the tunnel will react at the critical velocities, and whether the ground vibration level is too large due to the hyperloop pod, which could be of value for the design of the concrete tunnel.

In order to do so, the finite element method (FEM) and the boundary element method (BEM) will be applied. Because the BEM has the main advantage of automatically satisfying the radiation condition at infinity in the finite or semi-finite soil media, it may be a better tool for the problem at hand. It is also interesting to investigate the performance of the FEM which uses the discrete pulse approximation.

## 1.3 Research questions

There are two main objectives of the current thesis:

1. Investigating the dynamic response of a concrete tunnel embedded in the soft soil due to the excitation of a hyperloop;
2. Making a comparison between the boundary element method and the finite element method, in terms of result accuracy and calculation time.

Throughout this thesis, the following research questions will be answered:

- (1) What are the dynamic responses of the tunnel and in the ground, especially in critical cases?
- (2) What are the factors which can influence the responses?
- (3) Which scenario is more crucial, a hyperloop traveling at critical speeds, or a hyperloop that accelerates and breaks the elastic wave barriers?
- (4) What are the performances of the boundary element method and the finite element method?

## 1.4 Research design

### 1.4.1 Research scope

This part limits this thesis to a certain scope, within which the thesis work is carried out. The wave propagation by a hyperloop pod can be comparable to that by a conventional high-speed train to some extent as shown in figure 1.2. The transmission path is:

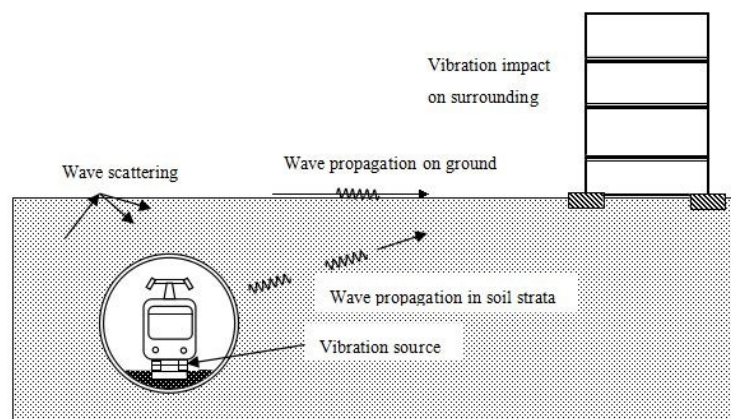


Figure 1.2: Wave propagation of a conventional high-speed train system[2]

- (1) waves are generated from the hyperloop; (2) the wave energy is transmitted to the supporting track; (3) from the track to the concrete tunnel; (4) from the tunnel to the surrounding soil; (5) from the subsoil to upper structures such as residence buildings and

other superstructures. According to the emphasis of our problem, some of the aspects just mentioned may be fully considered, or neglected or only partially taken into account. For the problem at hand, we specify the research objects which are involved:

### **Source**

As we know, loads can be applied on the underground tunnel system in the form of external loads (from the top of the ground surface), seismic waves (from below) or internal loads (at the tunnel invert). Moving objects in the tunnel generate waves which radiate away from it. There are various models for modelling the excitation sources, depending on the emphasis of the problem. The dynamic response of the system can be very different if the moving load is either constant, harmonic or even random in time. Throughout the thesis, the moving load is assumed to have a constant magnitude which does not vary in time. We take into account the hyperloop gravity force only.

### **Tunnel**

The tunnel is conceptualised as an infinitely long, thin cylindrical shell surrounded by the soil, and are characterized by the material property of concrete. It would have been more realistic if the interaction between tracks and the tunnel is considered. However, it is out of the thesis scope. Moreover, the connection between the tunnel and the soil is assumed to be perfectly bonded. No voids in between are assumed and no soil-structure behaviour is considered. This could suggest the vibration in the tunnel is overestimated in the situation where the soil is resonating. Because the tunnel is stiffer in material and suppresses the soil from vibrating.

### **Soil**

Soil often behaves nonlinearly and shows anisotropic and time dependent material behaviour. To simplify the model, here, the soil is modelled using the wave equations for linear elastic continuum. A full contact between soil and structure at their interface is assumed. The viscoelastic material behaviour can be easily incorporated in the frequency domain by using complex Lamé constants. Although the anisotropic character of the soil especially different soil properties in the vertical direction is interesting, it is not modeled considering the difficulty in establishing the coupled boundary integrals for the shell and layered soil. In this thesis work, for simplification, homogeneous soil is considered.

## **1.4.2 Research approach**

As stated before, the finite element method and the boundary element method will be applied in this thesis.

### **The finite element method (FEM)**

The FEM is the most common numerical method for analysing structures, very flexible in dynamic analysis with complex material properties and geometric structures. Interaction between different material or structures can be easily taken into account. Unlike the BEM, interior discretization is required for the FEM. In order to model a half-space with a finite geometry, artificial boundaries have to be assigned. The radiation effect at the infinity is modeled by either using extensive and uneconomical meshes or expensive non-reflecting boundaries. In the meantime, at positions close to the tunnel, small size elements have to be used to ensure accuracy. These two reasons often lead to a long

calculation time.

Stuit *et al* [7] adopted a static model, a track model and a wave propagation model to study dutch subway vibration propagation and analysed the influence of cell size, soil parameters and boundary conditions in FEM analysis software (ANSYS and LS-DYNA). In this thesis work, the stated wave propagation model will be adapted for calculation.

### **The boundary element method (BEM)**

The boundary element method shows unique advantages in solving the problem at hand: it requires only a boundary discretization and automatically take into account the radiation condition at infinity in the semi-infinite soil medium. As a consequence, the use of the BEM results in a matrix equation of a much smaller size than that of the FEM. For frequency domain BEM, the governing equations are static-like and are easy to employed. When the BEM is used for solving problems with irregularities in geometry of material, either a more complicated version of Green's function should be used or an interior subdivision of the domain is needed [8].

The use of 2.5D Green's functions together with boundary formulation is very powerful for the study of wave scattering, radiation and interaction in elastodynamics. The well-known singularity problems of Green's functions can be avoided by placing sources and receivers slightly deviated from each other. Luco *et al* [9] first obtained the steady-state response in a multi-layered viscoelastic half-space generated by a buried or surface point load moving with a constant speed. Furthermore, in combination with 2.5D Green's function, the 3D seismic response of a canyon, a tunnel and a valley for obliquely incident P-, SV- and SH waves were studied by indirect boundary element method[10, 11, 12].

Kausel and Tadeu [13] presented a fully analytical solution for the steady-state response for 3D homogeneous full space subjected to a spatially sinusoidal, harmonic line load. Later, in conjunction with discrete wave number method [14], the 2.5D Green's functions for a half-space were developed [15]. A variety of 2.5D Green's functions based on the same ideology were also developed for other purposes. Results obtained by using these 2.5D Green's functions have shown a great accuracy and a high efficiency. Therefore, incorporating these 2.5D Green's functions into the boundary element formulation to solve our problem at hand is of interest.

In this thesis, indirect boundary integrals are formulated in the frequency domain, in conjunction with the 2.5D Green's functions for a half-space.

### **1.4.3 Report structure**

This thesis report is divided into 6 chapters.

Chapter 1 explains the background of the research and states the problem of interest. Research goals and research questions are established to be kept in mind during the whole process of the thesis work. In the end, the research scope and approach are specified.

Chapter 2 mainly describes the theories to be used for the indirect boundary element method. It begins with the formulation of the indirect form of boundary integrals. Then, the two-and-a-half dimensional Green's functions for a half-space are presented, with firstly the full-space Green' functions and then the surface-related terms. Thereafter, the Donnell's theory for a thin shell is presented.

Chapter 3 is for the verification of the BEM model. The model is adapted to analyse the scattering of 3D harmonic seismic P waves. Two cases are considered: an embedded hollow cavity and an embedded concrete tunnel. The dynamic response of the half-space is explicitly analysed.

Chapter 4 employs the BEM to analyse the hyperloop problem. Results are firstly verified by comparing to literature. Then, the dynamic response of a half-space with an embedded tunnel due to the an hyperloop is investigated. By conducting a parametric study, the influencing factors of the response are investigated.

Chapter 5 focuses on the modeling using the FEM. The theory of convolution, and the way the stationary impulse load is applied are discussed. Thereafter, the moving load problem is analysed and results are compared to those by the BEM. The performance of the FEM model is explicitly analysed. Furthermore, the critical velocity of the hyperloop running in the tunnel is investigated.

The final chapter presents the discussions of the results and conclusions of the whole thesis work, where research questions are answered. Limitations and recommendations for future are also discussed.

The following flowchart summarizes the main thesis work:

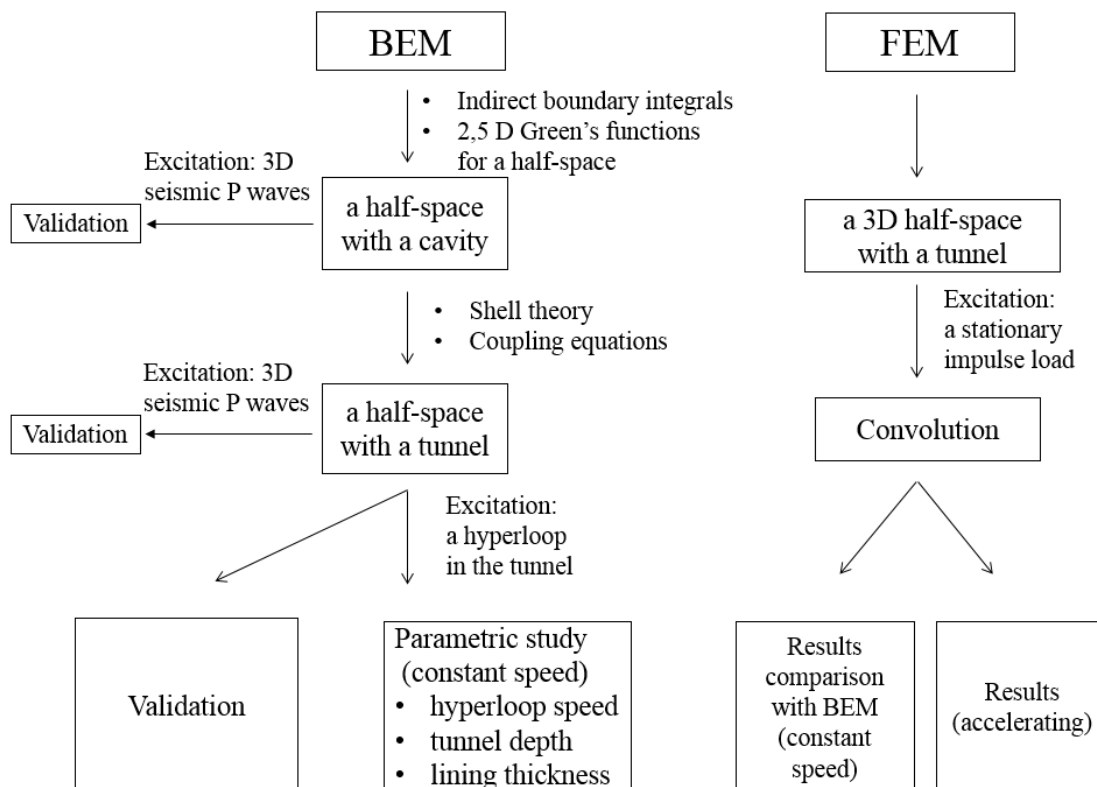


Figure 1.3: Flowchart of the main thesis work



# Chapter 2

## Methods of solution

### 2.1 Indirect boundary element method

#### 2.1.1 Idea

The boundary element method transforms partial differential equations to integral equations and it attempts to fit boundary values into the integral equation. The most widely used boundary integral has two basic forms, the direct boundary integral and the indirect boundary integral. The direct boundary integral employs the idea of reciprocity in elastic continuum: two admissible elastodynamic states can be associated with its own set of time-invariant parameters and its own set of loading conditions. Starting from the equation of equilibrium for two states in the continuum, applying the constitutive law and doing the integral considering time-harmonic relation, one could write down the explicit form of direct boundary integral. This integral relates the stress and displacement. The direct boundary integral has the advantages of obtaining the response by just solving one integral equation. However, in this thesis, the other form of boundary integral method(indirect) is used [10]. The indirect boundary integral method can be understood with a strong physical meaning: any form of loading that exerts on the system can be represented by a couple of sources with known positions but unknown amplitudes. These sources can be seen as equivalent loads and let the system have the same response as the original loading. Once the unknown amplitude of these sources have been found, with the help of transfer functions, the response elsewhere in the system can be easily obtained.

The procedure to solve seismic wave field using the indirect boundary element method is described in the following. As shown in the figure 2.1, a homogeneous half-space with a cavity is subjected to seismic waves. The radius of the cavity is  $R_1$ .

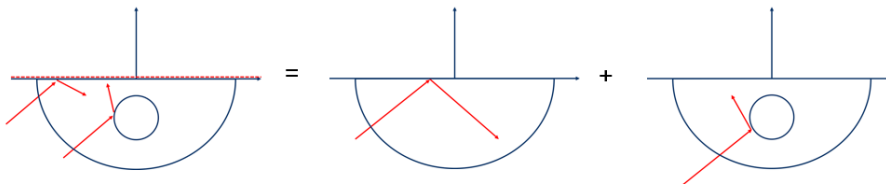


Figure 2.1: Wave field composition

Due to the presence of the cavity, a scattered wave field is produced. In the absence

of the cavity, the free wave field is composed of incident waves which come from infinitely far below, and reflected waves which are generated at the half-space surface in order to satisfy the traction-free boundary conditions. The total wave field to be solved consists of the free wave field and the scattered wave field. The total displacement is

$$\mathbf{u}^{\text{tot}} = \mathbf{u}^{\text{free}} + \mathbf{u}^{\text{sc}} = (\mathbf{u}^{\text{inc}} + \mathbf{u}^{\text{ref}}) + \mathbf{u}^{\text{sc}} \quad (2.1)$$

where the bold letters denote vectors or matrices here and after;  $\mathbf{u}^{\text{tot}}$  is the total displacement field,  $\mathbf{u}^{\text{free}}$  is the free displacement field and  $\mathbf{u}^{\text{sc}}$  is the scattered displacement field.  $\mathbf{u}^{\text{inc}}$  and  $\mathbf{u}^{\text{ref}}$  represent the incident displacement field and the reflected displacement field, respectively.

However, we can make use of the traction-free boundary condition at the cavity surface. At the position of the cavity surface, all the stresses should be logically equal to zero if we consider the total field. This means, if we look at the free field and the scattered field separately, the summation of the stresses from these two fields should together make up zero value at the cavity surface

$$\mathbf{T}^{\text{tot}} = \mathbf{T}^{\text{free}} + \mathbf{T}^{\text{sc}} = \mathbf{0}, r_1 = R_1 \quad (2.2)$$

where  $r_1$  represents the local coordinate originating at the center of the cavity,  $R_1$  is the radius of the cavity,  $\mathbf{T}^{\text{free}}$  and  $\mathbf{T}^{\text{sc}}$  (traction vectors) are associated with the free field and scattered field, respectively. The convention holds here and hereafter. This boundary condition is the key to solving the problem. Because the traction from the free field at the cavity surface as an input is already known, the traction from the scattered field  $\mathbf{T}^{\text{sc}}$  at the cavity surface can be written by simply adding a minus sign, i.e.,

$$r_1 = R_1, \mathbf{T}^{\text{sc}} = -\mathbf{T}^{\text{free}} \quad (2.3)$$

In order to represent the scattered field, a group of sources are used, with known positions but unknown amplitudes. These sources will function the same as the cavity, producing the same scattered wave field. Note that these sources are to be placed slightly inside the cavity, which is illustrated in the fig.2.2.

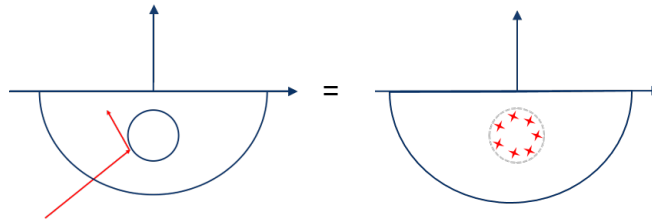


Figure 2.2: The scattered field produced by a number of sources (in red)

Once the unknown amplitudes of these sources have been solved, the response of the system can be computed by multiplying the sources with the transfer functions of the system.

### 2.1.2 Indirect boundary integrals

Now the old problem in figure 2.1 has been transformed such that the scattered field is represented as resulting from the action of a number( $N_s$ ) of sources. The unknown amplitudes of these sources can be solved by means of the fundamental solution of the complete half-space, the Green's functions. The scattered displacement field in the frequency domain at one observation is written in the form

$$\mathbf{U}^{\text{sc}}(\mathbf{x}) = \int_{L_0} \mathbf{G}(\mathbf{x}, \mathbf{x}_s) \mathbf{F}(\mathbf{x}_s) dl(\mathbf{x}_s) \quad (2.4)$$

where the capitalization of letters denotes the frequency domain; displacement vector  $\mathbf{U}^{\text{sc}}(\mathbf{x}) = [U_x, U_y, U_z]^T$ ; the contour  $L_0$  denotes the locations of the sources, and the integral means the joint contribution of all sources;  $\mathbf{x} = (x, y, z)$  is the location of an observation, and  $\mathbf{x}_s = (x_s, y_s, z_s)$  is the location of a source;  $\mathbf{G}(\mathbf{x}, \mathbf{x}_s)$  is the  $3 \times 3$  matrix of 2.5 D Green's functions for displacements. The 2.5D Green's functions are the steady state response of a half-space subjected to a spatially sinusoidal line load at one observation point located at  $\mathbf{x}$  due to a source located at  $\mathbf{x}_s$ . The first, second and third column of the matrix  $\mathbf{G}(\mathbf{x}, \mathbf{x}_s)$  correspond to the displacement vector due to a load acting in the  $x$ -,  $y$ - and  $z$ - direction, respectively. The matrix  $\mathbf{G}(\mathbf{x}, \mathbf{x}_s)$  has the form

$$\mathbf{G}(\mathbf{x}, \mathbf{x}_s) = \begin{bmatrix} G_{xx}^{(i,j)} & G_{xy}^{(i,j)} & G_{xz}^{(i,j)} \\ G_{yx}^{(i,j)} & G_{yy}^{(i,j)} & G_{yz}^{(i,j)} \\ G_{zx}^{(i,j)} & G_{zy}^{(i,j)} & G_{zz}^{(i,j)} \end{bmatrix} \quad (2.5)$$

where the superscript denotes the  $i$ -th observation and  $j$ -th source; the first index in subscript denotes the direction of displacement while the second index denotes the direction of the load. For example,  $G_{xy}$  represents the displacement component in  $x$ - direction due to a load acting in the  $y$ - direction. As is mentioned, this is a spatial sinusoidal and time-harmonic line load distributed along the longitudinal direction. Therefore, displacement in each of the direction is a consequence of the loads in all three directions.  $\mathbf{F}(\mathbf{x}_s) = [F_x, F_y, F_z]$  is the unknown amplitude vector of the sources which act in  $x$ -,  $y$ - and  $z$ - direction. These sources are located slightly inside the cavity. In a similar manner, stresses related to the scattered field have the following form:

$$\boldsymbol{\sigma}^{\text{sc}}(\mathbf{x}) = \int_{L_0} \mathbf{H}(\mathbf{x}, \mathbf{x}_s) \mathbf{F}(\mathbf{x}_s) dl(\mathbf{x}_s) \quad (2.6)$$

where in the left hand side  $\boldsymbol{\sigma}^{\text{sc}}(\mathbf{x}) = [\sigma_{rr}^x, \sigma_{r\theta}^x, \sigma_{rz}^x, \sigma_{\theta\theta}^x, \sigma_{zz}^x, \sigma_{\theta z}^x]^T$  is the stress vector at one observation point, and in the right hand side  $\mathbf{F}(\mathbf{x}_s)$  is the unknown amplitude vector of the sources same as before. The matrix  $\mathbf{H}(\mathbf{x}, \mathbf{x}_s)$  is the  $6 \times 3$  matrix of 2.5 D Green's functions for stresses.

$$\mathbf{H}(\mathbf{x}, \mathbf{x}_s) = \begin{bmatrix} \sigma_{rr}^x & \sigma_{rr}^y & \sigma_{rr}^z \\ \sigma_{r\theta}^x & \sigma_{r\theta}^y & \sigma_{r\theta}^z \\ \sigma_{rz}^x & \sigma_{rz}^y & \sigma_{rz}^z \\ \sigma_{\theta\theta}^x & \sigma_{\theta\theta}^y & \sigma_{\theta\theta}^z \\ \sigma_{zz}^x & \sigma_{zz}^y & \sigma_{zz}^z \\ \sigma_{\theta z}^x & \sigma_{\theta z}^y & \sigma_{\theta z}^z \end{bmatrix} \quad (2.7)$$

Once the unknown amplitudes of the sources  $\mathbf{F}(\mathbf{x}_s)$  are known, displacements and stresses related to the scattered field at any point in the system can be computed by equation (2.4) and equation (2.6). In the next section, the manner to find the unknown amplitudes of these sources are discussed.

For convenience, at the tunnel invert, the stress vector  $\boldsymbol{\sigma}^{\text{sc}}(\mathbf{x})$  is defined using cylindrical coordinates, while the direction of the sources are defined in Cartesian coordinates. Therefore, a transformation matrix is required to transform the Green's function stress terms. The displacement and stress expressions in cylindrical coordinates can be derived by transforming the ones in Cartesian coordinates using the following relations

$$\begin{bmatrix} u_r \\ u_\theta \\ u_z \end{bmatrix} = \mathbf{R} \begin{bmatrix} u_x \\ u_y \\ u_z \end{bmatrix} \quad (2.8)$$

$$\begin{bmatrix} \sigma_{rr} & \sigma_{r\theta} & \sigma_{rz} \\ \sigma_{\theta r} & \sigma_{\theta\theta} & \sigma_{\theta z} \\ \sigma_{zr} & \sigma_{z\theta} & \sigma_{zz} \end{bmatrix} = \mathbf{R} \begin{bmatrix} \sigma_{xx} & \sigma_{xy} & \sigma_{xz} \\ \sigma_{yx} & \sigma_{yy} & \sigma_{yz} \\ \sigma_{zx} & \sigma_{zy} & \sigma_{zz} \end{bmatrix} \mathbf{R}^T \quad (2.9)$$

where

$$\mathbf{R} = \begin{bmatrix} \cos\theta & \sin\theta & 0 \\ -\sin\theta & \cos\theta & 0 \\ 0 & 0 & 1 \end{bmatrix} \quad (2.10)$$

where the cylindrical coordinates are defined as  $x = r \cdot \sin\theta$  and  $y = r \cdot \cos\theta$ ,  $\mathbf{R}^T$  is the transpose of the transformation matrix  $\mathbf{R}$ . In this way, the Green's functions for stresses are transformed from Cartesian coordinates to cylindrical coordinates. The same process should be carried out for loads acting in  $x$ -,  $y$ -, and  $z$  direction respectively.

## 2.2 Fundamental solution - 2.5D Green's functions

### 2.2.1 Green's functions for a full-space

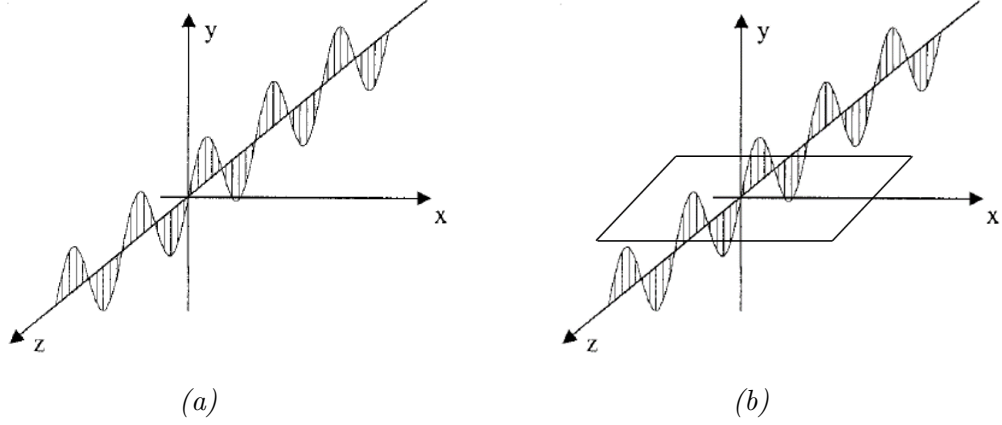


Figure 2.3: Sinusoidal harmonic line load acting at the origin of: (a) a full-space; (b) a half-space

As is known, the response of a system due to a load in the frequency domain is equal to the multiplication of the transfer function of the system and the Fourier transform of the load. For a special case where the load is an impulse excitation, the frequency response of the system is called the Green's function. The Green's functions applied in this thesis work are based on the paper of A.Tadeu et al [13][15]. The 2.5D Green's functions are steady state responses of a homogeneous 3D space subjected to a spatially sinusoidal harmonic line load. However, these Green's functions are consistent with the response functions for constant moving loads. This requires considering constant point sources moving with constant speed  $V = \omega/k_z$ .

Consider an infinitely large homogeneous 3D full space which is subjected to a time-harmonic and spatially varying line load of the form  $p(x, y, z, t) = \delta(x)\delta(y)e^{i(\omega t - k_z z)}$  at the origin of coordinates acting in any direction (figure 2.3a). In this expression,  $\delta(x)$ ,  $\delta(y)$  and  $\delta(z)$  are Dirac-delta functions,  $\omega$  is the frequency of the load and  $k_z$  is the wave number in the  $z$  direction. The response to this load can be obtained by applying a spatial Fourier transform in the  $z$ -direction to the Helmholtz wave potential equations for a time-harmonic point load:

$$\nabla^2 A_p + k_p^2 A_p = \frac{1}{4\pi R} \frac{1}{\rho c_p^2} \quad (2.11a)$$

$$\nabla^2 A_s + k_s^2 A_s = \frac{1}{4\pi R} \frac{1}{\rho c_s^2} \quad (2.11b)$$

in which  $A_p(x, y, z, \omega)$  and  $A_s(x, y, z, \omega)$  are irrotational and equivoluminal parts of the displacement vector, respectively; compressional wave speed  $c_p = \sqrt{(\lambda + 2\mu)/\rho}$  and shear wave speed  $c_s = \sqrt{\mu/\rho}$ ;  $k_p = \omega/c_p$ ,  $k_s = \omega/c_s$  are corresponding wave numbers;  $\lambda$  and  $\mu$  are Lamé's constants;  $\rho$  is the density;  $R = \sqrt{x^2 + y^2 + z^2}$  is radial distance between the source and the receiver; Laplace operator  $\nabla^2 = \frac{\partial^2}{\partial x^2} + \frac{\partial^2}{\partial y^2} + \frac{\partial^2}{\partial z^2}$ . The transformed

equations are

$$\frac{\partial^2 \hat{A}_p}{\partial x^2} + \frac{\partial^2 \hat{A}_p}{\partial y^2} + k_\alpha^2 \hat{A}_p = \frac{-iH_0^{(2)}(-ik_z r)}{4\rho c_p^2} \quad (2.12a)$$

$$\frac{\partial^2 \hat{A}_s}{\partial x^2} + \frac{\partial^2 \hat{A}_s}{\partial y^2} + k_\beta^2 \hat{A}_s = \frac{-iH_0^{(2)}(-ik_z r)}{4\rho c_s^2} \quad (2.12b)$$

in which  $\hat{A}_p(x, y, k_z, z, \omega)$  and  $\hat{A}_s(x, y, k_z, z, \omega)$  are Fourier transforms of the two potentials;  $H_0^{(2)}()$  are Hankel functions of the second kind and order zero;  $r = \sqrt{x^2 + y^2}$  is radial distance on the 2D plane and  $i = \sqrt{-1}$ ;  $k_\alpha = \sqrt{k_p^2 - k_z^2}$  and  $k_\beta = \sqrt{k_s^2 - k_z^2}$  with imaginary part  $\text{Im}(k_\alpha) < 0$  and  $\text{Im}(k_\beta) < 0$  to prevent infinite displacement at  $r = \infty$ .

The complete solution to these second-order partial differential equations is found by assuming a homogeneous solution and a particular solution, with unknown constants solved by satisfying radiation condition at infinity and equilibrium conditions at the origin. In the end, the wave potentials in the frequency domain are

$$\hat{A}_p = \frac{1}{4\rho\omega^2} \left[ H_0^{(2)}(k_\alpha r) - H_0^{(2)}(-ik_z r) \right] \quad (2.13a)$$

$$\hat{A}_s = \frac{1}{4\rho\omega^2} \left[ H_0^{(2)}(k_\beta r) - H_0^{(2)}(-ik_z r) \right] \quad (2.13b)$$

The displacement  $G_{ij}$  in direction  $i$  due to a load applied in direction  $j$  can be obtained from the relation

$$G_{ij} = \frac{\partial^2 (\hat{A}_p - \hat{A}_s)}{\partial x_i \partial x_j} + \delta_{ij} \hat{\nabla}^2 \hat{A}_s \quad (2.14)$$

where  $i, j = x, y, z$  and  $\delta_{ij}$  Kronecker delta;  $\frac{\partial}{\partial z} = -ik_z$  and  $\hat{\nabla}^2 = \frac{\partial^2}{\partial x^2} + \frac{\partial^2}{\partial y^2} - k_z^2$ .

Therefore, the complete set of Green's functions for a three dimensional full-space is

$$G_{xx}^{\text{full}} = A \left[ k_s^2 H_{0\beta} - \frac{1}{r} B_1 + \left( \frac{x - x_0}{r} \right)^2 B_2 \right] \quad (2.15a)$$

$$G_{yy}^{\text{full}} = A \left[ k_s^2 H_{0\beta} - \frac{1}{r} B_1 + \left( \frac{y - y_0}{r} \right)^2 B_2 \right] \quad (2.15b)$$

$$G_{zz}^{\text{full}} = A [k_s^2 H_{0\beta} - k_z^2 B_0] \quad (2.15c)$$

$$G_{xy}^{\text{full}} = G_{yx}^{\text{full}} = \left( \frac{x - x_0}{r} \right) \left( \frac{y - y_0}{r} \right) AB_2 \quad (2.15d)$$

$$G_{xz}^{\text{full}} = G_{zx}^{\text{full}} = ik_z \left( \frac{x - x_0}{r} \right) AB_1 \quad (2.15e)$$

$$G_{yz}^{\text{full}} = G_{zy}^{\text{full}} = ik_z \left( \frac{y - y_0}{r} \right) AB_1 \quad (2.15f)$$

where the amplitude  $A = \frac{1}{4i\rho\omega^2}$  and  $r = \sqrt{(x - x_0)^2 + (y - y_0)^2}$  is the radial distance between a source located at  $(x_0, y_0)$  and a receiver at  $(x, y)$ ; modified Hankel functions

are expressed through the Hankel's functions of the second kind  $B_n = k_\beta^n H_n^{(2)}(k_\beta r) - k_\alpha^n H_n^{(2)}(k_\alpha r)$  where the integer number  $n$  denotes the order. The corresponding strain and stress Green's functions can be found on [13]. They are derived from equation (2.15) by means of the well-known equations relating displacements and strains. The strains components can be derived from the displacement field with

$$\varepsilon_{ij} = \frac{1}{2} \frac{\partial u_i}{\partial j} + \frac{1}{2} \frac{\partial u_j}{\partial i} \quad (2.16)$$

where  $i, j = x, y, z$ . Stresses in terms of strains are

$$\sigma_{ij} = \lambda \varepsilon_{kk} \delta_{ij} + 2\mu \varepsilon_{ij} \quad (2.17)$$

with the Lamé's constants

$$\lambda = \frac{E\nu}{(1+\nu)(1-2\nu)}, \mu = \frac{E}{2(1+\nu)} \quad (2.18)$$

related to the Young's modulus  $E$  and the Poisson's ratio  $\nu$ . These Green's functions are defined in the frequency-wavenumber domain with the frequency  $\omega$  and the wave number  $k_z$  specified. For the moving load problem,  $k_z = \omega/V$  where  $V$  is the moving load velocity. There are a few things that can be observed: firstly, the frequency  $\omega$  in the denominators indicate the singularity of these displacements at  $\omega = 0$ , and that is to say, static response cannot be calculated; secondly, the in-plane distance  $r$  appeared in the arguments of Hankel functions implies the singularity at  $r = 0$  because the value is infinite at this point, which explains the reason why the sources and receivers (or observations) can not be located at the same position; thirdly, it is seen that the displacements in the  $x, y$  direction are very similar because the full-space is symmetric in these two directions; and lastly, the  $z$ -dependence of these displacements is just  $ik_z$ , since waves are assumed to be spatially sinusoidal in  $z$  direction for the steady-state solution. In other words, the  $z$ -coordinates of sources and receivers are needed in computing the Green's functions. In order to apply these Green's functions, one just need to know the dynamic properties, material properties of the full space and positions of the sources and receivers in the 2D plane.

### 2.2.2 Green's functions for a half-space

A remarkable difference between a full-space and a half-space is the satisfaction of the stress-free boundary conditions at the half-space surface. This is accomplished by considering the free wave field as a superposition of incident waves and reflected waves, and writing the reflected waves in terms of the incident waves multiplying with unknown coefficients. In the end, these unknown coefficients are solved by satisfying the stress-free boundary condition at the half-space surface. In this way, the Green's functions for a half-space (which contains these coefficients) automatically satisfy the boundary condition.

Therefore, the Green's functions for a half-space are written as a sum of the Green's functions for a full-space (incident waves) and surface terms (reflected waves). These waves are written as a superposition of a series of waves which have different wavenumbers

in space. This is the so-called discrete wave number method (DWNM). It was previously introduced by Bouchon [14]. It relies on the exact discretization of the elastic wave fields by considering infinitely many wave numbers. This is similar to the law of diffraction of light by grating.

Load acting  $x$ ,  $y$ , and  $z$  direction should be considered separately. Here, for the purpose of illustration, the Green's function displacement terms for loading act in the  $x$  direction is discussed, while the Green's functions for load acting in  $y$ - and  $z$ - direction are given in the appendix.

Based on the discrete wave number representation, the displacements resulting from a spatially sinusoidal harmonic line load along the  $z$  direction, applied at the point  $(x_0, y_0)$  in the  $x$  direction for a half-space are given by

$$G_{xx}^{\text{half}} = E_a \int_{-\infty}^{+\infty} \left( \frac{-ik_x^2}{k_{py}} E_b + \left( -ik_{sy} - \frac{ik_z^2}{k_{sy}} \right) E_c \right) e^{-ik_x(x-x_0)} dk_x \quad (2.19a)$$

$$+ E_a \int_{-\infty}^{+\infty} \left( A^x \frac{-ik_x^2}{k_{py}} E_{b0} + \left( -ik_{sy} C^x - \frac{ik_z^2}{k_{sy}} B^x \right) E_{c0} \right) e^{-ik_x(x-x_0)} dk_x \quad (2.19b)$$

$$G_{yx}^{\text{half}} = E_a \int_{-\infty}^{+\infty} (-i \cdot \text{sgn}(y - y_0) k_x E_b + i \cdot \text{sgn}(y - y_0) k_x E_c) e^{-ik_x(x-x_0)} dk_x \quad (2.19c)$$

$$+ E_a \int_{-\infty}^{+\infty} (-ik_x A^x E_{b0} + ik_x C^x E_{c0}) e^{-ik_x(x-x_0)} dk_x \quad (2.19d)$$

$$G_{zx}^{\text{half}} = E_a \int_{-\infty}^{+\infty} \left( \frac{-ik_z k_n}{k_{py}} E_b + \frac{ik_z k_n}{k_{sy}} E_c \right) e^{-ik_x(x-x_0)} dk_x \quad (2.19e)$$

$$+ E_a \int_{-\infty}^{+\infty} \left( \frac{-ik_z k_n}{k_{py}} A^x E_{b0} + \frac{ik_z k_n}{k_{sy}} B^x E_{c0} \right) e^{-ik_x(x-x_0)} dk_x \quad (2.19f)$$

where

$$E_a = \frac{1}{4\pi\rho\omega^2} \quad (2.20a)$$

$$E_b = e^{-ik_{py}|y-y_0|} \quad (2.20b)$$

$$E_c = e^{-ik_{sy}|y-y_0|} \quad (2.20c)$$

$$E_{b0} = e^{-ik_{py}y} \quad (2.20d)$$

$$E_{c0} = e^{-ik_{sy}y} \quad (2.20e)$$

$$E_{b1} = e^{-ik_{py}y_0} \quad (2.20f)$$

$$E_{c1} = e^{-ik_{sy}y_0} \quad (2.20g)$$

and  $\text{sgn}$  represents the signum function;  $k_x$  is the wave number in the horizontal direction,  $k_{py} = \sqrt{k_p^2 - k_z^2 - k_x^2}$  is the vertical component of P wavenumber with  $(\text{Imag}(k_{py}) \leq 0)$ , and  $k_{sy} = \sqrt{k_s^2 - k_z^2 - k_x^2}$  is the vertical component of S wavenumber with  $(\text{Imag}(k_{sy}) \leq 0)$ . This is because

$$e^{-ik_{py}y} = e^{-i(\text{Re}\{k_{py}\} + i\text{Im}\{k_{py}\})y} = e^{-i\text{Re}\{k_{py}\}y} \cdot e^{\text{Im}\{k_{py}\}y} \quad (2.21)$$

with the first term representing the oscillation nature of waves, and the second term representing the decay of waves with distance  $y$  increases and radiation at  $y = +\infty$ . The



same holds for  $k_{sy}$ . Therefore, the imaginary parts must be negative. For each of the displacement in equation (2.19), the first term is the Green's function for a full-space and is equivalent to that in (2.15) mentioned previously. While the second term are the surface terms which are needed for the satisfaction of stress-free boundary conditions at the surface  $y = 0$ . Together, they make up the complete Green's functions for a half-space. The second term is very similar to the first term but with unknown coefficients  $A^x$ ,  $B^x$  and  $C^x$  to be determined from the stress-free boundary conditions at the half-space surface, i.e.,

$$y = 0, \sigma_{yx} = \sigma_{yy} = \sigma_{yz} = 0 \quad (2.22)$$

The stress-free boundary conditions should be satisfied per wave number  $k_x$ . This procedure includes the partial derivatives of the integrands in equation (2.19) to go from displacement to stresses, again by using the well-known constitutive relation. Finally, the imposition of the three boundary conditions leads to a system of three equations with three unknowns for each  $k_x$ .

$$\begin{bmatrix} -2k_x^2 & -k_z^2 & k_x^2 - k_{sy}^2 \\ -2 & 1 & 1 \\ \frac{-k_s^2}{k_{py}} + \frac{2k_{hor}^2}{k_{py}} & 0 & 2k_{sy} \end{bmatrix} \times \begin{bmatrix} A^x \\ B^x \\ C^x \end{bmatrix} = \begin{bmatrix} -2k_x^2 E_{b1} + (-k_s^2 + 2k_x^2) E_{c1} \\ -2E_{b1} + 2E_{c1} \\ (\frac{k_s^2}{k_{py}} - \frac{2k_{hor}^2}{k_{py}}) E_{b1} - 2k_{sy} E_{c1} \end{bmatrix} \quad (2.23)$$

In order to solve these linear algebraic equations, one can apply the Cramer's rule. Taking the determinant of the coefficient matrix on the left hand side, one can observe the Rayleigh denominator having the form

$$\Delta_R = -\frac{1}{k_{py}} \{ (k_s^2 - 2(k_x^2 + k_z^2))^2 + 4(k_x^2 + k_z^2)k_{py}k_{sy} \} \quad (2.24)$$

which renders the solution to become infinity when  $\Delta_R = 0$ . The Rayleigh pole in the denominator appears when the horizontal wave number is equal to one of the roots of the equation  $\Delta_R = 0$ , i.e.,

$$k_{x,R}^2 = k_R^2 - k_z^2 \quad (2.25)$$

where  $k_R$  is the Rayleigh wave number. Furthermore, this indicates the maxima at  $k_x = k_{x,R}$  which occurs in the wavenumber spectra of the half-space Green's functions. To further illustrate this phenomenon, one example is given in the next section.

Having obtained these unknown constants, the Green's functions related to the half-space can be computed. This is done in a different manner than described on A.Tadeu's paper and is discussed in the next section.

Here, only the Green's functions due to loads acting in  $x$  direction are shown. Similarly, for loads acting in  $y$  and  $z$  directions, the same procedure should be consistently carried out. The full set of the half-space Green's functions for displacements is shown in the Appendix.

## 2.2.3 Preliminary checks

### 2.2.3.1 Convergence

As stated before, the Green's functions for a half-space is a sum of the Green's functions for a full-space which is expressed in analytical form (equation (2.15)), and the surface terms to satisfy the boundary conditions on the half-space surface which are expressed using discrete wave number representation. The convergence in evaluating the integrals is of concern. For example, recalling a displacement surface-related term

$$G_{yy}^{\text{surf}} = E_a \int_{-\infty}^{+\infty} \left[ -ik_{py} A^y E_{b0} + \left( \frac{-ik_x^2}{k_{sy}} B^y + \frac{-ik_z^2}{k_{sy}} C^y \right) E_{c0} \right] e^{-ik_x(x-x_0)} dk_x \quad (2.26)$$

where the discretization of horizontal wave number  $k_x$  plays an important role in the convergence. Firstly, since calculating infinitely many wave numbers is not possible,  $k_x$  should be truncated at a relatively large value, ensuring that all the energy is taken into account. Secondly, the increment of the wavenumber  $dk_x$  should be small enough so that there will be no leakage in the wavenumber spectra causing the inaccuracy of the calculation.

The locations of the source and receiver considered here are (5,5) and (3,0). The material properties for the half-space are: elastic modulus  $E = 2.13 \times 10^8 \text{N/m}^2$ , Poisson's ratio  $\nu = 0.33$ , medium density  $\rho = 2000 \text{kg/m}^3$ , which result in the wavespeed  $c_p = 397 \text{m/s}$ ,  $c_s = 200 \text{m/s}$ , and Rayleigh wave speed  $c_R = 186 \text{m/s}$ . The excitation frequency is  $\omega = 10 \cdot 2\pi \text{ rad/s}$ ; horizontal components of P-wave number and S-wave number are  $k_\alpha = \sqrt{k_p^2 - k_z^2}$  and  $k_\beta = \sqrt{k_s^2 - k_z^2}$  where the longitudinal wavenumber is define by  $k_z = \omega/V$ . As can be seen, the value of  $k_z$  decreases as the velocity  $V$  increases. The cross points will be  $V = c_s$  and  $V = c_p$ , after which  $k_\alpha$  and  $k_\beta$  change from real numbers to complex numbers. Physically, this means evanescent waves evolve into propagating waves.

In table 2.1, values of wavenumbers are listed for  $V$  equal to 180 m/s, 190 m/s, 210 m/s and 200 m/s.

Figure	$V$ [m/s]	$\text{Re}\{k_\alpha\}$	$\text{Re}\{k_\beta\}$	$\text{Re}\{k_{x,R}\}$
2.4(a)	180	0.000040	0.00032	0.00062
2.4(b)	190	0.000043	0.00047	0.06443
2.4(c)	210	0.000049	0.09530	0.15488
2.4(d)	400	0.018579	0.27190	0.29805

Table 2.1: wavenumber values for different velocities

Figure 2.4 shows half of the wavenumber spectra for the integrand of  $|G_{yy}^{\text{surf}}|$ . The integral range is discretized with sufficiently small intervals and is truncated at a sufficiently large value  $k_x = 2\pi$ . In figure 2.4, differently scenarios are observed for different velocities. For  $V < c_R$ , the evanescent waves have the main part of energy concentrated around  $k_x = 0$  since it is a constant load. For  $c_R < V < c_s$  comparing figure 2.4(b) and 2.4(a), the first peak is observed when  $k_x = k_{x,R}$ . This peak occurs because of the Rayleigh pole in the denominator, as discussed before. The amplitude of the peak is 100

times the one in the case  $V < c_R$ . The distribution is more narrow-banded and the non-zero part is between  $k_x = 0$  and  $k_x = k_{x,R}$  is due to a small amount of damping. For  $V > c_s$ , as shown in figure 2.4(c) and 2.4(d), a second peak is observed at  $k_x = k_\beta$ , the horizontal component of shear wave wavenumber. The amplitudes of these maximas decrease when the velocity  $V$  increases further. Also, there are no more peaks observed for  $V > c_p$ .

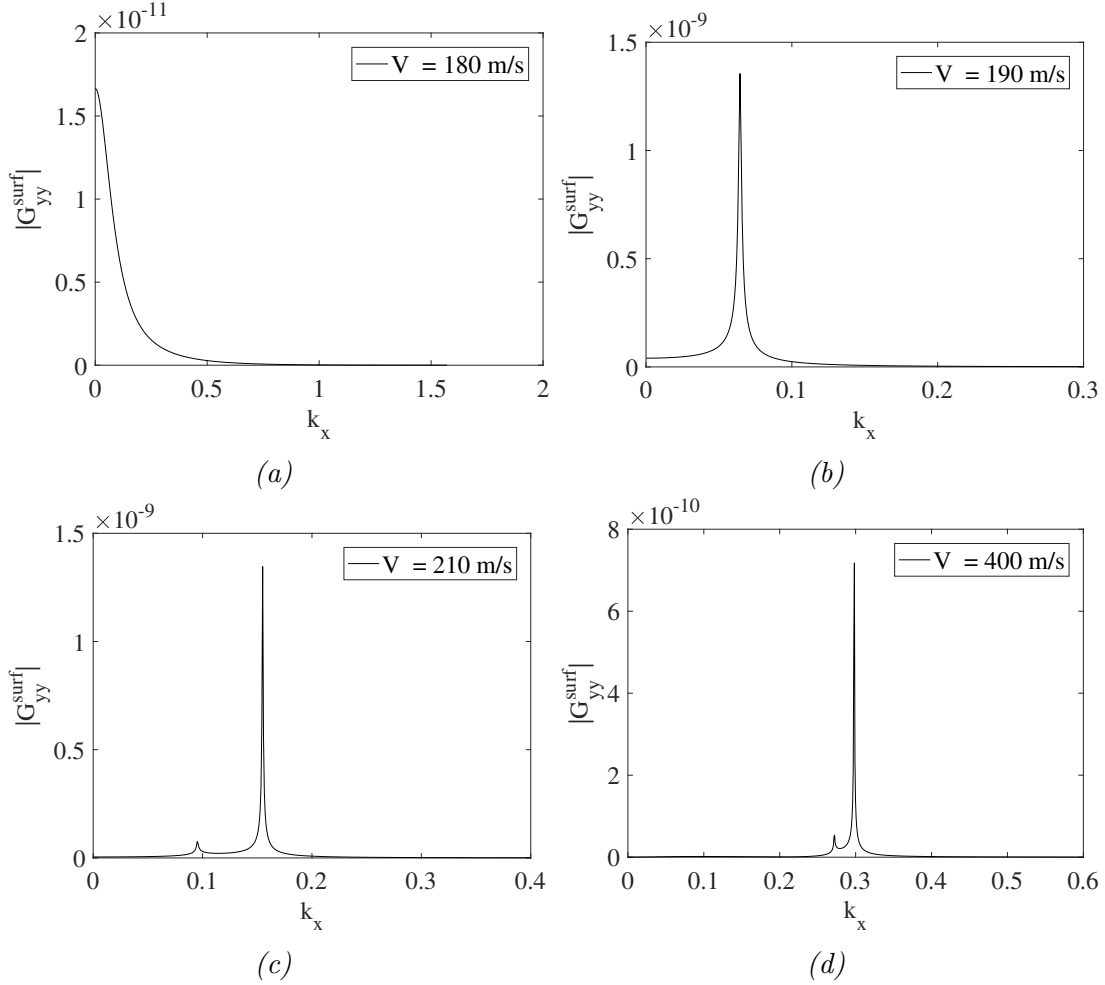


Figure 2.4: Wavenumber spectra for the displacement surface term  $G_{yy}^{surf}$

The distribution of the spectra provide a hint to the evaluation of the integral in these surface terms. These integrals are in fact the inverse Fourier transform with wavenumber  $k_x$ . On the paper by A.Tadeu, these integrals are evaluated by calculating the integrand for each  $k_x$  and summing up all the components. This is similar to applying the trapezoidal integration rule. To do this, one needs to compute the unknown coefficients as shown in equation (2.23) for each wavenumber. There are two disadvantages by doing this: firstly it is computational demanding in solving the  $3 \times 3$  matrices many times; secondly and more importantly, it is difficult to determine the truncated wavenumber  $k_x$  and the increment  $\Delta k_x$  since the integration is case-dependent. For different materials and excitation frequencies, the values of integrals are sensitive to the choice of the discretization of  $k_x$ .

Evaluating these integrands is done in a different way, which is by applying a numerical integration routine. This involves solving the unknown coefficients analytically and

having the analytical form for these integrands. This simplifies the procedure of solving them per wavenumber. Then the integrands are integrated over wavenumber using numerical integration. Specifically, the adaptive Gauss-Kronrod quadrature is chosen for the numerical integration, where the integrands are approximated using high-order polynomials. Furthermore, due to the existence of maximas in the previous spectra, singular points (such as  $k_x = k_{x,R}$ ) are handled by making them endpoints of each separate integration. Therefore, the whole integrand is integrated over several small intervals and added up.

There are two main advantages by substituting trapezoidal integration rule with Gaussian quadrature. Firstly, the accuracy in evaluating the integrands is improved. The choice of the discretization of  $k_x$  are automatically taken into account using a matlab function `quadk`. For double-precision for floating-point values in the following calculations, absolute error tolerance is set to be  $1e-10$ . On the other hand, the computational time is reduced due to the fact that the unknown coefficients in the surface-related terms are solved just for once.

### 2.2.3.2 Satisfaction of boundary conditions

In the previous section, the convergence of the surface-related terms are improved using the numerical integration routine. The convergence of these terms is important because it also directly influences how well the boundary conditions on the half-space surface  $y = 0$  are satisfied. The satisfaction of these boundary conditions should be ensured in any case. In the following, the satisfaction of these free-stress boundary conditions are checked.

The locaiton of the source and receiver considered here is (5,5) and (3,0); the material properties used here for the half-space are: elastic modulus  $E = 2.13 \times 10^8 \text{N/m}^2$ , poisson's ratio  $\nu = 0.33$ , medium density  $\rho = 2000 \text{kg/m}^3$ ; the excitation frequency is  $\omega = 10 \cdot 2\pi$  rad/s.

	$l = x$	$l = y$	$l = z$
$ \Sigma_{yx} $	2.159e-18 <b>2.337e-15</b>	1.095e-4 <b>3.581e-14</b>	1.597e-18 <b>4.436e-16</b>
$ \Sigma_{yy} $	3.175e-5 <b>2.117e-14</b>	1.452e-16 <b>1.336e-15</b>	2.810e-4 <b>2.752e-16</b>
$ \Sigma_{yz} $	8.172e-20 <b>4.448e-16</b>	3.433e-4 <b>8.284e-17</b>	3.541e-17 <b>4.083e-15</b>

Table 2.2: stresses at the half-space surface: normal font size denotes the original method; bold font size denotes the improved method

Table 2.2 clearly shows the difference between the Green's function stresses by the originally proposed method from A.Tadue and that by newly proposed numerical integration routine in the previous section. The stress components  $\Sigma_{yx}$ ,  $\Sigma_{yy}$  and  $\Sigma_{yz}$  at the half-space surface shown in the table must be equal to zero. However, using numerical tools such as MATLAB, these values should be within precision tolerance. It is shown

that the newly-proposed numerical integration routine has indeed improved the satisfaction of stress-free boundary conditions of the Green's functions. A good satisfaction of stress-free boundary conditions is a prerequisite for a good accuracy.

### 2.2.3.3 Symmetry

The symmetry property is an inherent characteristics of the Green's functions. It depends on the system only and has no relation with the boundary conditions or external forces. If the positions of the receivers relative to the sources are symmetric, then the responses should also be symmetric in these receivers.

For the considered half-space model, the whole medium is geometrically symmetry with the vertical axis  $y$ . Therefore, if a load acts in the  $y$  direction, the response in the half-space should be symmetric with  $y$  axis as well. Two examples of the Green's functions are shown in Fig2.5. Fig2.5(a) shows  $G_{yy}$  the displacement in  $y$  direction due to a load acting in the  $y$  direction at the lowest point and fig2.5(b) shows the radial stress  $\sigma_{rr}$  due to a load acting in the  $y$  direction at the lowest point. Logically, the response should be symmetric with  $y$  axis.

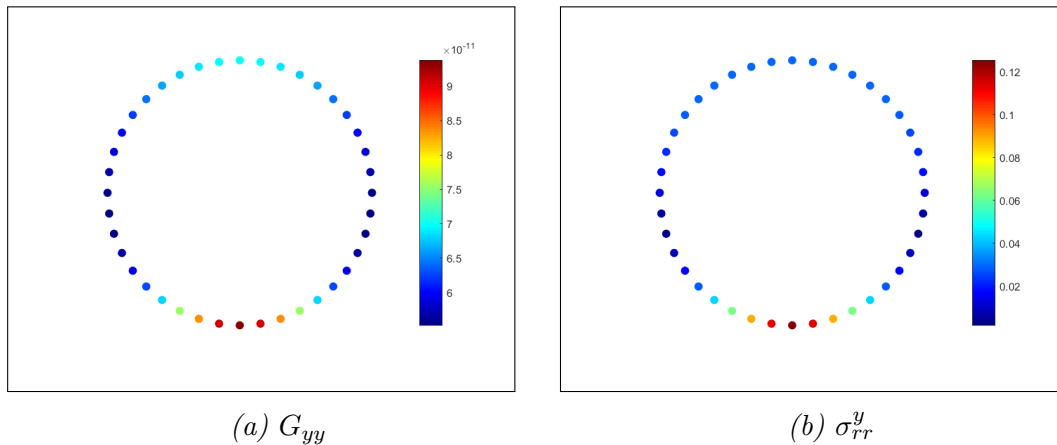


Figure 2.5: Symmetry property of Green's functions

In each figure, 40 points of receivers are arranged in a circle, with different colors denoting the values. As is shown, the values in these receiver are indeed symmetric. Other responses such as  $G_{xy}, G_{zy}, \dots$  follow the same principle. The symmetry property is a prerequisite that the Green's functions are correctly constructed. However, for load acting in the  $x$  direction, this symmetry property does not necessarily hold.

## 2.3 Donnell theory for thin cylindrical shells

### 2.3.1 Governing equations

The tunnel of a circular cross section buried in the half-space can be conceptualized as an infinitely long tube surrounded by soil. Since the wall thickness of the tunnel is thin compared to its radius ( $t/a < 1/10$ ), cylindrical thin shell theory is used to model the tunnel. In general, according to the first assumption in the Love-Kirchhoff hypothesis in the theory of small displacements of thin shells, the thickness of the shell is considered small in comparison to other dimensions. Because of the complexity in deriving the equations of motion of a shell, this assumption may be used in different manners, resulting in various shell theories. A comprehensive study was performed on various shell theories and it is explicitly explained in the work of Leissa [16].

The three-dimensional infinitely long circular cylindrical shell used here is assumed to be linear elastic, homogeneous and isotropic. Such a shell is shown in figure 2.6.

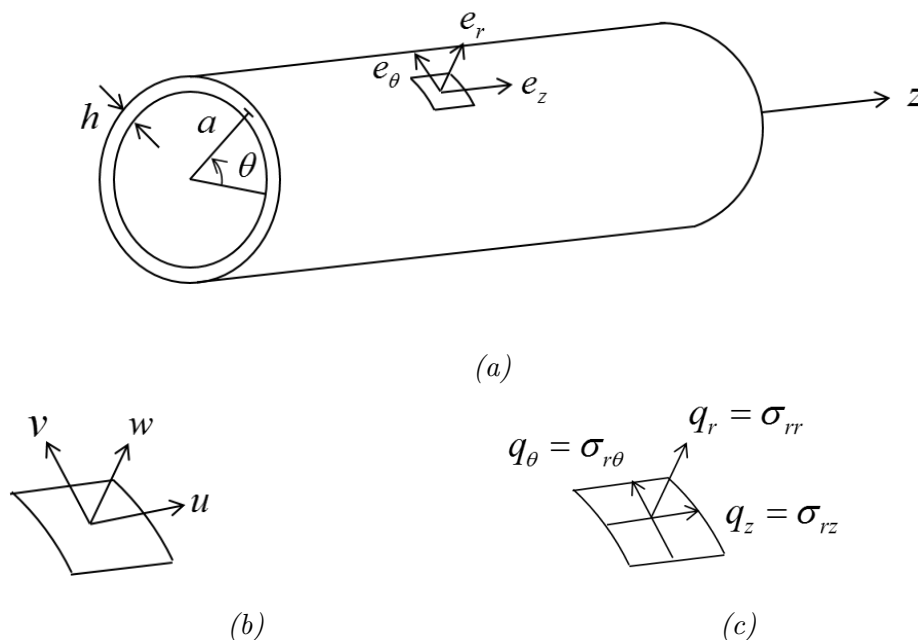


Figure 2.6: Coordinate system for three-dimensional cylindrical shell equations showing (a) the principle direction for a piece of shell element; (b) the corresponding displacement components and (c) the corresponding surface traction components

### Governing equations

The general dynamic equations are described by a system of three coupled partial differential equations in the form

$$\rho h \frac{\partial^2 \mathbf{u}_2(\mathbf{x}, t)}{\partial t^2} - K_0 \mathbf{L} \cdot \mathbf{u}_2(\mathbf{x}, t) = \mathbf{q}_{2e}(\mathbf{x}, t) \quad (2.27)$$

where  $\mathbf{u}_2(\mathbf{x}, t) = [u, v, w]^T$  represents the mid-surface displacement vector with local cylindrical coordinates: the longitudinal displacement  $u$ , the circumferential displacement  $v$

and the radial displacement  $w$  in the three principal directions;  $\mathbf{q}_{2e}(\mathbf{x}, t) = [q_r, q_\theta, q_z]^T$  is the corresponding effective or net traction acting on the shell, which are the differences between the inside and outside surface tractions, also referred to local cylindrical coordinates;  $\rho$  is the density of the shell,  $h$  is the thickness of the shell,  $K_0 = Eh/(1 - \nu^2)$  in which  $E$  is the elastic modulus and  $\nu$  the Poisson's ratio of the shell. The differential operator matrix  $\mathbf{L}$  is a  $3 \times 3$  matrix depending on the type of shell theory. Various shell theories share the fundamental formulation common, which is the Donnell-Mustari part to be used here. In order to use other shell theories, an extra modification matrix should be added. Here for the Donnell shell theory,  $\mathbf{L}$  contains the following elements,

$$L_{11} = \frac{\partial^2}{\partial z^2} + \frac{(1 - \nu)}{2a^2} \frac{\partial^2}{\partial \theta^2} \quad (2.28a)$$

$$L_{22} = \frac{(1 - \nu)}{2} \frac{\partial^2}{\partial z^2} + \frac{1}{a^2} \frac{\partial^2}{\partial \theta^2} \quad (2.28b)$$

$$L_{33} = -\frac{h^2}{12} \left( \frac{\partial^4}{\partial z^4} + \frac{2}{a^2} \frac{\partial^4}{\partial z^2 \partial \theta^2} + \frac{1}{a^4} \frac{\partial^4}{\partial \theta^4} \right) - \frac{1}{a^2} \quad (2.28c)$$

$$L_{12} = L_{21} = \frac{1 + \nu}{2a} \frac{\partial^2}{\partial z \partial \theta} \quad (2.28d)$$

$$L_{13} = -L_{31} = \frac{\nu}{a} \frac{\partial}{\partial z} \quad (2.28e)$$

$$L_{23} = -L_{32} = \frac{1}{a^2} \frac{\partial}{\partial \theta} \quad (2.28f)$$

This is obtained by adding inertia term to the static equations from Donnell [17], or Leissa [16]. Each equation corresponds to a dynamic equilibrium in one of the three principal directions. The hysteretic material damping can be introduced by using complex Lamé constants. In these governing equations, terms multiplied by  $h^2/12$  represent the contribution of bending effects of the shell, while the others represent the membrane effects.

The actual response of the shell to an arbitrary external loading can be seen as a superposition of harmonic movements due to harmonic loadings. This is realized in a similar manner by applying forward Fourier transform with respect to angle  $\theta$  in the paper by Luco et al[18]. Since we are looking for steady state solution, we can further assume the loading and the response be harmonic in both time and longitudinal direction, which are written as

$$q_z(\theta, z, t) = \sum_{n=-\infty}^{+\infty} \tilde{Q}_{zn} e^{in\theta} e^{i(\omega t + k_z z)} \quad (2.29a)$$

$$q_\theta(\theta, z, t) = \sum_{n=-\infty}^{+\infty} \tilde{Q}_{\theta n} e^{in\theta} e^{i(\omega t + k_z z)} \quad (2.29b)$$

$$q_r(\theta, z, t) = \sum_{n=-\infty}^{+\infty} \tilde{Q}_{rn} e^{in\theta} e^{i(\omega t + k_z z)} \quad (2.29c)$$

and the corresponding displacement components are

$$u(\theta, z, t) = \sum_{n=-\infty}^{+\infty} \tilde{U}_n e^{in\theta} e^{i(\omega t + k_z z)} \quad (2.30a)$$

$$v(\theta, z, t) = \sum_{n=-\infty}^{+\infty} \tilde{V}_n e^{in\theta} e^{i(\omega t + k_z z)} \quad (2.30b)$$

$$w(\theta, z, t) = \sum_{n=-\infty}^{+\infty} \tilde{W}_n e^{in\theta} e^{i(\omega t + k_z z)} \quad (2.30c)$$

where  $\omega$  is angular frequency,  $k_z$  is wavenumber in the longitudinal  $z$  direction,  $n$  is a positive integer denoting the mode number;  $\tilde{Q}_{zn}$ ,  $\tilde{Q}_{\theta n}$  and  $\tilde{Q}_{rn}$  represent the net applied load amplitudes for a particular circumferential mode  $n$  in directions  $z$ ,  $\theta$  and  $r$ , respectively;  $\tilde{U}_n$ ,  $\tilde{V}_n$  and  $\tilde{W}_n$  are the displacement component amplitudes for a particular circumferential mode  $n$  in directions  $z$ ,  $\theta$  and  $r$ , respectively; exponential terms with  $\theta$  show the angular distribution on the cylindrical cross section and represent the ring modes. Figure 2.7 shows the first three ring modes, which are in-plane flexural modes for radial displacement  $w$ , in-plane extensional modes for tangential displacement  $v$ , and out-of-plane flexural modes for longitudinal displacement  $u$ .

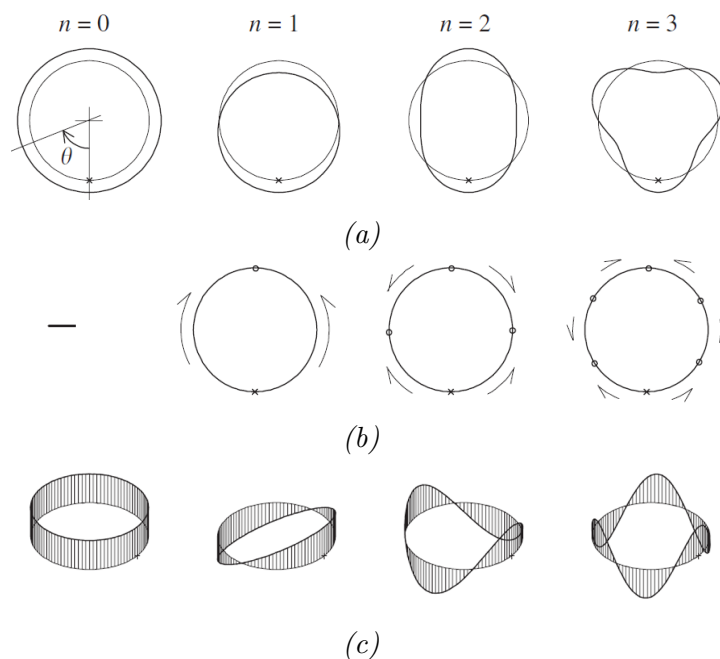


Figure 2.7: (a) In-plane flexural modes corresponding to radial displacement  $w$ ; (b) in-plane extensional modes corresponding to tangential displacement  $v$ ; and (c) out-of-plane flexural modes corresponding to longitudinal displacement  $u$ . [3]



### 2.3.2 Green's functions for thin cylindrical shells

Substituting the loading (2.29) and the displacements (2.30) into the equation of motion of the shell (2.28), the following relation between displacement at the midsurface and the net loading can be obtained:

$$\frac{Eh}{a^2} \mathbf{A}_n \tilde{\mathbf{U}}_{2n} = \tilde{\mathbf{Q}}_{2en} \quad (2.31)$$

where  $\tilde{\mathbf{U}}_{2n} = [\tilde{U}_n, \tilde{V}_n, \tilde{W}_n]^T$  and  $\tilde{\mathbf{Q}}_{2en} = [\tilde{Q}_{zn}, \tilde{Q}_{\theta n}, \tilde{Q}_{rn}]^T$  are the amplitudes of displacements and tractions, respectively.  $\mathbf{A}_n$  is a coefficient matrix in the form

$$\mathbf{A}_n = - \left( \frac{1}{1 - \nu^2} \right) \cdot \mathbf{L}_n - \left( \frac{\rho \omega^2 a^2}{E} \right) \cdot \mathbf{I} \quad (2.32)$$

where the matrix  $\mathbf{I}$  is a  $3 \times 3$  unit matrix. The elements of the matrix  $\mathbf{L}_n$  are given by

$$L_{11n} = - \left[ (k_z a)^2 + \left( \frac{1 - \nu}{2} \right) n^2 \right] \quad (2.33a)$$

$$L_{22n} = - \left[ \left( \frac{1 - \nu}{2} \right) (k_z a)^2 + n^2 \right] \quad (2.33b)$$

$$L_{33n} = - \frac{1}{12} \left( \frac{h}{a} \right) [(k_z a)^4 + 2(k_z a)^2 n^2 + n^4] - 1 \quad (2.33c)$$

$$L_{12n} = L_{21n} = \left( \frac{1 - \nu}{2} \right) (k_z a) n \quad (2.33d)$$

$$L_{13n} = -L_{31n} = -i\nu(k_z a) \quad (2.33e)$$

$$L_{23n} = -L_{32n} = in \quad (2.33f)$$

In fact, equation (2.31) is the relation between displacements at the shell midsurface and effective traction. In order to apply the continuity conditions at the interface, we should consider displacements and traction on the outside boundary  $r = a + h/2$  of the shell. Displacements at the midsurface and at the outside surface are related by

$$\tilde{\mathbf{U}}_{2n}^{\text{out}} = \mathbf{D}_n \tilde{\mathbf{U}}_{2n}^{\text{mid}} = \begin{bmatrix} 1 & 0 & i\frac{k_z h}{2} \\ 0 & 1 + \frac{h}{2a} & -\frac{nh}{2a} \\ 0 & 0 & 1 \end{bmatrix} \tilde{\mathbf{U}}_{2n}^{\text{mid}} \quad (2.34)$$

in the frequency domain. Provided there is only loading on the outer surface of the shell (zero loading at the inside), the effective traction vector is related to the traction vector on the outside surface  $r = a + h/2$  of the shell through the relation

$$\tilde{\mathbf{Q}}_{2en} = \mathbf{B}_n \tilde{\mathbf{Q}}_{2n} = \begin{bmatrix} 1 & 0 & 0 \\ 0 & 1 + \frac{h}{2a} & 0 \\ -i\frac{k_z h}{2} & i\frac{nh}{2a} & 1 \end{bmatrix} \tilde{\mathbf{Q}}_{2n} \quad (2.35)$$

Substituting equation (2.35) into (2.31) results in

$$\frac{Eh}{a^2} \mathbf{A}_n \tilde{\mathbf{U}}_{2n} = \mathbf{B}_n \tilde{\mathbf{Q}}_{2n} \quad (2.36)$$

Therefore, midsurface displacement amplitudes for each mode can be solved

$$\tilde{\mathbf{U}}_{2n} = \frac{a^2}{Eh} \mathbf{A}_n^{-1} \mathbf{B}_n \tilde{\mathbf{Q}}_{2n} \quad (2.37)$$

Since the total response is a superposition of infinitely many modes, considering contribution from all sources, it is written as

$$\mathbf{U}_2(\theta) = a \int_0^{2\pi} \mathbf{G}_2(\theta, \theta') \cdot \mathbf{Q}_2(\theta') d\theta' \quad (2.38)$$

in which the Green's function for the shell is

$$\mathbf{G}_2(\theta, \theta') = \frac{a}{2\pi Eh} \sum_{n=-\infty}^{+\infty} \mathbf{D}_n \mathbf{A}_n^{-1} \mathbf{B}_n e^{in(\theta-\theta')} \quad (2.39)$$

The  $3 \times 3$  dimensional Green's function  $\mathbf{G}_2(\theta, \theta')$  relates the outside displacement vector and the outside tractions of the shell. Since the shell has a symmetric circular cross-section, one just need to look at the difference between angle  $\theta$  and  $\theta'$ , which corresponds to the position of the receiver and source, respectively. The summation represents the superposition of modes. In practice, it is impossible to consider infinitely many circumferential modes for the summation, therefore, the number of modes should be large enough to reach a satisfactory convergence.

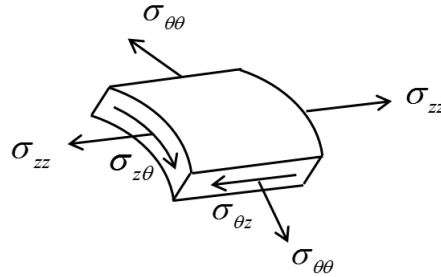


Figure 2.8: Schematic representation of hoop stress  $\sigma_{\theta\theta}$ , longitudinal stress  $\sigma_{zz}$  and shear stress  $\sigma_{z\theta}$  on a shell element

Similarly, in Luco's paper [18], some stresses of interest are also given in terms of Green's functions. They are derived by taking the derivatives of the displacements, which are assumed to be time- and space-harmonic as shown in (2.30). This process is omitted in this thesis and only the transformation matrices are given.

$$\begin{bmatrix} \Sigma_{zz} \\ \Sigma_{\theta\theta} \\ 2\Sigma_{z\theta}/(1-\nu) \end{bmatrix} = a \int_0^{2\pi} \mathbf{H}_2(\theta, \theta') \cdot \mathbf{Q}_2(\theta') d\theta' \quad (2.40)$$

where the Green's function

$$\mathbf{H}_2(\theta, \theta') = \frac{1}{2\pi a(1-\nu^2)} \left(\frac{a}{h}\right) \sum_{n=-\infty}^{+\infty} \mathbf{E}_n \mathbf{A}_n^{-1} \mathbf{B}_n e^{in(\theta-\theta')} \quad (2.41)$$

relates the stresses and outside tractions of the shell, in which

$$\mathbf{E}_n = \begin{bmatrix} -ik_z a & i\nu n & \nu \\ -i\nu k_z a & in & 1 \\ in & -ik_z a & 0 \end{bmatrix} + \left(\frac{\hat{r}}{a}\right) \begin{bmatrix} 0 & i\nu n & (k_z a)^2 + \nu n^2 \\ 0 & in & \nu(k_z a)^2 + n^2 \\ 0 & -ik_z a & -2(k_z a)n \end{bmatrix} \quad (2.42)$$

Depending on the location of interest ( $\hat{r} = h/2$  on the outside wall and  $\hat{r} = -h/2$  on the inside wall), stresses at any depth of the cross-section can be easily found by applying the transformation matrix  $\mathbf{E}_n$ . These stresses are visualized in figure 2.8.

## 2.4 Summary

In this chapter, theories related to the indirect boundary element method are presented. The chapter starts with a physical explanation of the method. For a linear elastic and homogeneous half-space, in the presence of a cavity (or a tunnel), a scattered wave field is produced due to any excitation of the system. The scattered field can be represented by a number of sources with known positions but unknown amplitudes. In order to find the unknown amplitudes of these sources, the 2.5D Green's functions for a half-space are employed in conjunction with the stress-free boundary conditions at the cavity (or tunnel inside) in case of seismic excitation.

The 2.5D Green's functions are essentially steady state solutions of the half-space subjected to a spatially varying line load, which requires considering the half-space to be infinitely long and invariant in the longitudinal direction. They automatically satisfy the boundary conditions, which are stress-free boundary conditions at the half-space surface and radiation conditions at infinity. The 2.5D Green's functions consist of terms related to the full-space, and terms related to the surface. The surface-related terms are needed to satisfy the stress-free boundary conditions at the free-surface, and are formed by considering sufficiently many wavenumbers. The surface-related terms expressed in integrands are integrated with horizontal wavenumbers following a numerical integration routine, which has improved the convergence of these surface-related terms and the satisfaction of stress-free boundary conditions at the half-space surface.

In terms of the tunnel modelling, Donnell theory for thin cylindrical shells is employed. An coupled eighth-order equation of motion describing the dynamic behaviour of a thin shell is given. Assuming the loading and the response to be both spatially harmonic and time harmonic, the relation between the displacement of the shell and the net loading is established, which is essentially the Green's function for the shell. The resulting response is a superposition of sufficiently many harmonic modes.

In chapter 3 and chapter 4, coupling forms of indirect boundary integrals are given, relying on the Green's functions for a half-space and Green's functions for the shell which have been discussed in this chapter.

# Chapter 3

## Model validation: scattering of P waves by a tunnel embedded in a half-space using indirect BEM

In this chapter, the BEM model is adapted to calculate the half-space response due to three-dimensional harmonic P waves excitation. The half-space with an embedded cavity will be first discussed. Secondly, a tunnel is modelled using the Donnell shell theory to replace the cavity. The purpose of this chapter is to test the performance and verify the correctness of the BEM model.

### 3.1 A cavity embedded in a half-space

#### 3.1.1 Model, governing equations and boundary conditions

An infinitely long circular cylindrical cavity of radius  $R_1 = 5\text{m}$  is buried at a depth  $H = 4.545R_1$  in a homogeneous, isotropic and linear elastic half-space. The axis of the cavity is assumed to be parallel to the  $z$  axis. The half-space with the embedded cavity is subjected to non-vertically incident ( $\theta_v = 30^\circ$ ) P harmonic waves impinging in the direction of the cavity axis ( $\theta_h = 0^\circ$ ), as shown in figure 3.1. The homogeneous soil has a mass density  $\rho_s = 2.664 \times 10^3 \text{ kg/m}^3$ , a modulus of elasticity  $E_s = 7.567 \times 10^9 \text{ N/m}^2$  and a Poisson's ratio  $\nu_s = 0.333$ . The frequency of the excitation is such that dimensionless frequency  $\eta = \omega R_0 / \pi c_s = 0.105$  (equal to 10.8 Hz).

A schematic representation of the model is shown in Fig.3.1. The coordinate system used here complies with the one used before. The global coordinate system is centered at  $(0, 0)$  at the ground surface and the origin of local coordinate coincides with the center of the cavity. In this case, receivers are chosen to be placed at the surface of the cavity. And the sources are placed at a radius slightly smaller than the cavity radius  $R_1$  according to relation [19]

$$R_s = R_1 - 3 \frac{2\pi R_1}{N_o} \quad (3.1)$$

Obviously, an increase in observation points will result in an decrease of distance between the sources and observations. A sufficient number of sources ( $N_s$ ) and a sufficient number of observations ( $N_o$ ) are needed to ensure the convergence of the results. However,

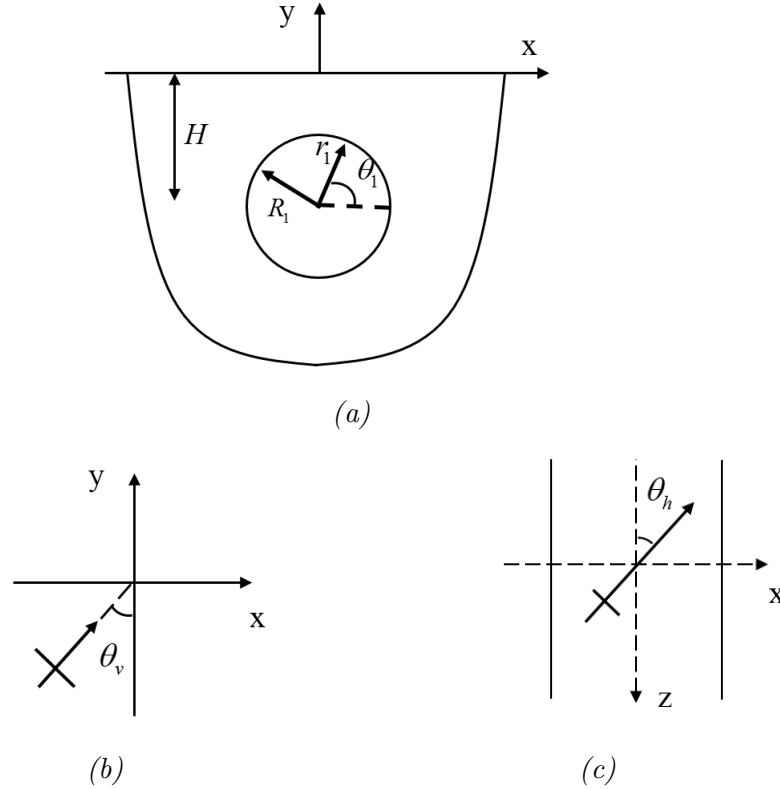


Figure 3.1: Schematic representation of a cylindrical tunnel embedded in a homogeneous half-space subjected to oblique incident P waves: (a) cross-section of the model; (b) vertical incident angle; (c) horizontal incident angle

unreasonably too many observations can result in too close distances between the sources and the observations according to (3.1) which can cause singularity problems discussed in chapter 2.

In the following results, displacements are normalized by the amplitude  $A$  of the incident P-wave at the origin  $(0,0)$ , i.e.,  $U = |u/A|$ . Also, all of the stress components are normalized in the way  $\Sigma = |\Sigma/(\omega\rho c_s A)|$ .

### 3.1.2 Formulation using indirect BEM

The procedure to solve for the seismic wave field using the indirect boundary element method has been physically explained at the beginning of chapter 2, and will be discussed here with explicit expressions.

As stated, in case of seismic excitation, due to the presence of the cavity, scattered waves are produced, which are represented by a group of sources with known positions but unknown amplitudes. To solve the amplitudes of these sources, the traction-free boundary conditions at the cavity surface is employed. Recalling Eq.(3.2), the tractions from the scattered field  $\mathbf{T}^{\text{sc}}$  are written in terms of the tractions from the free field

$$r_1 = R_1, \mathbf{T}^{\text{sc}} = -\mathbf{T}^{\text{free}} \quad (3.2)$$

This is a special case which the stress boundary integral Eq.(2.6) satisfies. In this case, the observations are located at the cavity surface. The stresses at one observation point

at the boundary  $r_1 = R_1$  are

$$r_1 = R_1, \boldsymbol{\sigma}^{\text{sc}} = \begin{bmatrix} \sigma_{rr}^{\text{free}} \\ \sigma_{r\theta}^{\text{free}} \\ \sigma_{rz}^{\text{free}} \end{bmatrix} \quad (3.3)$$

where only the stresses on the cavity surface are involved, meaning that the full dimension of  $6 \times 3$  matrix of 2.5 D Green's functions for stresses  $\mathbf{H}(\mathbf{x}, \mathbf{x}_s)$  is reduced to  $3 \times 3$ .

Next, in order to solve the amplitudes of the unknown sources numerically, the integral Eq.(2.6) is discretized by replacing the ideal continuously distributed sources by a number ( $N_s$ ) of sources. These sources act the source points  $\mathbf{x} = \mathbf{x}_{sj}$  ( $j = 1, \dots, N_s$ ) located on the path  $L_0$ . In addition, the integrals should be written for a set of observation points  $\mathbf{x} = \mathbf{x}_{si}$  ( $i = 1, \dots, N_o$ ) located on the cavity surface. In the end, the resulting set of linear algebraic equations can be written in the form

$$\begin{bmatrix} \boldsymbol{\sigma}^{\text{sc}}(\mathbf{x}_{o,1})_{3 \times 1} \\ \boldsymbol{\sigma}^{\text{sc}}(\mathbf{x}_{o,2})_{3 \times 1} \\ \vdots \\ \boldsymbol{\sigma}^{\text{sc}}(\mathbf{x}_{o,N_o})_{3 \times 1} \end{bmatrix} = \begin{bmatrix} \mathbf{H}(\mathbf{x}_{o,1}, \mathbf{x}_{s,1})_{3 \times 3} & \mathbf{H}(\mathbf{x}_{o,1}, \mathbf{x}_{s,s})_{3 \times 3} & \dots & \mathbf{H}(\mathbf{x}_{o,1}, \mathbf{x}_{s,N_s})_{3 \times 3} \\ \mathbf{H}(\mathbf{x}_{o,2}, \mathbf{x}_{s,1})_{3 \times 3} & \mathbf{H}(\mathbf{x}_{o,2}, \mathbf{x}_{s,2})_{3 \times 3} & \dots & \mathbf{H}(\mathbf{x}_{o,2}, \mathbf{x}_{s,N_s})_{3 \times 3} \\ \vdots & \vdots & \dots & \vdots \\ \mathbf{H}(\mathbf{x}_{o,N_o}, \mathbf{x}_{s,1})_{3 \times 3} & \mathbf{H}(\mathbf{x}_{o,N_o}, \mathbf{x}_{s,2})_{3 \times 3} & \dots & \mathbf{H}(\mathbf{x}_{o,N_o}, \mathbf{x}_{s,N_s})_{3 \times 3} \end{bmatrix} \begin{bmatrix} \mathbf{F}(\mathbf{x}_{s,1})_{3 \times 1} \\ \mathbf{F}(\mathbf{x}_{s,2})_{3 \times 1} \\ \vdots \\ \mathbf{F}(\mathbf{x}_{s,N_s})_{3 \times 1} \end{bmatrix} \quad (3.4)$$

where the left hand side can be represented by stress related to the free field. The amplitudes of the sources can be easily found by solving the set of linear algebraic equations. Moreover, it can be observed that: (1) adding points of sources will lead to augmentation of columns in the matrix related to Green's functions, and the number of unknown amplitudes; (2) adding points of observations/receivers will result in an augmentation of rows in the Green's function matrix, and stresses at the observations; (3) assuming  $N_o$  observation points and  $N_s$  source points are used, the stress vector will have a  $3N_o \times 1$  dimension, and vector related to unknown amplitudes will have an  $3N_s \times 1$  dimension. Therefore, the Green's function matrix will have the dimension  $(3N_o) \times (3N_s)$ . Note that the number of sources and the number of observations do not have to be the same, which is proven in the next section.

### 3.1.2.1 Wave fields

#### Free field

The free field motion is the motion of the half-space in the absence of the tunnel, which consists of the incident waves and the reflected (from the free surface) waves as shown in equation (2.1). Displacements related to three dimensional pressure wave field are given with explicit expressions from Zhao's work [20] which are listed in Appendix B. Stresses are derived from the displacements again using the well-known constitutive relation.

#### Scattered field

With the free field known as an input, in order to compute the total field, one has to determine the scattered field. To do so, the unknown amplitude of the sources are determined by using Eq.(3.4), which involves computing the stresses related to the free field at

the positions of the receivers (cavity surface) and adding a minus sign according to the stress-free boundary condition (3.2). Once the amplitudes of the sources are found, at any point in the half-space, displacements related to the scattered field can be computed using equation (2.4), and stresses related to the scattered field can be computed using equation (2.6).

### Total field

In the end, displacements or stresses from free field and scattered field must be summed up to complete the total wave field.

## 3.1.3 Convergence tests and results

### 3.1.3.1 Convergence tests

In the previous chapter, the convergence of the 2.5D Green's functions has been improved by using the numerical integration routine to evaluate the surface-related integrals. Besides, a convergence test of the model must also be conducted to make sure that the model produces unique and accurate results. Because the numerical results depend in principle on the locations, and the number of sources ( $N_s$ ) and observations ( $N_o$ ). In the following, results are calculated with the convergence of the Green's functions satisfied. Responses in the frequency domain will be shown with the factor  $e^{i\omega t}$  omitted and understood. Also, in this part, the number of observations and the number of sources are equal, meaning that we are solving a square matrix in Eq.(3.4).

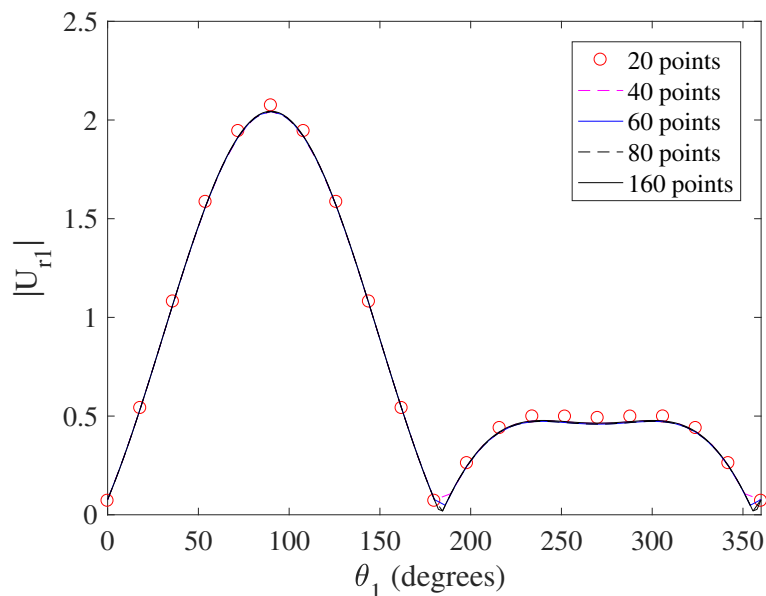


Figure 3.2: Normalized radial displacement at the cavity  $|U_{r_1}|$  for different number of sources and receivers

Fig.3.2 shows the amplitude of the normalized radial displacement  $|U_{r_1}|$  at the cavity surface  $r_1 = R_1$  due to the 3D P-waves excitation. The comparison is made by using different number of sources and receivers. With the increase of the sources and receivers, the radial displacements tends to approach certain values. As long as the number is



large enough, adding sources and receivers will only make a small difference in decimal precision. This process is called convergence. In this case, using 20 sources and 20 receivers are not sufficient for converged results, while using 40 sources and receivers gives the same results as those using 160 sources and receivers.

We conclude that 40 sources and 40 receivers are sufficient enough for the convergence in the current case study.

### 3.1.3.2 Verification

Using the stated parameters and employing the proposed method, more results are calculated and compared to those from Zhao *et al* [20]. Displacements are compared at the half-space surface  $y = 0$  and at the cavity surface  $r_1 = R_1$ . Moreover, the hoop stress at the cavity surface is also compared. Results are calculated using 160 sources and 160 receivers.

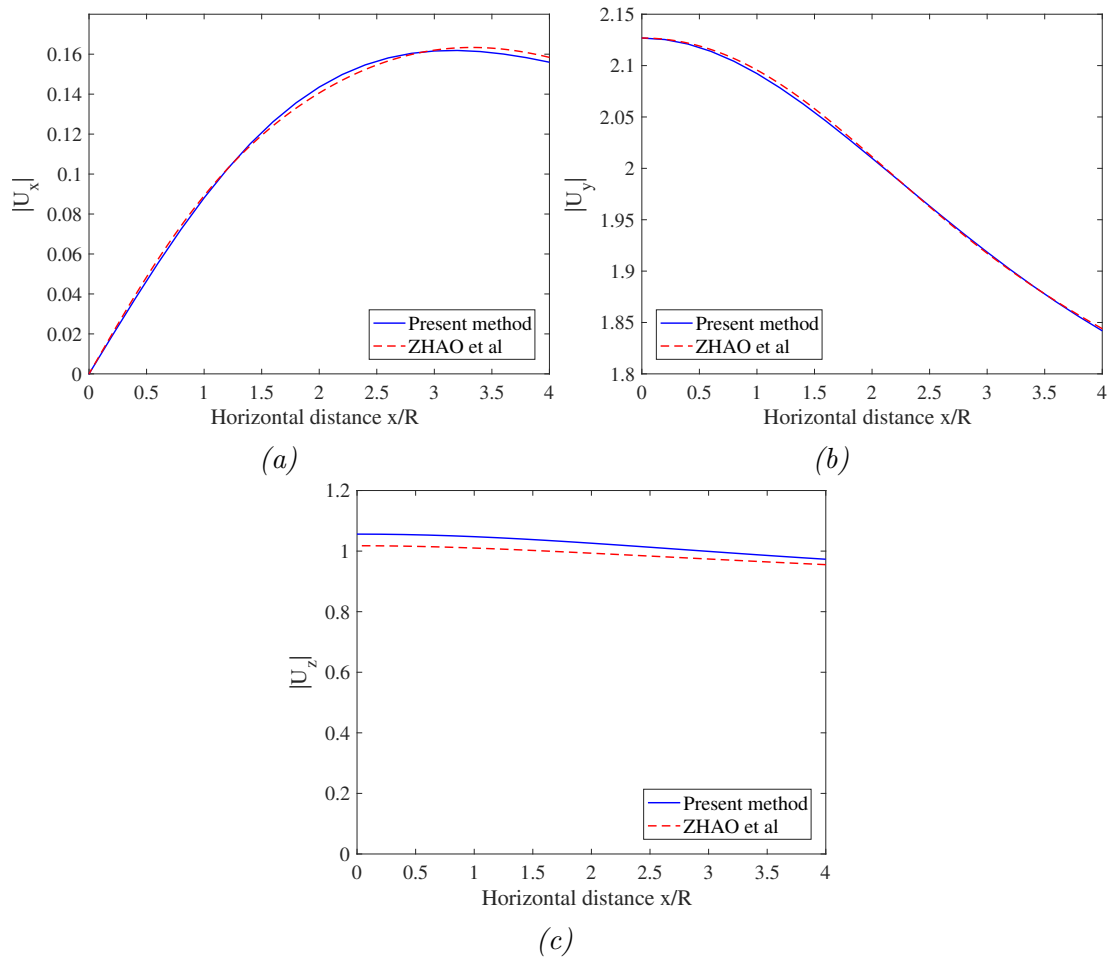


Figure 3.3: Normalized displacement (a)  $|U_x|$ , (b)  $|U_y|$  and (c)  $|U_z|$  at the half-space surface  $y = 0$  with a cavity

Figure 3.3 shows the comparison of normalized displacements  $|U_x|$ ,  $|U_y|$  and  $|U_z|$  on the surface of the half-space ( $y = 0$ ). Since the horizontal incident angle  $\theta_h = 0^\circ$ , the response is also symmetric with respect to the vertical  $y$  axis. Therefore, only half of the responses are plotted. Displacements are calculated up to the distance equal to 4 times

the cavity radius.

It is shown that present results are in perfect agreement with those obtained by Zhao et al in  $x$  and  $y$  direction. The difference in  $z$  direction is less than 4%.

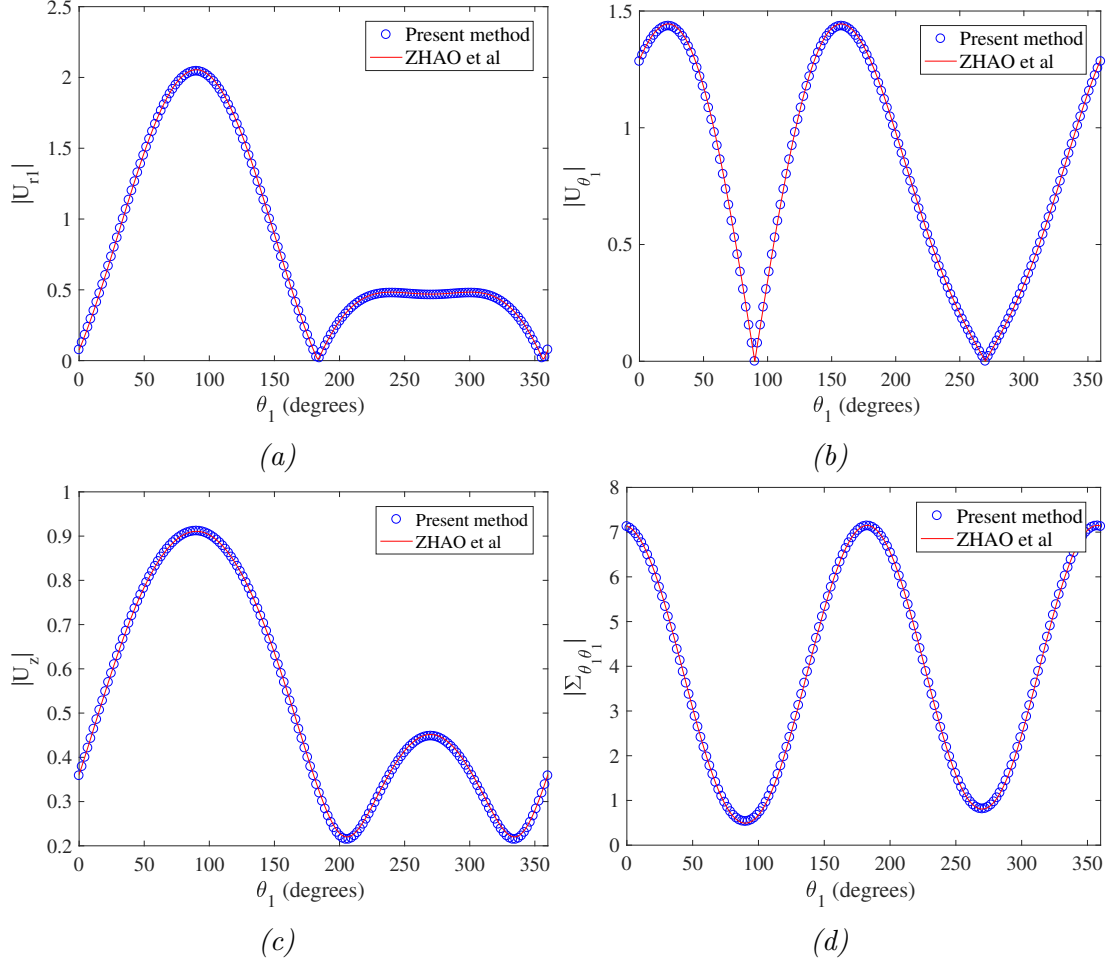


Figure 3.4: Normalized displacement (a)  $|U_{r1}|$ , (b)  $|U_{\theta_1}|$ , (c)  $|U_z|$  and hoop stress  $|\Sigma_{\theta_1\theta_1}|$  at the cavity surface  $r_1 = R_1$ .

Fig 3.4 (a)(b)(c) show the comparison of normalized radial displacements  $|U_{r1}|$ , angular displacement  $|U_{\theta_1}|$  and longitudinal displacement  $|U_z|$  at the cavity surface  $r_1 = R_1$ . Also, the comparison for normalized hoop stress  $|\Sigma_{\theta_1\theta_1}|$  is shown in (d). Since the horizontal incident angle  $\theta_h = 0^\circ$ , all the responses at the cavity surface are symmetric with  $\theta_1 = 90^\circ$  and  $270^\circ$ . Maximum values of  $U_{r1}$  and  $U_z$  are found at the top point  $\theta_1 = 90^\circ$ , which is probably due to the waves reflected from the free-surface. At  $\theta_1 = 90^\circ$  and  $270^\circ$ , no circumferential deformation occurs due to the symmetry. However, the hoop stress can still occur because of the radial deformation.

The results using the present method show perfect agreements with those obtained by Zhao *et al* [20]. The result comparisons at the cavity are better than the ones at the surface, probably because the responses are very close to the source position.

### 3.1.3.3 Using half of the sources

Up to now, the correctness of the BEM model has been proven. In order to speed up the calculation, results have also been calculated using a half number of the sources rather than the same number as the receivers, i.e.,  $N_s = 0.5N_o$ . In fact, using half of the sources is not a new idea and was proposed by Luco *et al* [10]. Using half of the sources is proven to be equally accurate and very efficient. By using half of the sources, half of the calculation time can be directly reduced, because the matrix related to Green's functions in Eq.(3.4) is changed to a non-square matrix.

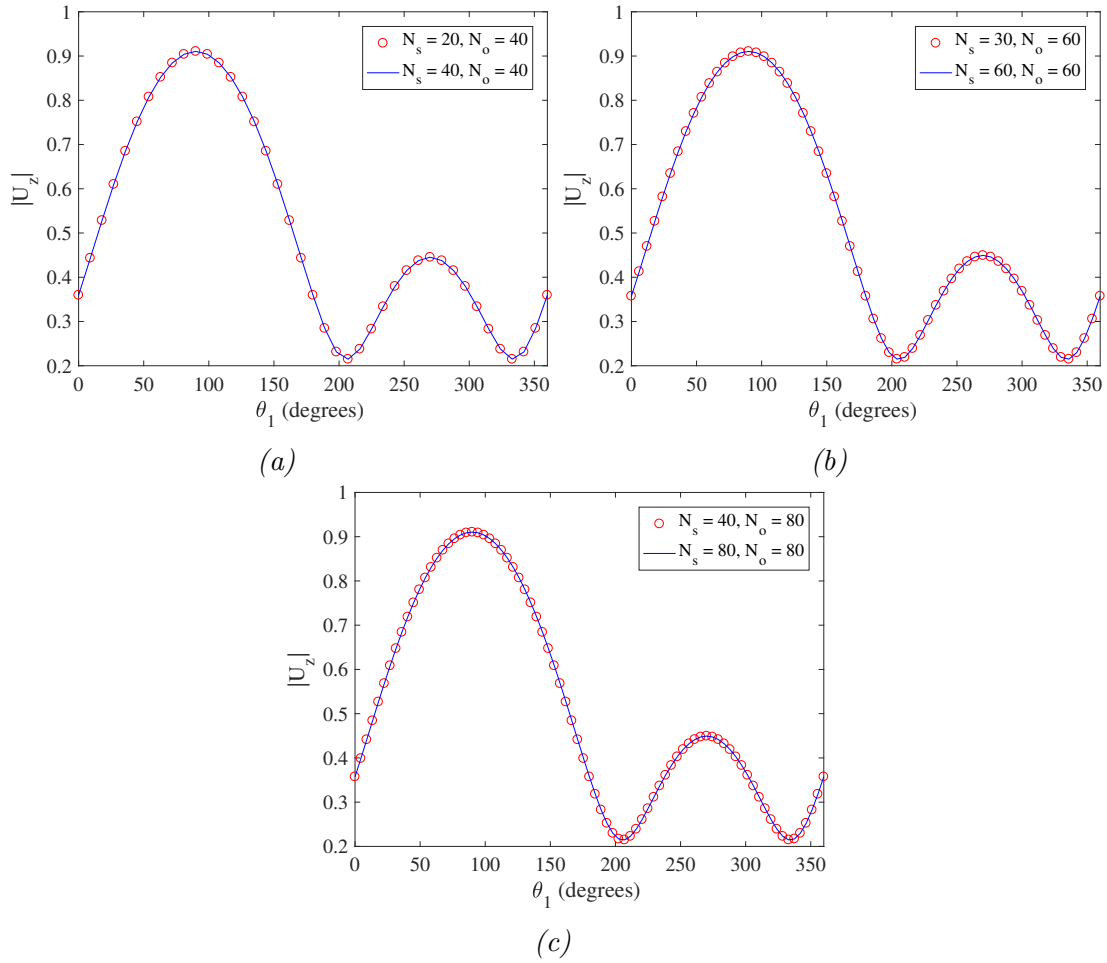


Figure 3.5: Normalized displacement  $|U_z|$  at the cavity surface  $r_1 = R_1$  using different number of sources and receivers ( $N_s =$  number of sources,  $N_o =$  number of observations)

In figure 3.5, results calculated using half of the sources are compared to those using the same number of sources and receivers. Normalized displacements  $|U_z|$  are computed for 3 scenarios where the number of observations (receivers) equals to 40, 60 or 80. Comparisons are made within each scenario. It is clearly shown that results using half of the sources are the same as those using the full sources, within tolerance of decimal precision. Using half of the sources is equally efficient regardless of the number of observations. This is an important finding because using half of the sources means reducing the calculation time by half, bring a high efficiency in calculation. Furthermore, 20 sources and 40 receivers are proven to give converged and accurate good results.

The conditioning numbers of the matrices to be solved in equation (3.4) are:  $1.33 \times 10^4$  for a non-square matrix and  $1.18 \times 10^9$  for a square matrix in the case of 40 receivers are used;  $1.15 \times 10^4$  for a non-square matrix and  $3.32 \times 10^7$  for a square matrix in the case of 60 receivers are used;  $1.0 \times 10^4$  for a non-square matrix and  $2.95 \times 10^7$  for a square matrix in the case of 80 receivers are used.

## 3.2 A tunnel embedded in a half-space

### 3.2.1 Model, governing equations and boundary conditions

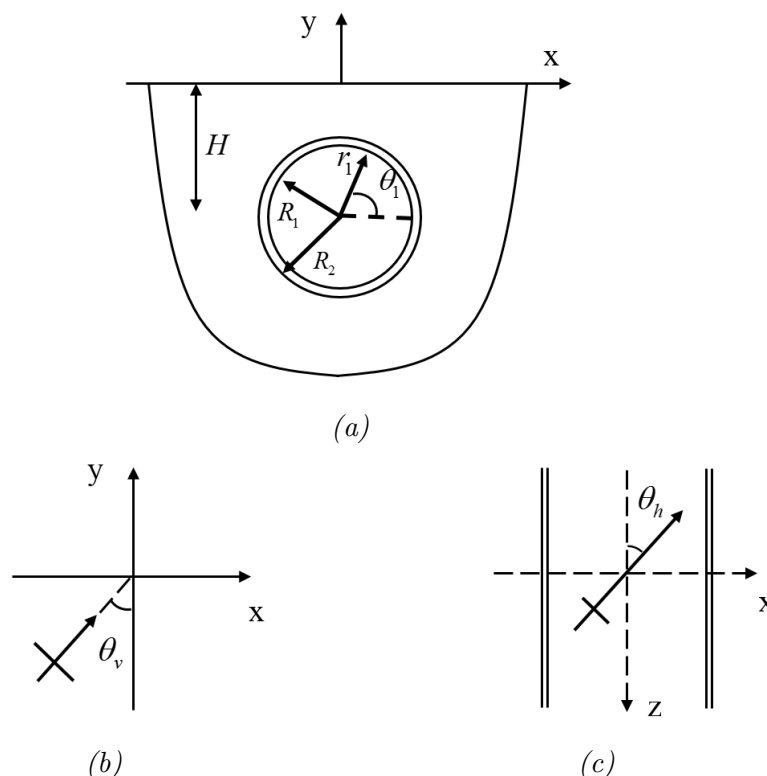


Figure 3.6: Schematic representation of a cylindrical cavity embedded in a homogeneous half-space subjected to oblique incident P waves: (a) cross-section of the model; (b) vertical incident angle; (c) horizontal incident angle

In this part, instead of a cavity, a tunnel is embedded in a homogeneous, isotropic and linear elastic half-space. A schematic representation of the model is shown in Fig.3.6.

The tunnel is modeled as an infinitely long circular cylindrical shell, with an inner radius  $R_1 = 0.9091R_2$  and an outer radius  $R_2 = 5\text{m}$  buried at a depth  $H = 4.545R_1$  below ground surface. The axis of the tunnel is assumed to be parallel to the  $z$  axis. The half-space with the embedded cavity is subjected to the same non-vertically incident ( $\theta_v = 30^\circ$ ) P harmonic waves impinging in the direction of the tunnel axis ( $\theta_h = 0^\circ$ ), as shown in figure 3.6. The material properties of the half-space are the same as those before: density  $\rho_s = 2.664 \times 10^3 \text{ kg/m}^3$ , modulus of elasticity  $E_s = 7.567 \times 10^9 \text{ N/m}^2$  and Poisson's ratio  $\nu_s = 0.333$ . The frequency of the excitation is such that dimensionless frequency  $\eta = \omega R_0 / \pi c_s = 0.105$  (equal to 10.8 Hz).

The coordinate system used here complies with the one used before. The global coordinate system is centered at  $(0,0)$  at the ground surface and the origin of local coordinate coincides with the center of the tunnel.

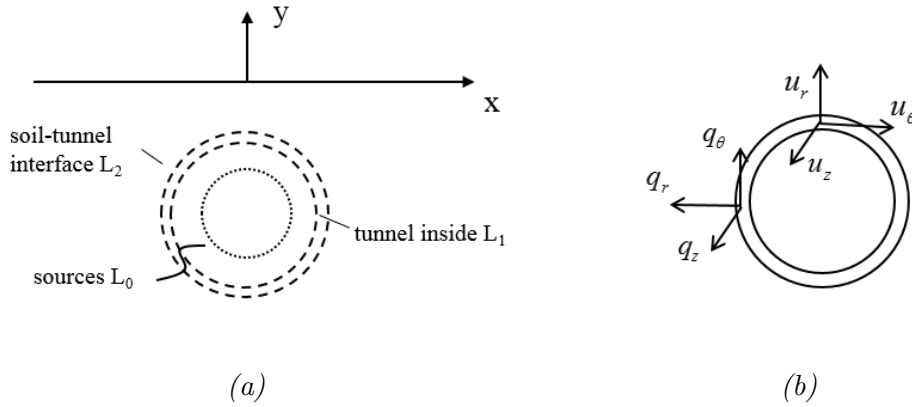


Figure 3.7: (a) Position to be occupied by a shell in the half-space; (b) Green's functions for a shell

For the complete tunnel-soil system, the tunnel is modeled by a cylindrical shell and the soil by elastic continuum of a half-space surrounding the tunnel. The boundary conditions and interface conditions of the whole system are stated below:

1. On the inside of the shell  $\mathbf{x} \in L_1$  (as shown in Fig. 3.7 and Fig.4.3), the traction-free boundary condition must be satisfied, in case of seismic excitation;
2. At the interface between the tunnel shell and the soil continuum  $\mathbf{x} \in L_2$ , displacements must be compatible and tractions must be in equilibrium;
3. On the half-space free surface  $y = 0$ , the stresses must be equal to zero (also known as traction-free condition);
4. At the infinity, the displacement of the soil continuum must decay to zero (the radiation condition).

The formulation of governing equations presented here are based on Luco's work (except the Green's functions) [18]. As discussed in chapter 2, under the seismic excitation, the total wave field in the half-space consists of the free field and the scattered wave field. The total displacement vector  $\mathbf{U}_1(\mathbf{x})$  and the total traction vector  $\mathbf{T}_1(\mathbf{x})$  are written in the form

$$\mathbf{U}_1(\mathbf{x}) = \mathbf{U}_1^{\text{free}}(\mathbf{x}) + \mathbf{U}_1^{\text{sc}}(\mathbf{x}) \quad (3.5)$$

$$\mathbf{T}_1(\mathbf{x}) = \mathbf{T}_1^{\text{free}}(\mathbf{x}) + \mathbf{T}_1^{\text{sc}}(\mathbf{x}) \quad (3.6)$$

where  $\mathbf{U}_1^{\text{sc}}(\mathbf{x})$  and  $\mathbf{T}_1^{\text{sc}}(\mathbf{x})$  are the scattered displacement and traction vectors, respectively, for the soil medium;  $\mathbf{U}_1^{\text{free}}(\mathbf{x})$  and  $\mathbf{T}_1^{\text{free}}(\mathbf{x})$  are the displacement and traction vectors related to the free field. Capitalization of letters denotes the frequency domain. Superscript '1' denotes the soil domain while superscript '2' in the following denotes the shell domain. Equation (3.5) and (3.6) hold for the position within the soil medium (including the boundary). The soil should satisfy the traction-free boundary conditions on the free

surface and the radiation conditions at infinity, which is automatically realized by using the Green's functions for a half-space. Specifically, at the interface  $L_2$  between the shell and the exterior medium, the continuity of displacement and the equilibrium of traction are applied:

$$\mathbf{U}_1(\mathbf{x}_o) = \mathbf{U}_2^{\text{out}}(\mathbf{x}_o), \quad \mathbf{x}_o \in L_2 \quad (3.7)$$

$$\mathbf{T}_1(\mathbf{x}_o) + \mathbf{T}_2^{\text{out}}(\mathbf{x}_o) = \mathbf{0}, \quad \mathbf{x}_o \in L_2 \quad (3.8)$$

where  $\mathbf{U}_2^{\text{out}}(\mathbf{x}_o)$  and  $\mathbf{T}_2^{\text{out}}(\mathbf{x}_o)$  are the displacement and traction vectors, respectively, at the exterior surface of the shell. Vector  $\mathbf{x}_o = (x_o, y_o, z_o)$  denotes the coordinates of a number ( $N_o$ ) of observation points located on the interface  $L_2$  between the soil and the tunnel.

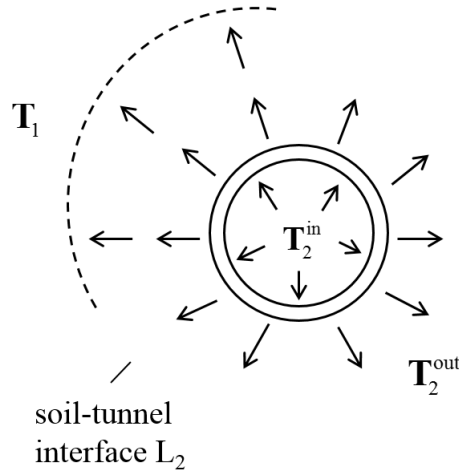


Figure 3.8: Traction equilibrium and net loading on the shell

### 3.2.2 Half-space domain

The scattered field in the soil is represented as resulting from a number of sources acting in the half-space, which are located slightly inside the region to be occupied by the shell. Within the soil medium, the displacement related to the scattered field is written in discretized matrix form

$$\mathbf{U}_1^{\text{sc}}(\mathbf{x}) = \int_{L_0} \mathbf{G}_1(\mathbf{x}, \mathbf{x}_s) \mathbf{F}(\mathbf{x}_s) dl(\mathbf{x}_s) \quad (3.9)$$

Similarly, for the traction related to the scattered field

$$\mathbf{T}_1^{\text{sc}}(\mathbf{x}) = -\boldsymbol{\sigma}_1^{\text{sc}}(\mathbf{x}) = - \int_{L_0} \mathbf{H}_1(\mathbf{x}, \mathbf{x}_s) \mathbf{F}(\mathbf{x}_s) dl(\mathbf{x}_s) \quad (3.10)$$

where  $\mathbf{G}_1$  and  $\mathbf{H}_1$  are matrices of 2.5D Green's functions for displacements and stresses of the half-space, respectively; and  $\mathbf{F}(\mathbf{x}_s)$  represents the unknown amplitudes of the sources whose position and the direction are known. The contour  $L_0$  corresponds to the source position. Equation (3.9) and (3.10) hold equally for displacements and stresses at the interface between the soil and the tunnel.

### 3.2.3 Cylindrical shell domain

For the shell component, the displacements at the shell outside surface and the net stresses can be related through equation (2.38). For the hyperloop problem where there is gravity pressure acting at the shell inside, the net loading  $\mathbf{Q}_2(\theta')$  in (2.38) has to be modified.

$$\mathbf{Q}_2(\theta') = \mathbf{T}_2^{\text{out}}(\theta') - \mathbf{T}_2^{\text{in}}(\theta') \quad (3.11)$$

where

$$\mathbf{T}_2^{\text{in}}(\theta') = \mathbf{0} \quad (3.12)$$

$\mathbf{T}_2^{\text{out}}(\theta')$  and  $\mathbf{T}_2^{\text{in}}(\theta')$  represent the traction on the outer surface and inner surface of the shell, respectively.

Using equations(3.5), (3.6), (3.8), (3.9), (3.10), (3.11),(3.12) the displacement fields  $\mathbf{U}_1(\mathbf{x}_o)$  from the half-space and  $\mathbf{U}_2^{\text{out}}(\mathbf{x}_o)$  from the shell at the soil-tunnel interface  $\mathbf{x}_o \in L_2$  can be written [18]

$$\mathbf{U}_1(\mathbf{x}_o) = \mathbf{U}_1^{\text{free}}(\mathbf{x}_o) + \int_{L_0} \mathbf{G}_1(\mathbf{x}_o, \mathbf{x}_s) \mathbf{F}(\mathbf{x}_s) dl(\mathbf{x}_s) \quad (3.13)$$

$$\mathbf{U}_2(\mathbf{x}_o) = - \int_S \mathbf{G}_2(\mathbf{x}_o, \mathbf{x}'_o) \cdot \left[ \mathbf{T}_1^{\text{free}}(\mathbf{x}_o) - \int_{L_0} \mathbf{H}_1(\mathbf{x}_o, \mathbf{x}_s) \mathbf{F}(\mathbf{x}_s) dl(\mathbf{x}_s) \right] dl(\mathbf{x}'_o) \quad (3.14)$$

where  $\mathbf{x}_s \in L_0$  represents the position of the sources;  $\mathbf{x}_o \in L_2$  denotes the position of the observations;  $\mathbf{x}, \mathbf{x}' \in S$  denotes the shell. It can be seen that the vector  $\mathbf{F}(\mathbf{x}_s)$ , the unknown amplitude of the sources appears in both equations, meaning that the thin shell and the half-space are coupled.

Next, in order to apply the displacement continuity condition, substituting equation (3.13) and (3.14) into (3.7) and rearranging terms leads to

$$\int_{L_0} \mathbf{B}(\mathbf{x}_o, \mathbf{x}_s) \mathbf{F}(\mathbf{x}_s) dl(\mathbf{x}_s) = \mathbf{D}(\mathbf{x}_o) \quad (3.15)$$

where

$$\mathbf{B}(\mathbf{x}_o, \mathbf{x}_s) = \mathbf{G}_1(\mathbf{x}_o, \mathbf{x}_s) - \int_S \mathbf{H}_1(\mathbf{x}_o, \mathbf{x}_s) \mathbf{G}_2(\mathbf{x}_o, \mathbf{x}'_o) dl(\mathbf{x}'_o) \quad (3.16)$$

and

$$\mathbf{D}(\mathbf{x}_o) = -\mathbf{U}_1^{\text{free}}(\mathbf{x}_o) - \int_S \mathbf{T}_1^{\text{free}}(\mathbf{x}_o) \mathbf{G}_{22}(\mathbf{x}_o, \mathbf{x}'_o) dl(\mathbf{x}'_o) \quad (3.17)$$

Equation (3.15) is the equation to be solved for the unknown amplitudes of sources  $\mathbf{F}(\mathbf{x}_s)$ . To obtain this equation, the continuity of displacements and equilibrium of traction at the interface between the soil and tunnel have been employed. Note that in order to connect displacements and tractions on the shell with those of the soil, it is necessary

to refer these vectors to the same cylindrical coordinates. The coordinate conversion relation has been given in chapter 2. Once the unknown amplitudes have been found, the displacement fields in the soil medium and in the shell can be calculated from equations (3.13) and (3.14). Note that the observation points are now placed to be located on the tunnel-soil interface, which is different from the cavity case.

### 3.2.4 Results

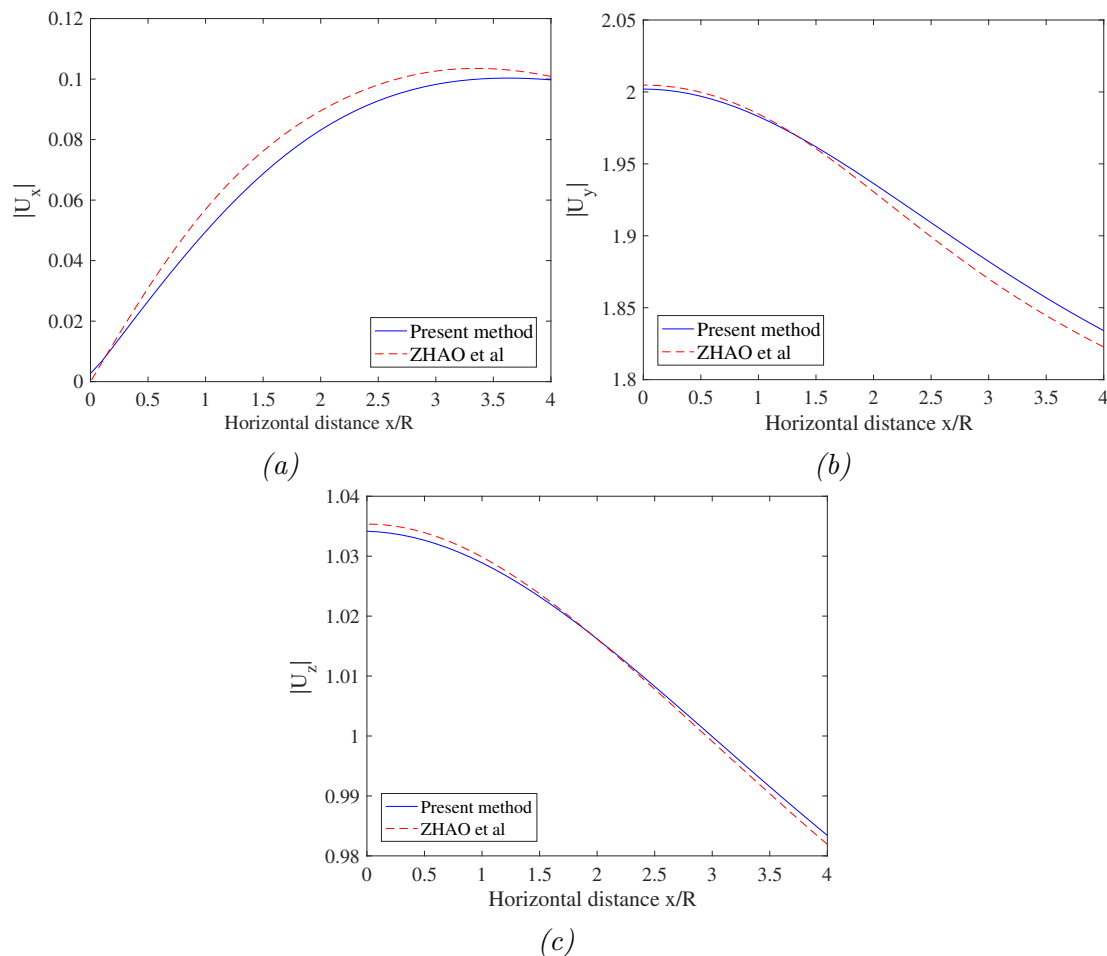


Figure 3.9: Normalized displacements: (a)  $|U_x|$ , (b)  $|U_y|$  and (c)  $|U_z|$  at half-space surface  $y = 0$  with a tunnel

Figure 3.9 shows the comparison of normalized displacements  $|U_x|$ ,  $|U_y|$  and  $|U_z|$  on the surface of the half-space ( $y = 0$ ) in the case there is a tunnel. The displacement components have almost the same shapes as those in Fig.3.3, and smaller amplitudes. The amplitude reduction effect is observed because of a larger stiffness of the tunnel.

Present results are shown to have good agreements with those obtained by Zhao *et al*, with the difference less than 5%. The small differences can be attributed to the different methods in modeling the tunnel.



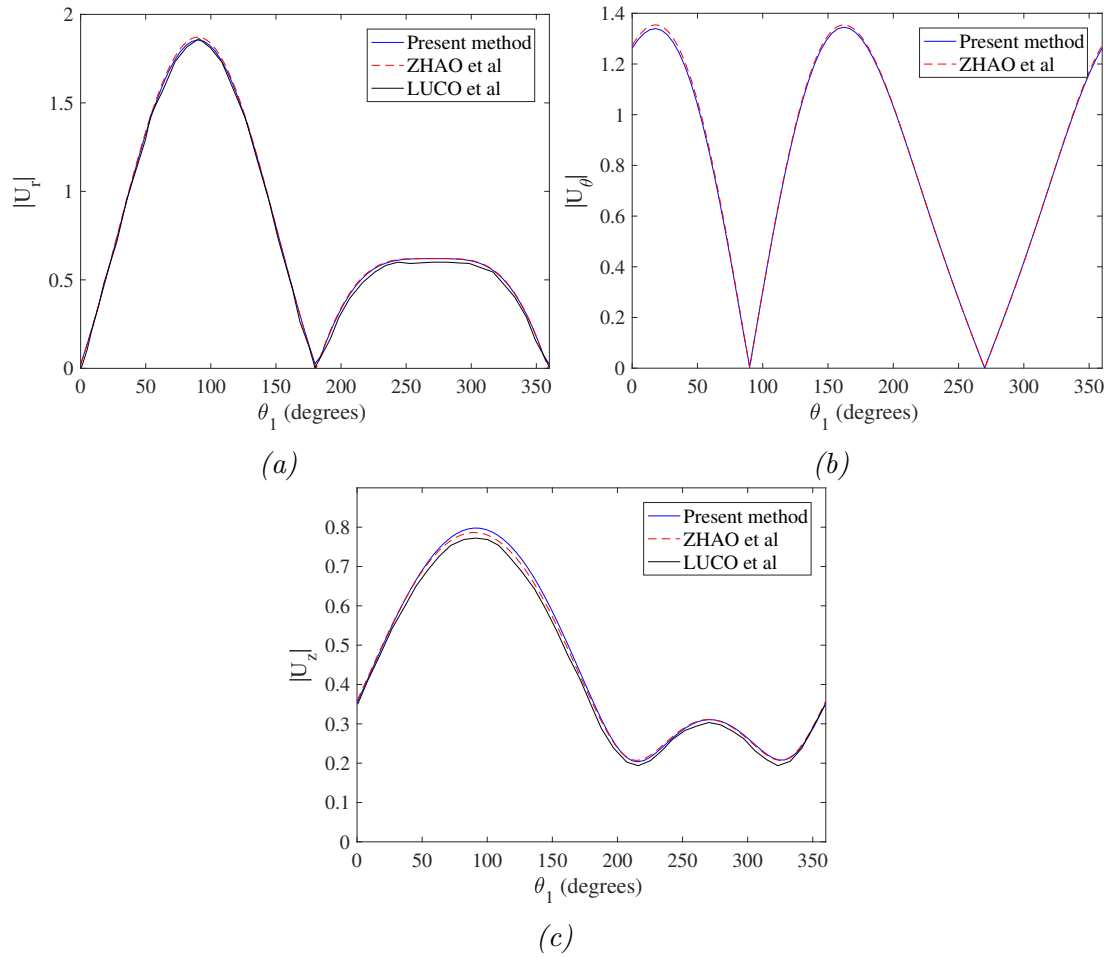


Figure 3.10: Normalized displacements: (a)  $|U_x|$ , (b)  $|U_y|$  and (c)  $|U_z|$  at the tunnel-soil interface  $r = r_o$

Fig 3.10 shows the comparison of normalized radial displacements  $|U_{r1}|$ , angular displacement  $|U_{\theta1}|$  and longitudinal displacement  $|U_z|$  at the soil-tunnel interface  $r_1 = R_2$ . Comparison have been made among results obtained by the current method, Zhao *et al* [20] and Luco *et al* [10] in radial direction and longitudinal direction. The responses are very similar to those in Fig.3.4, but with reduction in amplitudes.

The results using the present method show a perfect agreement with those obtained by Zhao *et al* [20], and those by Luco *et al* [10]. The result comparisons at the tunnel are again better than the ones at the surface.

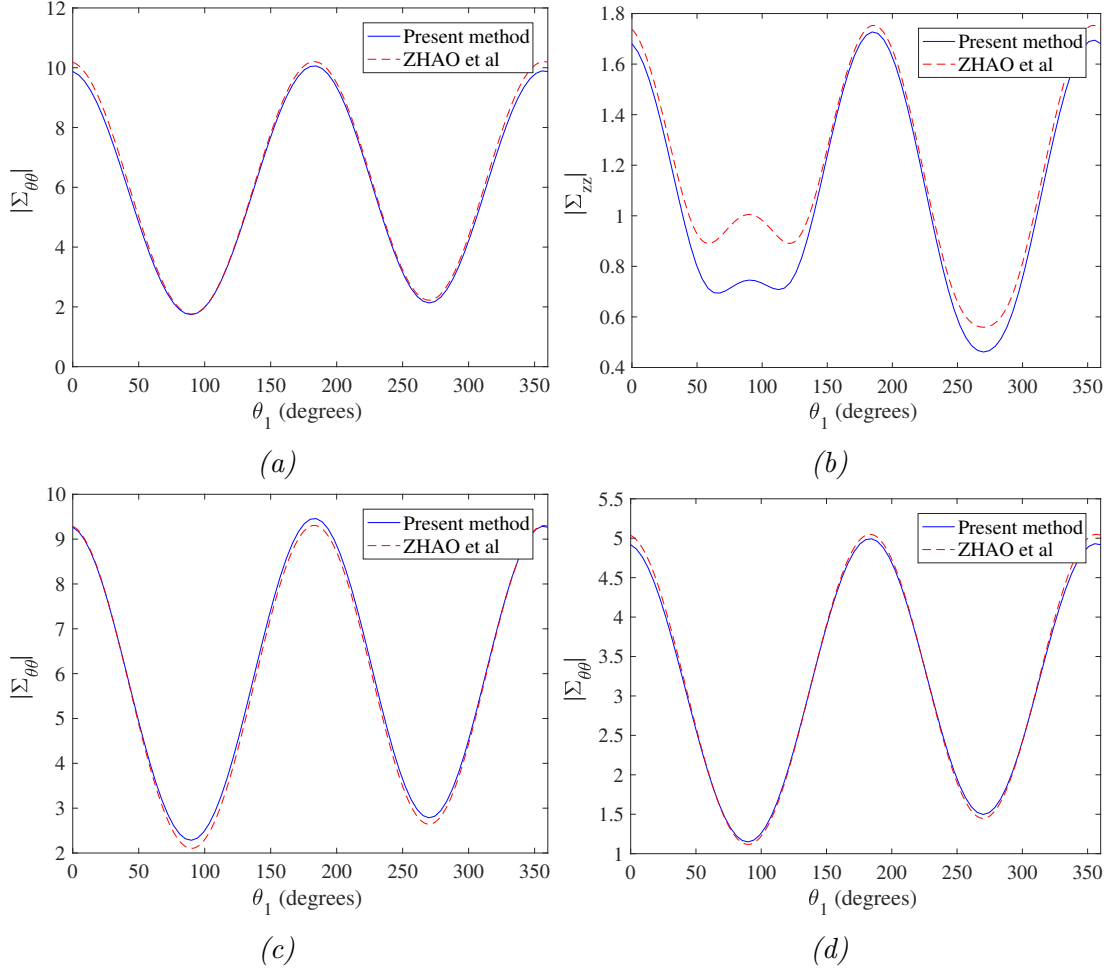


Figure 3.11: Normalized stresses: (a) hoop stress  $\Sigma_{\theta\theta}$  at tunnel centerline  $r = a$ , (b) longitudinal stress  $\Sigma_{zz}$  at tunnel centerline  $r = a$ , (c) hoop stress  $\Sigma_{\theta\theta}$  at tunnel-soil interface  $r = R_2$  from tunnel side, (d) hoop stress  $\Sigma_{\theta\theta}$  at tunnel-soil interface  $r = R_2$  from soil side

Fig.3.11 shows the comparisons of hoop stress around the tunnel centerline, and the comparison of longitudinal stress at the tunnel centerline. Comparing (a) and (c), the hoop stress at the tunnel centerline  $r = a$  is larger than the one at the outside, due to a closer distance to the load. Also, by comparing (c) and (d), it is found that at soil-tunnel interface  $r = R_2$ , there is a discontinuity of hoop stress, because the deformation should be continuous while the Young's modulus is different in the two materials.

The hoop stresses calculated by the present method show a perfect agreement with those obtained by Zhao *et al* [20]. However, a noticeably large difference can be observed in the longitudinal stress comparison. The longitudinal stress reveals the bending behavior of the tunnel, therefore, the bending behaviour is described differently when continuum theory are shell theory are used.

### 3.3 Summary

In this chapter, the scatterings of 3D harmonic seismic P waves by a circular cavity and by a tunnel in a linear elastic half-space are both analysed. In both cases, boundary conditions at the half-space surface and at infinity are the same, however, the existence of the tunnel brings extra interface conditions to be satisfied. Therefore, different governing equations are formulated.

In case of seismic excitations, the total wave field is a summation of free wave field (known) and a scattered wave field. As stated, the scattered wave field is represented by a number of sources with known positions but unknown amplitudes. For the scattering of 3D P waves by a circular cavity, the amplitudes of these sources are found by applying the stress-free boundary conditions at the cavity surface. At the cavity surface, the stresses related to the scattered field are equal to the stresses related to the free field. Together with the Green's functions for stresses in a half-space, the unknown amplitudes of sources are found by solving a set of linear algebraic equations.

Secondly, the scattering of 3D P waves by a tunnel in a linear elastic half-space is analysed. The tunnel is modelled as a thin cylindrical shell. Due to the existence of the tunnel, the formulation to find the unknown amplitudes of sources is different: the responses of the shell and the half-space are analysed independently, and later the continuity conditions of displacements and stresses are imposed at the interface. In the end, a couple form of boundary integral is established for finding the unknown amplitudes of the sources.

In both cases, once the unknown amplitudes of sources are found, responses at any position in the half-space can be found by means of transfer functions (which are essentially Green's functions). Displacements are computed at the half-space surface, at the cavity and at the tunnel, and are compared to those from literature. Results obtained by the current method are shown to have good agreements, which proves the correctness of the method.

Moreover, the performance of the method is analysed. Convergence tests have shown that 40 observations are sufficient enough for describing the dynamic behaviour of the systems in the current case studies. Using half number of sources rather than the same number as the observations has shown an equal accuracy and a much higher efficiency, i.e., 40 observations and 20 sources.

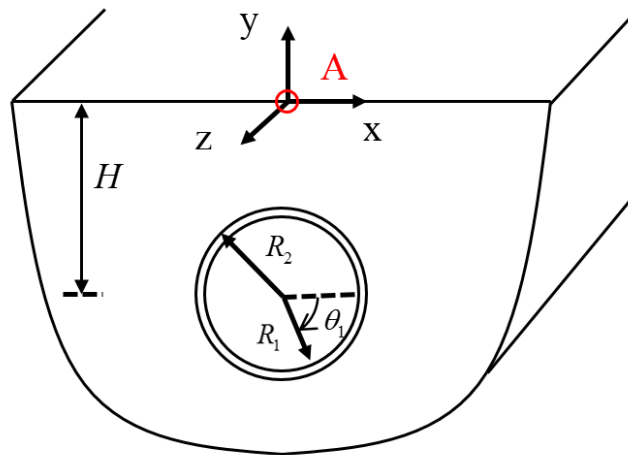


# Chapter 4

## Dynamic response of an embedded tunnel in a half-space subjected to a Hyperloop pod running in the tunnel by indirect BEM

### 4.1 Model description

In figure 4.1, the ground with an embedded tunnel is modelled as a linear elastic, homogeneous and isotropic half-space. The material parameters are the density  $\rho$  and the Lamé constants  $\lambda$  and  $\mu$  with hysteretic damping. The tunnel is modeled as a circular cylindrical thin shell with an inner radius  $R_1$  and an outer radius  $R_2$ , buried at a depth  $H$  below the ground surface. The axis of the tunnel is parallel to the  $z$  axis. A constant moving load with a constant magnitude  $P_0$  and velocity  $V$  is applied at the lower part of the tunnel to represent a hyperloop pod. The material parameters are listed in table 4.1.



(a)

Figure 4.1: Schematic representation of a 3D half-space with an embedded tunnel

Inner radius $R_1$	2.75 m
Outer radius $R_2$	3.0 m
Tunnel wall thickness $t$	0.25 m
Tunnel depth $H$	15 m
Internal load amplitude $P_0$	$8 \times 10^4$ N
Elastic modulus of soil $E_s$	$3 \times 10^7$ N/m <sup>2</sup>
Poisson's ratio of soil $\nu_s$	0.3
Density of soil $\rho_s$	1900 kg/m <sup>3</sup>
Hysteretic damping in soil $\zeta_s$	0.05
Shear wave speed in soil $c_{s,s}$	78 m/s
Elastic modulus of concrete $E_c$	$2.5 \times 10^{10}$ N/m <sup>2</sup>
Poisson's ratio of concrete $\nu_c$	0.2
Density of concrete $\rho_c$	2400 kg/m <sup>3</sup>
Hysteretic damping in concrete $\zeta_c$	0.02
Shear wave speed in concrete $c_{s,c}$	2084 m/s

Table 4.1: Material parameters

## 4.2 Formulation using indirect BEM

### 4.2.1 Loading condition

In order to represent a uniformly distributed load with a constant pressure within the range  $\theta_1 \in [\frac{\pi}{2} - \frac{\pi}{4}, \frac{\pi}{2} + \frac{\pi}{4}]$ , one may apply the Heaviside function  $H(\theta_1)$ . The load exerted on the system has the form

$$p_r(\theta_1, z, t) = \frac{P_0}{R_1 \times \frac{\pi}{2} \times 1} \left\{ H(\theta_1 - \frac{\pi}{4}) - H(\theta_1 - \frac{3\pi}{4}) \right\} \delta(z - Vt) \quad (4.1a)$$

$$p_\theta(\theta_1, z, t) = 0 \quad (4.1b)$$

$$p_z(\theta_1, z, t) = 0 \quad (4.1c)$$

where  $P_0$  represents the magnitude of the gravity force. Equation (4.1) means in the 2D plane  $xoy$ , the gravity force is smeared in the circumferential direction at the lower part of the tunnel within the range  $[\frac{\pi}{4}, \frac{3\pi}{4}]$ , while in the longitudinal direction, it is a point load represented by the Dirac-delta function. Unless specified, the load will have the same form throughout the thesis.

### 4.2.2 Boundary and interface conditions

For the complete tunnel-soil system, the tunnel is modelled by a cylindrical shell and the soil by elastic continuum of a half-space surrounding the tunnel. The boundary conditions and interface conditions of the whole system are stated below:

1. On the inside of the shell  $\mathbf{x} \in L_1$  (as shown in figure 4.2), the stresses are directly equal to the applied loading, in case, the pressure from the hyperloop;

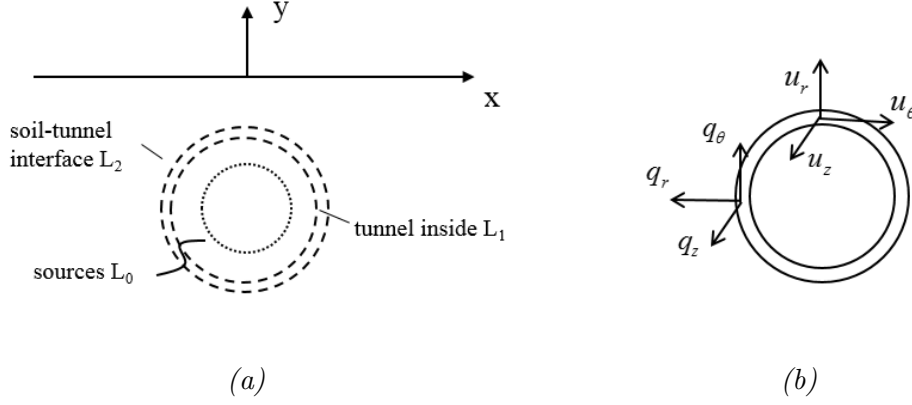


Figure 4.2: (a) Position to be occupied by a shell in the half-space; (b) Green's functions for a shell

2. At the interface between the tunnel shell and the soil continuum  $\mathbf{x} \in L_2$ , displacements must be compatible and tractions must be in equilibrium;
3. On the half-space free surface  $y = 0$ , the stresses must be equal to zero (also known as the traction-free condition);
4. At infinity, the displacements of the soil continuum must decay to zero (the radiation condition).

In case of hyperloop excitation, the total displacement vector  $\mathbf{U}_1(\mathbf{x})$  and the total traction vector  $\mathbf{T}_1(\mathbf{x})$  in the soil are written in the form

$$\mathbf{U}_1(\mathbf{x}) = \mathbf{U}_1^{\text{sc}}(\mathbf{x}) \quad (4.2)$$

$$\mathbf{T}_1(\mathbf{x}) = \mathbf{T}_1^{\text{sc}}(\mathbf{x}) \quad (4.3)$$

where  $\mathbf{U}_1(\mathbf{x})$  and  $\mathbf{T}_1(\mathbf{x})$  are the scattered displacement and traction vectors, respectively, for the soil medium. Capitalization of letters denotes the frequency domain. Superscript '1' denotes the soil domain while superscript '2' denotes the shell domain. Equation (4.2) and (4.3) hold for all the position within the soil medium (including the boundary). The soil should satisfy the traction-free boundary conditions on the free surface and the radiation conditions at the infinity. This is realized by applying a correct form of the Green's functions. Specifically, at the interface between the shell and the exterior medium, the following continuity conditions are applied:

$$\mathbf{U}_1(\mathbf{x}_o) = \mathbf{U}_2^{\text{out}}(\mathbf{x}_o), \quad \mathbf{x}_o \in L_2 \quad (4.4)$$

$$\mathbf{T}_1(\mathbf{x}_o) + \mathbf{T}_2^{\text{out}}(\mathbf{x}_o) = \mathbf{0}, \quad \mathbf{x}_o \in L_2 \quad (4.5)$$

where  $\mathbf{U}_2^{\text{out}}(\mathbf{x}_o)$  and  $\mathbf{T}_2^{\text{out}}(\mathbf{x}_o)$  are the displacement and traction vectors, respectively, at the exterior surface of the shell. Vector  $\mathbf{x}_o = (x_o, y_o, z_o)$  denotes the coordinates of a number ( $N_o$ ) of observation points located on the interface between the soil and the tunnel.

### 4.2.3 Half-space domain

As is discussed before, the scattered field in the soil is represented as resulting from a number of sources acting in the half-space which are located slightly inside the region to be occupied by the shell. Within the soil medium, the scattered displacements are written in discretized matrix form

$$\mathbf{U}_1^{\text{sc}}(\mathbf{x}) = \int_{L_0} \mathbf{G}_1(\mathbf{x}, \mathbf{x}_s) \mathbf{F}(\mathbf{x}_s) dl(\mathbf{x}_s) \quad (4.6)$$

Similarly, for the traction related to the scattered field

$$\mathbf{T}_1^{\text{sc}}(\mathbf{x}) = - \int_{L_0} \mathbf{H}_1(\mathbf{x}, \mathbf{x}_s) \mathbf{F}(\mathbf{x}_s) dl(\mathbf{x}_s) \quad (4.7)$$

where  $\mathbf{G}_1$  and  $\mathbf{H}_1$  are matrices of 2.5D Green's functions for displacements and stresses of the half-space, respectively; and  $\mathbf{F}(\mathbf{x}_s)$  represents the unknown amplitudes of the sources whose position and the direction are known. The contour  $L_0$  corresponds to the source position. They are the same as the ones discussed in Chapter 2. Relation (4.6) and (4.7) hold equally for displacements and stresses at the interface between the soil and the tunnel.

### 4.2.4 Cylindrical shell domain

For the shell component, the displacements at the shell outside surface and the net stresses can be related through equation (2.38). For the hyperloop problem where there is gravity pressure acting at the shell inside, the net loading  $\mathbf{Q}_2(\theta')$  in (2.38) has to be modified.

$$\mathbf{Q}_2(\theta') = \mathbf{T}_2^{\text{out}}(\theta') - \mathbf{T}_2^{\text{in}}(\theta') \quad (4.8)$$

where

$$\mathbf{T}_2^{\text{in}}(\theta') = \mathbf{P}^{\text{hyper}}(\theta') \quad (4.9)$$

$\mathbf{T}_2^{\text{out}}(\theta')$  and  $\mathbf{T}_2^{\text{in}}(\theta')$  represent the loading on the outer surface and inner surface of the shell, respectively;  $\mathbf{P}^{\text{hyper}}$  represents the gravity pressure from a hyperloop pod acting on the inner surface of the shell.

### 4.2.5 Coupling equations of the shell and soil medium

Using equations (2.38), (4.2), (4.3), (4.5), (4.6), (4.7), (4.8), (4.9) the displacement fields  $\mathbf{U}_1(\mathbf{x}_o)$  from the half-space and  $\mathbf{U}_2^{\text{out}}(\mathbf{x}_o)$  from the shell at the soil-tunnel interface  $\mathbf{x}_o \in L_2$  can be written

$$\mathbf{U}_1(\mathbf{x}_o) = \int_{L_0} \mathbf{G}_1(\mathbf{x}_o, \mathbf{x}_s) \mathbf{F}(\mathbf{x}_s) dl(\mathbf{x}_s) \quad (4.10)$$

$$\mathbf{U}_2(\mathbf{x}_o) = \int_S \mathbf{G}_2(\mathbf{x}_o, \mathbf{x}') \cdot \left[ \int_{L_0} \mathbf{H}_1(\mathbf{x}_o, \mathbf{x}_s) \mathbf{F}(\mathbf{x}_s) dl(\mathbf{x}_s) - \mathbf{P}^{\text{hyper}}(\mathbf{x}_o) \right] dl(\mathbf{x}') \quad (4.11)$$

where  $\mathbf{x}_s \in L_0$  represents the position of the sources;  $\mathbf{x}_o \in L_2$  denotes the position of the observations;  $\mathbf{x}, \mathbf{x}' \in S$  denotes the shell. It can be seen that the vector  $\mathbf{F}(\mathbf{x}_s)$ , the



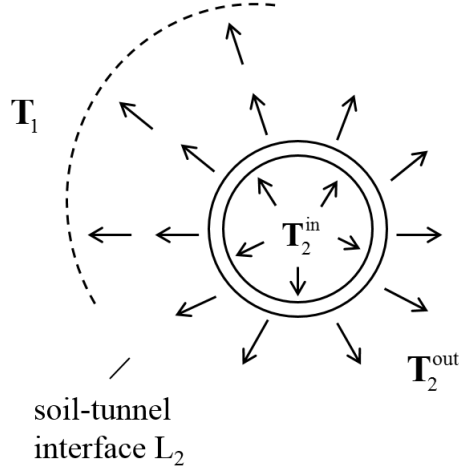


Figure 4.3: Traction equilibrium and net loading on the shell

unknown amplitude of the sources, appears in both equations, meaning that the thin shell and the half-space are coupled.

Next, in order to apply the displacement continuity condition, substituting equation (4.10) and (4.11) into (4.4) and rearranging terms leads to

$$\int_{L_0} \mathbf{B}(\mathbf{x}_o, \mathbf{x}_s) \mathbf{F}(\mathbf{x}_s) dl(\mathbf{x}_s) = \mathbf{D}(\mathbf{x}_o) \quad (4.12)$$

where

$$\mathbf{B}(\mathbf{x}_o, \mathbf{x}_s) = \mathbf{G}_1(\mathbf{x}_o, \mathbf{x}_s) - \int_S \mathbf{H}_1(\mathbf{x}_o, \mathbf{x}_s) \mathbf{G}_2(\mathbf{x}_o, \mathbf{x}'_o) dl(\mathbf{x}'_o) \quad (4.13)$$

and

$$\mathbf{D}(\mathbf{x}_o) = - \int_S \mathbf{P}^{\text{hyper}}(\mathbf{x}_o) \mathbf{G}_{22}(\mathbf{x}_o, \mathbf{x}'_o) dl(\mathbf{x}'_o) \quad (4.14)$$

Equation (4.12) is the equation to be solved for the unknown amplitudes of sources  $\mathbf{F}(\mathbf{x}_s)$ . To get to this equation, the continuity of displacements and equilibrium of stresses at the interface between the soil and tunnel have been employed. Note that in order to connect displacements and stresses on the shell with those of the soil, it is necessary to refer these vectors to the same cylindrical coordinates. The coordinates conversion relation has been given in chapter 2. Similarly as before, once the unknown amplitudes have been found, the displacement fields in the soil medium and in the shell can be calculated from equations (4.10) and (4.11).

## 4.3 Frequency domain and time domain response

### 4.3.1 Frequency domain

Since the calculation is carried out in the frequency domain, it is necessary to transform the loading in Eq.(4.1) into frequency domain. Applying a double Fourier transform with time  $t$  and space  $z$  to the non-zero term in equation (4.1),

$$\begin{aligned}
 p_r(k_z, \omega) &= \int_{-\infty}^{+\infty} \int_{-\infty}^{+\infty} \frac{2P_0}{\pi R_1} \left\{ H\left(\theta_1 - \frac{\pi}{4}\right) - H\left(\theta_1 - \frac{3\pi}{4}\right) \right\} \delta(z - Vt) e^{ik_z z - i\omega t} dz dt \\
 &= \int_{-\infty}^{+\infty} \frac{2P_0}{\pi R_1} \left\{ H\left(\theta_1 - \frac{\pi}{4}\right) - H\left(\theta_1 - \frac{3\pi}{4}\right) \right\} e^{ik_z Vt - i\omega t} dt \\
 &= \frac{2P_0}{\pi R_1} \left\{ H\left(\theta_1 - \frac{\pi}{4}\right) - H\left(\theta_1 - \frac{3\pi}{4}\right) \right\} 2\pi \delta(k_z V - \omega) \\
 &= \frac{2\pi}{V} \frac{2P_0}{\pi R_1} \left\{ H\left(\theta_1 - \frac{\pi}{4}\right) - H\left(\theta_1 - \frac{3\pi}{4}\right) \right\} \delta\left(k_z - \frac{\omega}{V}\right)
 \end{aligned} \tag{4.15}$$

in which the shifting property of Dirac-delta function and property  $\delta(x - a) = \frac{1}{2\pi} \int_{-\infty}^{+\infty} e^{ip(x-a)} dp$ ,  $\delta(cx) = \frac{1}{c} \delta(x)$  have been used. Then, applying an inverse Fourier transform with  $k_z$ ,

$$\begin{aligned}
 p_r(z, \omega) &= \int_{-\infty}^{+\infty} \frac{2\pi}{V} \frac{2P_0}{\pi R_1} \left\{ H\left(\theta_1 - \frac{\pi}{4}\right) - H\left(\theta_1 - \frac{3\pi}{4}\right) \right\} \delta\left(k_z - \frac{\omega}{V}\right) e^{-ik_z z} dk_z \\
 &= \frac{2\pi}{V} \frac{2P_0}{\pi R_1} \left\{ H\left(\theta_1 - \frac{\pi}{4}\right) - H\left(\theta_1 - \frac{3\pi}{4}\right) \right\} e^{-i\frac{\omega}{V}z}
 \end{aligned} \tag{4.16}$$

Considering a time-harmonic relation for equation (4.16), the moving load is shown to have the same form as the spatially varying line load for the case  $k_z = \omega/V$ . Mathematically, this relation provides the non-triviality of the Delta function in equation (4.15). Physically, this relation implies that the phase velocity of all waves radiated by the constant load must be equal to the velocity  $V$  of the load [21]. In this sense, these 2.5D Green's functions can be applied for constant moving load problems. Note that the factor  $\frac{2\pi}{V}$  should be used for a proper scaling. In other words, the 2.5D Green's functions are already the frequency responses of the half space due to a constant moving load, but with a scaling factor related to the velocity shown in Eq.(4.16).

With the proper form of loading, the coupling boundary integrals are solved to get the unknown amplitudes of the sources based on equation (4.12). Again, once the amplitudes of the unknown sources are known, at any point of the half-space, displacements related to scattered field can be computed using equation (2.4) and stresses related to scattered field can be computed using equation (2.6).

### 4.3.2 Time domain

The time domain response is obtained by applying a double inverse Fourier transform of the frequency-wavenumber response:

$$\mathbf{u}(x, y, z, t) = \frac{1}{4\pi^2} \int_{-\infty}^{+\infty} \int_{-\infty}^{+\infty} \mathbf{u}(x, y, k_z, \omega) e^{-i(\omega t - k_z z)} dk_z d\omega \quad (4.17)$$

In the frequency domain, displacement  $\mathbf{u}(x, y, z, t)$  is proportional to  $2\pi\delta(k_z V - \omega)$ . However, the kinetic invariant relation for a constant moving load entails  $k_z = \omega/V$ . The wave number  $k_z$  and the frequency  $\omega$  are not independent. Hence, the two dimensional inverse Fourier transform is reduced to one dimension with  $\omega$  only:

$$\mathbf{u}(x, y, z, t) = \frac{1}{4\pi^2} \int_{-\infty}^{+\infty} \mathbf{u}(x, y, \frac{\omega}{V}, \omega) e^{-i(\omega t - \frac{\omega}{V} z)} d\omega \quad (4.18)$$

Because the solution in the time domain should be real values, the imaginary part in 4.18 should be zero after integration from  $-\infty$  to  $+\infty$ . In the calculation, only the real part needs to be integrated, which is also even symmetric with  $\omega = 0$ .

$$\mathbf{u}(x, y, z, t) = \frac{2}{4\pi^2} \int_0^{+\infty} \text{Re} \left\{ \mathbf{u}(x, y, \frac{\omega}{V}, \omega) e^{-i(\omega t - \frac{\omega}{V} z)} \right\} d\omega \quad (4.19)$$

where the upper limit of frequency  $\omega$  should be truncated. In equation (4.19),  $z$  denotes the position of the interest. Since it is steady state solution, the response should be the same at every point in the  $z$  direction, and the difference is just a phase shift. Equation (4.19) can be further simplified if  $z = 0$ :

$$\mathbf{u}(x, y, 0, t) = \frac{2}{4\pi^2} \int_0^{+\infty} \text{Re} \left\{ \mathbf{u}(x, y, \frac{\omega}{V}, \omega) e^{-i\omega t} \right\} d\omega \quad (4.20)$$

Note here the upper limit of  $\omega$  should be truncated. The integration process is carried out using the trapezoidal integration. Time domain results shown in the next section are calculated based on Eq.(4.20), which involves calculating the response at each frequency and consider a sufficiently small frequency step size  $\Delta f$ . Also, the frequency component should be calculated up to a sufficiently large frequency such that all the energy is captured. Depending on the energy distribution in the spectra, these two criteria are met in the following calculations. Since the Fourier transform is periodic in its nature, the time domain response is also periodic. The periodic time domain response is in essence the steady-state response. However, the time window is restricted to one period  $[-\frac{T}{2}, \frac{T}{2}]$  with the time window defined as  $T = \frac{1}{\Delta f}$ . As is shown, a sufficiently small frequency time step size  $\Delta f$  is needed in order to get to a wide window. The time domain response in each period should be zero at both ends of the time window.

## 4.4 Convergence tests and validation

Numerical results for a moving constant load applied at the tunnel invert are presented in this section. The response is computed at the point A with coordinates  $(x = 0 \text{ m}, y = 0 \text{ m}, z = 0 \text{ m})$  and at the tunnel invert, as shown in Figure 4.1.

### 4.4.1 Convergence tests

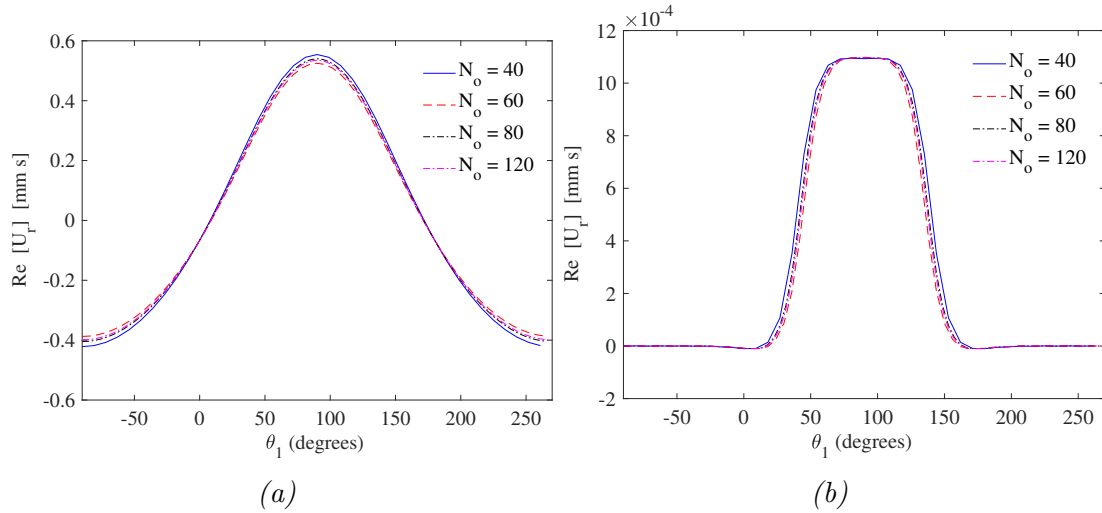


Figure 4.4: Convergence test of  $Re \{U_r\}$  at soil-tunnel interface for different number of receivers considering different frequencies and hyperloop speed: (a)  $f_0 = 0.2 \text{ Hz}$ ,  $V = 30 \text{ m/s}$ ; (b)  $f_0 = 20 \text{ Hz}$ ,  $V = 50 \text{ m/s}$

Figure 4.4 shows two examples of convergence test which show the real parts of radial displacements  $U_r$  versus angle for two scenarios. For convenience, angle equal to  $90^\circ$  in Fig.4.4 denotes the tunnel invert and the radial displacement is outwards positive. Because the moving load is evenly distributed on the lower part of the cavity with a range  $\theta_1 = [\frac{\pi}{4}, \frac{3\pi}{4}]$ , responses are symmetric with respect to  $\theta_1 = 90^\circ$ . In Fig.4.4(a), for a low frequency component a low speed  $V = 30 \text{ m/s}$ , the first two in-plane flexural modes are dominating. In both scenarios, the radial displacements are converged when the observation points are equal or more than 40. Therefore, 40 points of observations (and 20 points of sources) are sufficient enough for converged results. A couple of convergence tests for other frequencies and other speeds are shown in appendix A.

Figure 4.5 shows the convergence of vertical velocity at point A on the surface. It is found that the response at the surface is more difficult to converge than the one at the cavity surface, especially in high speed cases. In other words, to have converged results on the surface at high frequencies for a hyperloop speed higher than  $150 \text{ m/s}$ , at least 80 observations and 40 sources should be used. For even higher hyperloop speeds, the number should be increased correspondingly. Unless specified, the same number of

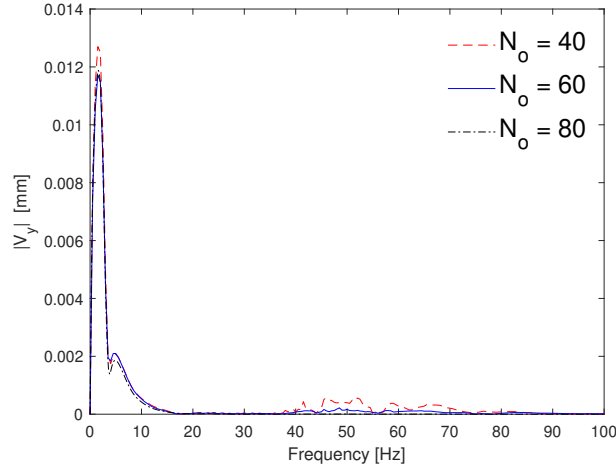


Figure 4.5: Convergence test for amplitude of vertical velocity at point A for different number of receivers considering frequency up to 100 Hz ( $V = 150$  m/s)

sources and receivers are used in the calculations that follow.

#### 4.4.2 Check of interface conditions

As a second step, the interface conditions are checked in order to ensure the compatibility of displacements. Since the traction continuity has been applied as a pre-condition, it is automatically satisfied. Figure 4.6 shows the displacement at the tunnel-soil interface. Displacements are calculated from the soil side using the equation (4.10) and from the tunnel side using the equation 4.11. As can be seen, they are equal to each other with the difference in the magnitude of  $10^{-12}$ . The same scenarios are observed for radial displacement  $U_\theta$  and longitudinal displacement  $U_z$ . We conclude that the interface conditions are satisfied well.

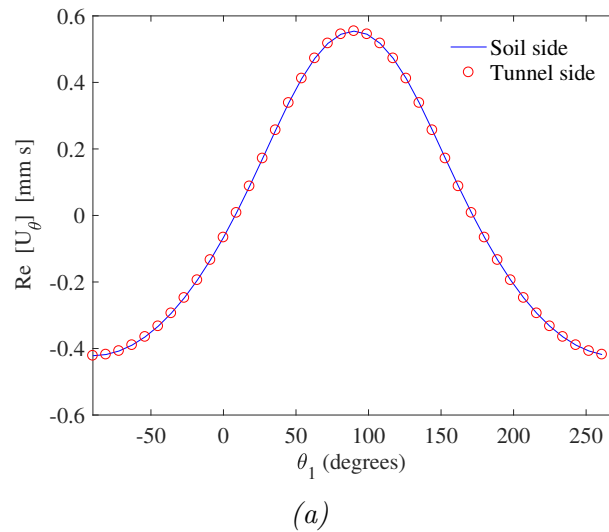


Figure 4.6:  $\text{Re}\{U_r\}$  at the soil-tunnel interface from the soil side and from the tunnel side for  $f_0 = 0.2$  Hz,  $c = 30$  m/s

### 4.4.3 Validation

#### 4.4.3.1 Loading condition

In order to validate the proposed method, results calculated by the present model are compared with those obtained by Yuan et al [22]. In Yuan's model, a concrete tunnel is embedded in a half-space with both material modeled as a linear elastic continuum. The boundary conditions applied in the model are the same as those discussed earlier: stress-free boundary conditions on the free surface, radiation conditions at the infinity, displacement and stress compatibility at the soil-tunnel interface. The results from Yuan's work are scaled for the sake of comparison.

Note that in Yuan's work, a moving load is modeled as a point load acting at the tunnel invert. Only one point at the invert is loaded, both in the cross-section plane and in the longitudinal direction. In the current BEM model, in order to represent a point load at  $\theta_1 = \frac{\pi}{2}$ , the following form of the load is adopted:

$$p_r(\theta_1, z, t) = \frac{P_0}{1 \times R_1} \delta(\theta_1 - \frac{\pi}{2}) \delta(z - Vt) = \frac{P_0}{1 \times R_1} \delta(z - Vt) \frac{1}{2\pi} \sum_{n=-N}^N e^{in(\theta_1 - \frac{\pi}{2})} \quad (4.21a)$$

$$p_\theta(\theta_1, z, t) = 0 \quad (4.21b)$$

$$p_z(\theta_1, z, t) = 0 \quad (4.21c)$$

meaning that the moving load is a point load acting at the tunnel invert in the 2D plane  $xOy$  plane and in the longitudinal direction. By applying this load in the BEM model, the following validation is conducted by comparing results obtained by the current method and those from Yuan *et al.*

#### 4.4.3.2 Numerical results

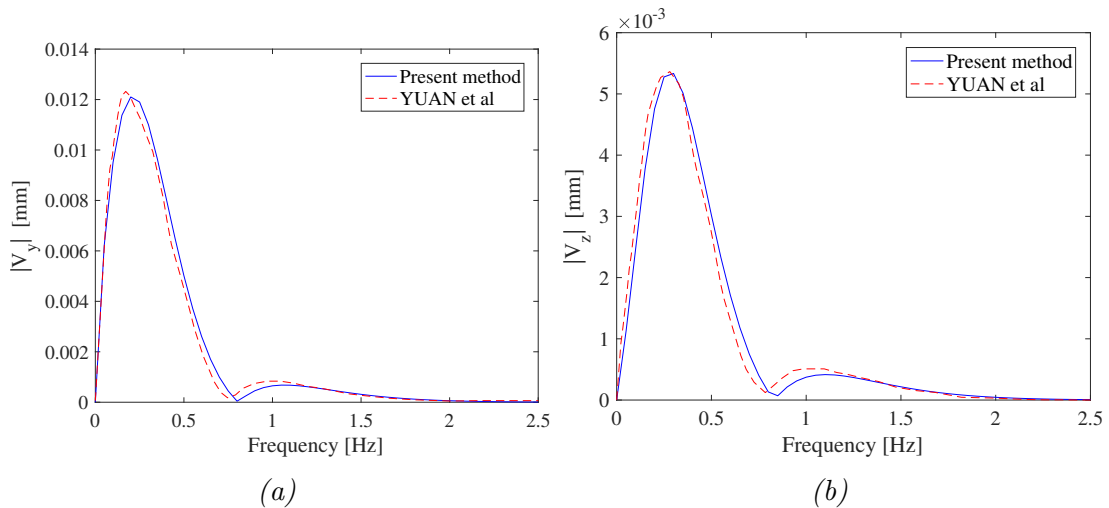


Figure 4.7: Amplitude spectrum comparison of the velocity response at point A due to a moving constant load ( $V = 30$  m/s)

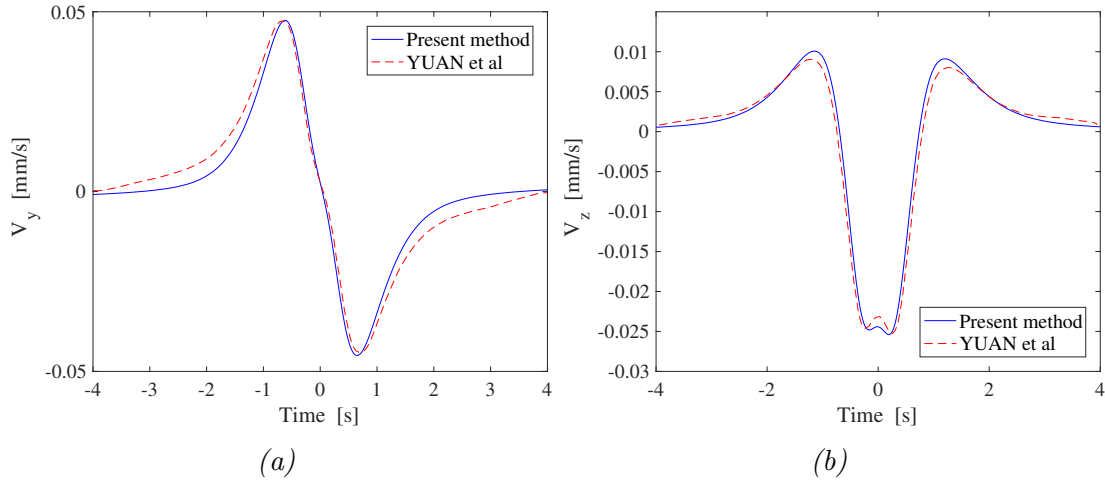


Figure 4.8: Time domain comparison of velocity response at point A on the half-space surface due to a moving constant load ( $V = 30$  m/s)

Figure 4.7 shows the frequency spectrum comparison for the velocity response in vertical and longitudinal directions at point A for  $V = 30$  m/s. The magnitudes at frequency  $f = 0$  Hz are set to be zero for a static case. Two peaks can be clearly observed from both spectra: the dominating part is at frequency  $f = 0.2$  Hz and a secondary part at frequency  $f = 1$  Hz.

Figure 4.8 shows the velocity time domain response comparison corresponding to the spectra in figure 4.7. This is done by applying inverse Fourier transform with respect to frequency. Time domain response in figure 4.8 are periodic and are confined to the time window  $[-4$  s,  $4$  s] for the sake of comparison. The time instant  $t = 0$  corresponds to the moment when the moving load exactly passes the observation point. The peak amplitude at frequency  $f = 0.2$  Hz observed in figure 4.7 indicates 1 cycle per 5 seconds, which is the main oscillating part in the time domain plot. Although the spectra for  $v_y$  and  $v_z$  are very similar, the time domain responses are very different. This is because the phase is not showed in the amplitude spectrum. In figure 4.8,  $v_y = 0$  at  $t = 0$  physically means the corresponding displacement reaches its maximum value.

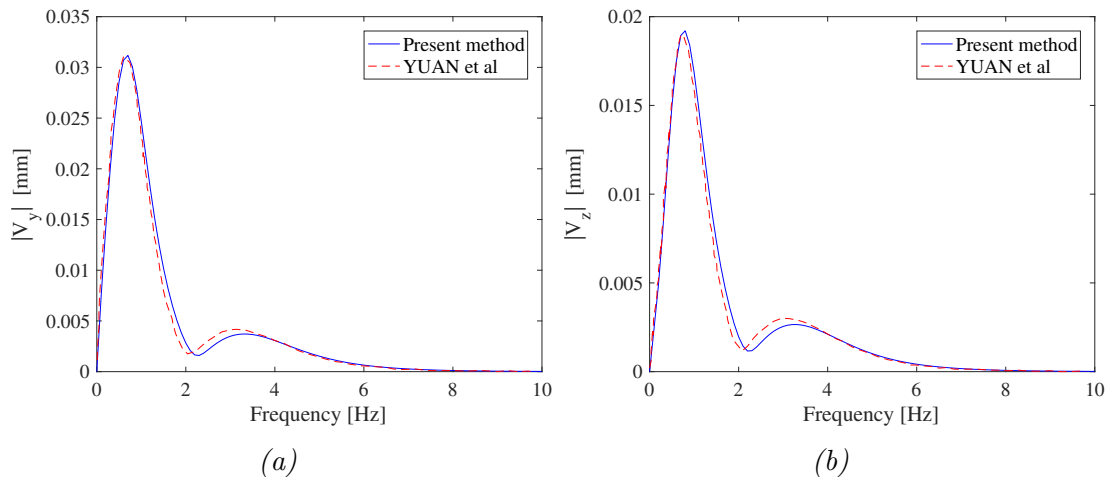


Figure 4.9: Frequency spectrum comparison for velocity response at point A due to a moving constant load ( $V = 75$  m/s)

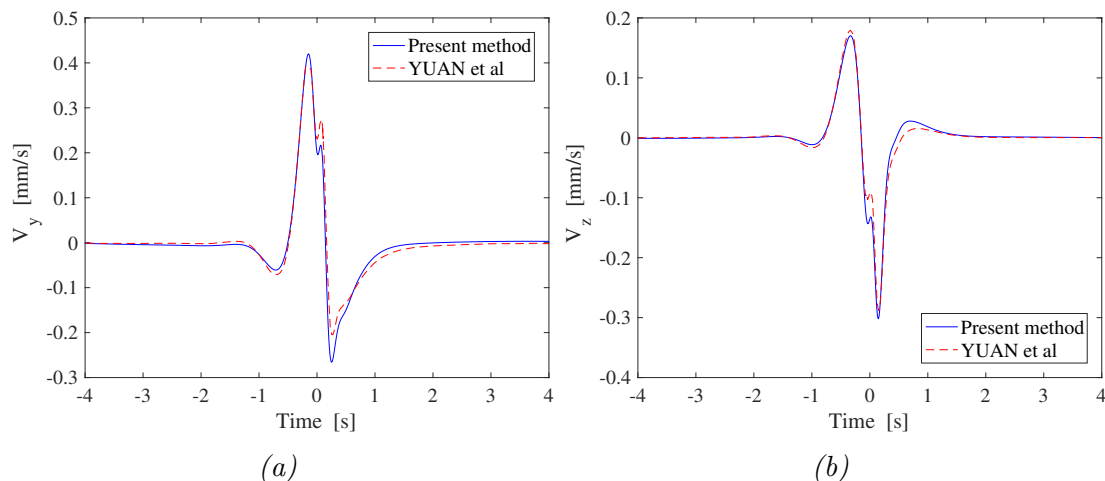


Figure 4.10: Time domain comparison of velocity response at point A on the half-space surface due to a moving constant load ( $V = 75$  m/s)

Similarly, for  $V = 75$  m/s, figure 4.9 and figure 4.10 show the amplitude spectrum comparison and the corresponding time domain comparison of velocity response at point A on the free-surface, respectively. Comparing to figure 4.7 for a subcritical case, the spectrum ranges are widened from 0 – 2Hz to 0 – 10Hz in figure 4.9. Two peaks are still observed but with larger amplitudes compared to those in figure 4.7. The smaller peak becomes more noticeable. In figure 4.10, wave patterns for the case  $V = 75$  m/s are more complicated than those for the case  $V = 30$  m/s. Time duration of the pulse becomes shorter and the change in velocity direction becomes more frequent which is probably due to strong wave radiation. A very important phenomenon observed is the maximum velocities for  $V = 75$  m/s is almost 10 times of those for  $V = 30$  m/s.

As can be seen, results obtained using the present method are proven to be in good agreement with those obtained by Yuan *et al* [22].



#### 4.4.4 Parametric study

In this section, the effect of varying parameters on the response of the system are investigated. Here, 3 main parameters are investigated: the hyperloop speed, the tunnel depth and the tunnel lining thickness. The standard parameters are those shown in 4.1.

##### 4.4.4.1 Effect of hyperloop speed

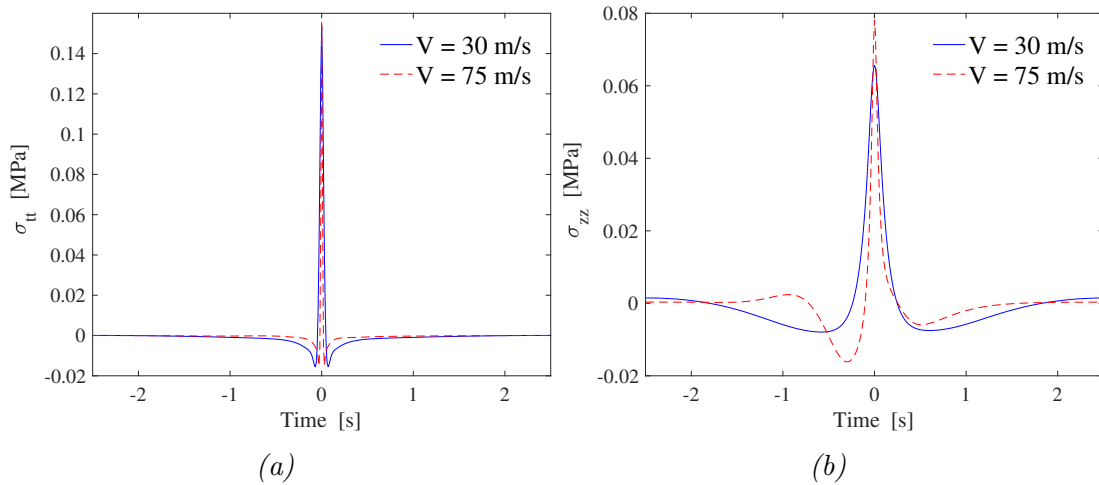


Figure 4.11: Stresses at tunnel invert for subcritical case  $V = 30$  m/s and critical case  $V = 75$  m/s: (a) hoop stress; (b) longitudinal stress

Fig.4.11 shows the hoop stress and longitudinal stress at the tunnel invert for  $V = 30$  m/s and  $V = 75$  m/s. For the hoop stress, the amplitudes are larger while the time duration are 10 times shorter than those of longitudinal stress. The case  $V = 75$  m/s has more influence on the time duration than on the amplitude, compared to the case  $V = 30$  m/s. At the tunnel invert, concrete experiences a tension at the moment when the hyperloop passes by, both in the radial direction and longitudinal direction. For the longitudinal stress, the response is less abrupt which lasts for approximately 4 seconds. Before or after the hyperloop passes the observation point, a compressive stress occurs due to the bending effect of the shell. The case  $V = 75$  m/s can cause an increase in the longitudinal stress amplitude, compared to the case  $V = 30$  m/s.

Fig.4.12 shows the effect of hyperloop speed on the displacement response at the tunnel invert. The singularity at frequency  $f = 0$  Hz in the Green's functions results in infinite values of displacement which are clearly observed. It may not be accurate by comparing the maximum values in the displacement spectrum because it is related to the frequency step size  $\Delta f$ . Furthermore, missing the zero-frequency component can result in an inaccuracy, which can introduce a wrong offset in the time domain response at the end points of the time window. In order to obtain a feasible time domain displacement response, the zero-frequency component is estimated by a linear extrapolation based on the first two points in the frequency spectrum, which might introduce an inaccuracy.

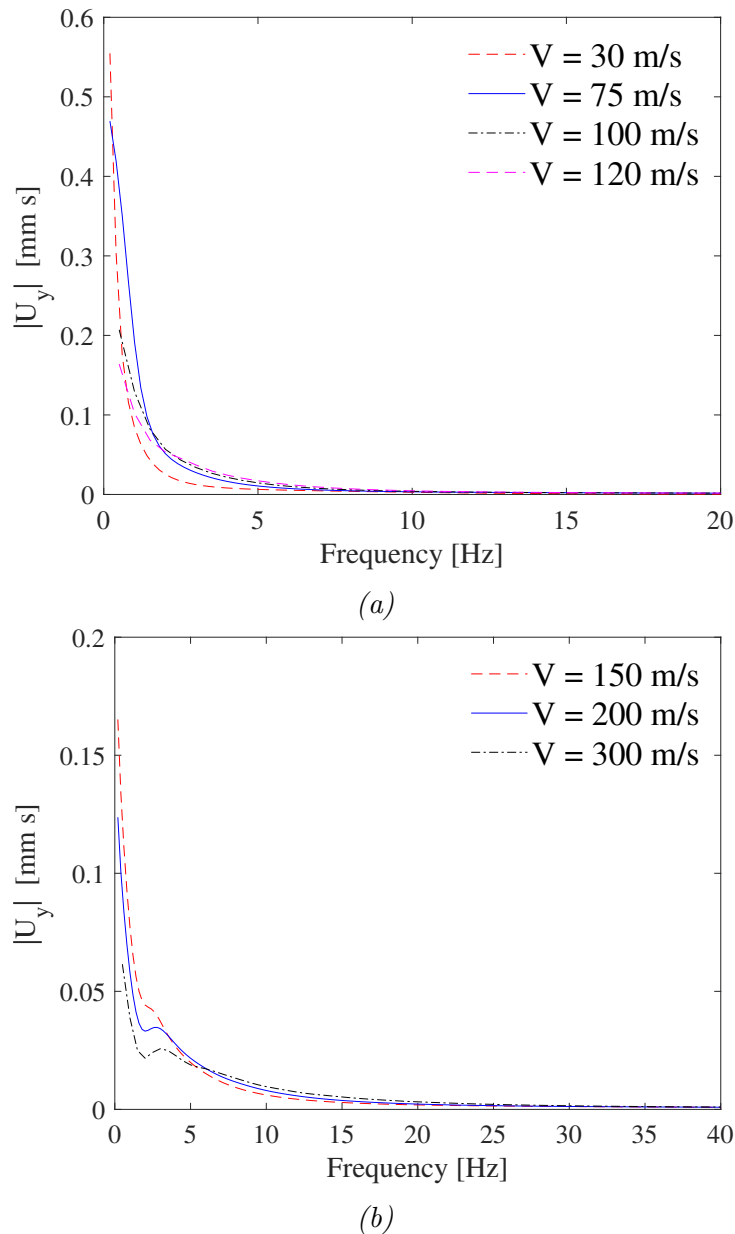
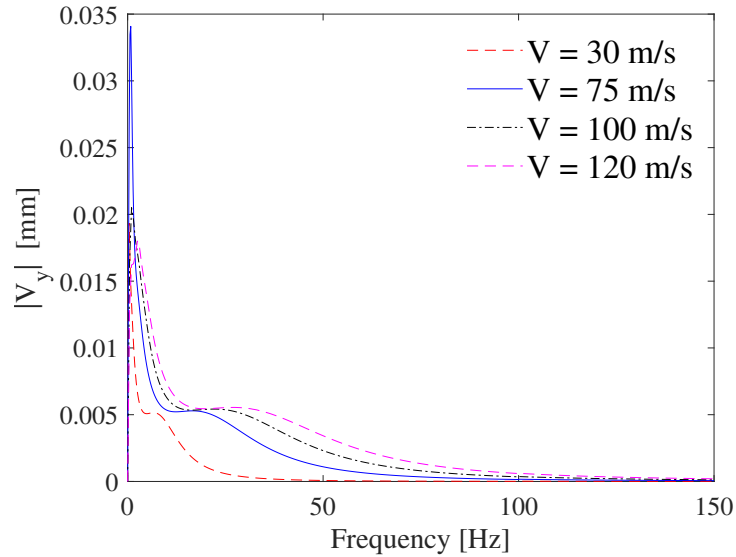


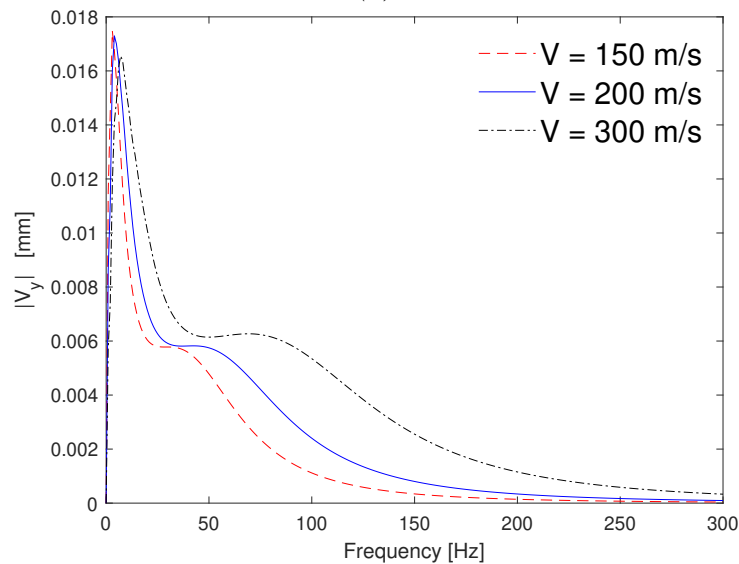
Figure 4.12: Amplitude spectrum of the vertical displacement response at tunnel invert for different hyperloop speeds

From fig.4.12(a) for cases  $V < 150$  m/s, the spectra of vertical displacements at the tunnel invert are confined to a low frequency band 0 - 10 Hz and the main energy is located at frequency lower than 5 Hz. Varying the hyperloop speed does not make too much differences in the displacement spectra. However, in fig.4.12(b) for cases  $V > 150$  m/s, the spectra become wider and more importantly, a second peak located at  $f = 3$  Hz starts to develop with a further increase in the hyperloop speed. The second peak appeared in the spectra could be attributed to the reflected waves from the free surface. For all cases, the main energy is located at  $f = 0$  Hz due to the gravity load from the hyperloop.

Fig.4.13 shows the effect of hyperloop speed on the velocity response at the tunnel invert. Since we are looking for steady-state responses which are assumed to be harmonic and proportional with the  $e^{i\omega t}$ , and the velocity is the first derivative of displacement with



(a)



(b)

Figure 4.13: Amplitude spectrum of the vertical velocity response at tunnel invert for different hyperloop speeds

respect to  $t$ , the velocity spectrum is obtained by multiplying a factor  $i\omega$  to the displacement spectrum at each frequency in Fig. 4.12. The velocity spectrum is related to how fast the displacement spectrum decays with frequency increases. When the amplitude is negligibly small at a sufficient high frequency, the convergence of the spectrum is satisfied.

In figure 4.13(a) for  $V < 150$  m/s, a noticeable part of the energy can be observed up to frequency  $f = 100$  Hz. The maximum peak observed in the velocity spectrum for  $V = 75$  m/s suggests the resonance of the system. With the increase in the hyperloop speed, the velocity spectrum becomes wider even though the speed is higher than the resonance speed  $V = 75$  m/s. In figure 4.13(b) for  $V > 150$  m/s, the frequency spectra are approximately two times wider than those for  $V < 150$  m/s, which suggests the difficulty of the convergence of the velocity spectrum. The truncated frequency of the

amplitude spectra should be sufficiently high in order to get to converged time domain responses.

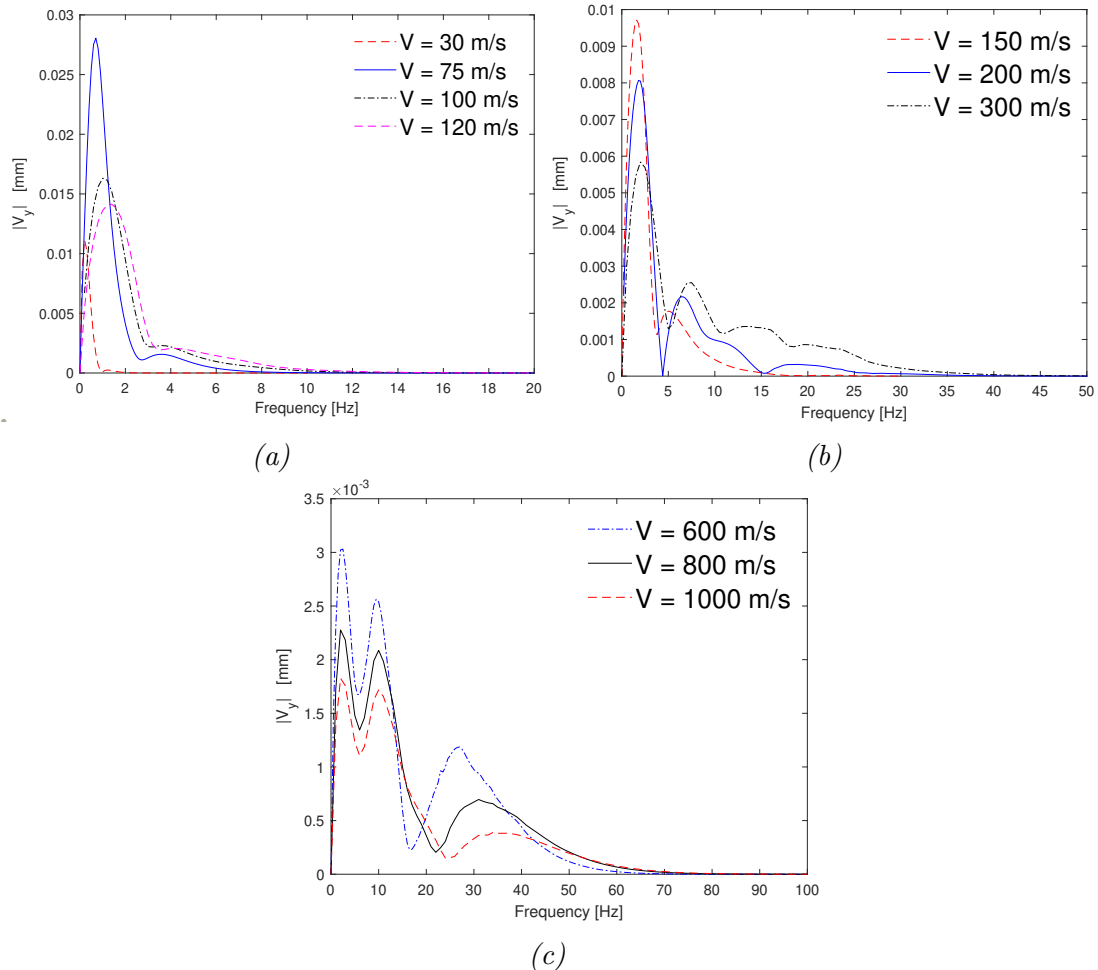


Figure 4.14: Amplitude spectrum of the vertical velocity responses at the surface point A for different hyperloop speeds

Fig.4.14 shows the effect of hyperloop speed on the velocity response at point A on the free surface. At the surface, reflected waves are generated and the stress-free boundary condition is satisfied. Intense interference of P waves and S waves results in Rayleigh waves whose amplitude decreases exponentially with the depth. From fig.4.14, the main energy is confined to a frequency band lower than 50 m/s, which is more narrow than the velocity spectrum at the tunnel invert shown in 4.13. Similarly, for cases  $V < 150$  m/s, two peaks are observed in the spectra. The maximum peak for  $V = 75$  m/s located at  $f = 1$  Hz suggests the resonance of the soil. For cases  $V > 150$  m/s, a further increase of hyperloop speed results in more peaks in the spectrum. For cases  $V > 600$  m/s, three peaks are shown in the spectrum.

## 4.4.4.2 Effect of tunnel depth

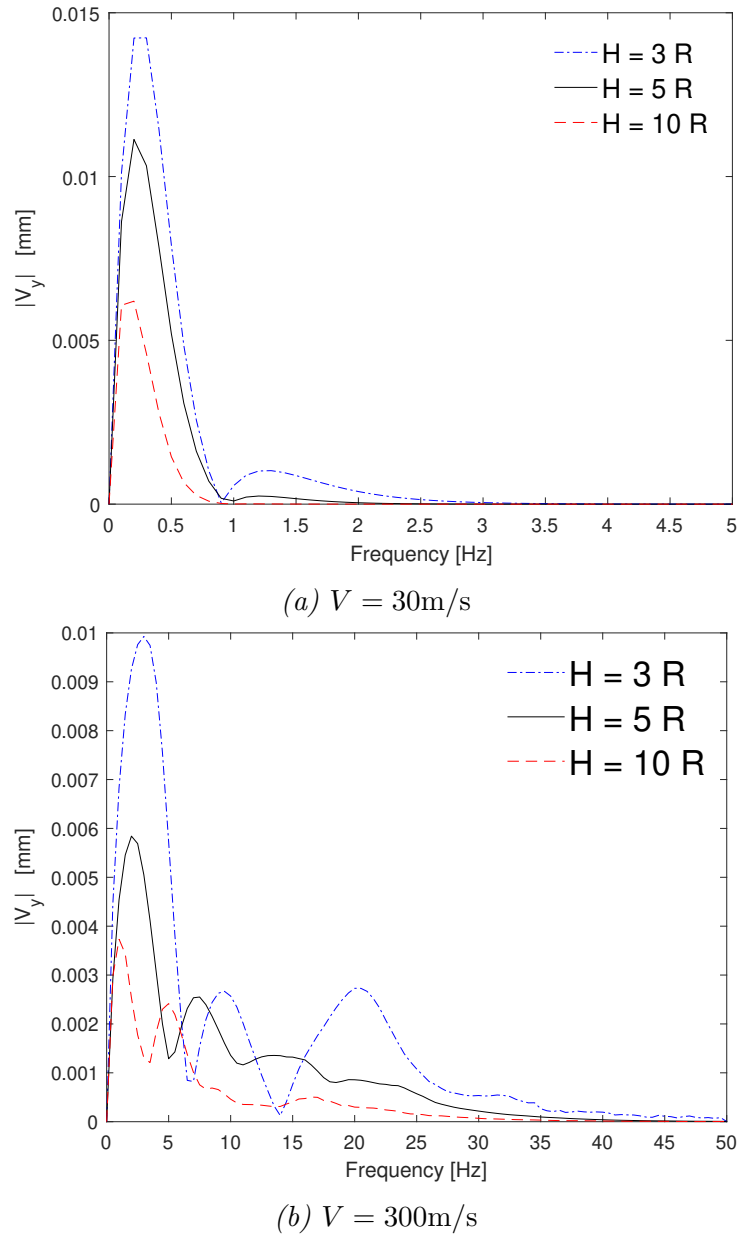


Figure 4.15: Amplitude spectrum of the vertical velocity response at the free surface point A

Fig.4.15 shows the effect of tunnel depth on the velocity response at the surface point A. It is observed that the peaks are smaller and the values decrease with the increase in the tunnel depth. In fig.4.15(a) for ( $V = 30\text{m/s}$ ), the smaller peaks in the spectra for  $H = 3R_2$  and  $H = 5R_2$  cannot be observed any more in the spectrum for  $H = 10R_2$ . Because for a deep tunnel  $H = 10R_2$ , the free surface is considered to have trivial influence on the tunnel and vice versa. The secondary waves reflected from the free surface are damped out on the path to the tunnel. Therefore, we conclude that the smaller peak which occurs at 1.2 Hz is due to the interaction between the free surface and the tunnel structure, while the larger peak which occurs at 0.2 Hz is due to the first-arrived waves

from the tunnel. In fig.4.15(a) for ( $V = 300\text{m/s}$ ), waves with higher frequency content are generated due to high speeds of the hyperloop, which can be seen from the truncated frequency. Also, the peaks becomes more prominent for a shallow tunnel case  $H = 3R_2$ , with larger amplitudes and more clear outlines.

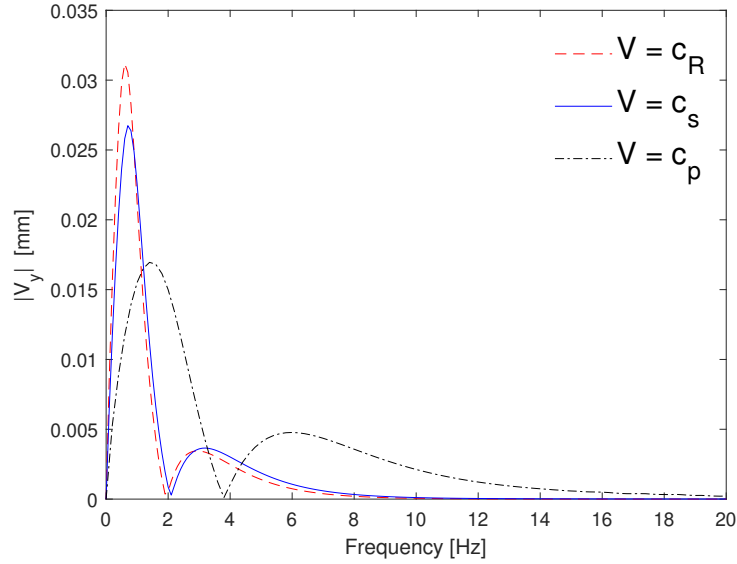


Figure 4.16: Amplitude spectrum of the velocity response at the ground surface point A in the case of a shallow tunnel  $H = 1.5 R_2$  for  $V = c_R, c_s$  and  $c_p$

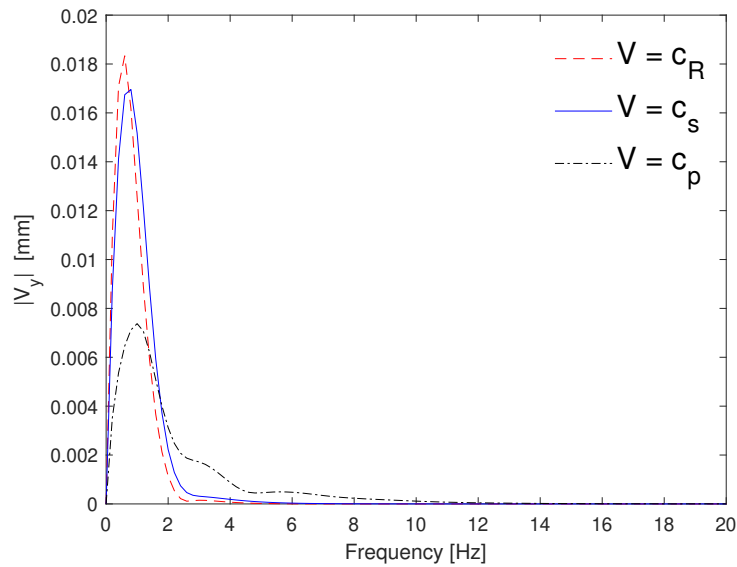


Figure 4.17: Amplitude spectrum of the velocity response at the ground surface point A in the case of a deep tunnel  $H = 10 R_2$  for  $V = c_R, c_s$  and  $c_p$

Figure 4.16 and figure 4.17 show the amplitude spectra of the velocity response at point A in the critical cases ( $V = c_R, c_s$  and  $c_p$ ) for a shallow tunnel case ( $H = 1.5R_2$ ) and for a deep tunnel case ( $H = 10R_2$ ). For both cases, the main energy is located at frequency lower than 2 Hz when  $V = c_R$  and  $V = c_s$ . For  $V = c_p$ , the influence on the

shallow tunnel case is more prominent than on the deep tunnel case, with a wider range and a larger amplitude.

From figure 4.15(a), we have found out the first peak occurs due to the first-arrived waves from the tunnel, and the second peak occurs due to secondary waves reflected from the tunnel. In figure 4.16, the first peak corresponds to frequency  $f = 1$  Hz for  $V = c_R$  and  $V = c_s$ , and to 2 Hz for  $V = c_p$ . It is interesting to notice that the P-wave speed is approximately 2 times the S-wave speed. In other words, P waves travel back and forth between the free surface and the tunnel 2 times per second, while S waves travel 1 time per second. A similar phenomenon can also be observed for the second peaks: the frequency with main energy for  $V = c_p$  (6 Hz) is approximately 2 times the one for  $V = c_s$  (3 Hz).

In figure 4.17, only one peak can be observed for the 3 critical cases. Compared to the shallow tunnel case, the difference between the peak values for  $V = c_R$  and the peak for  $V = c_s$  is smaller. It suggests in a deep tunnel case, Rayleigh waves are not as dominant as in the shallow tunnel case, which is probably because the amplitudes of Rayleigh waves decay exponentially with depth.

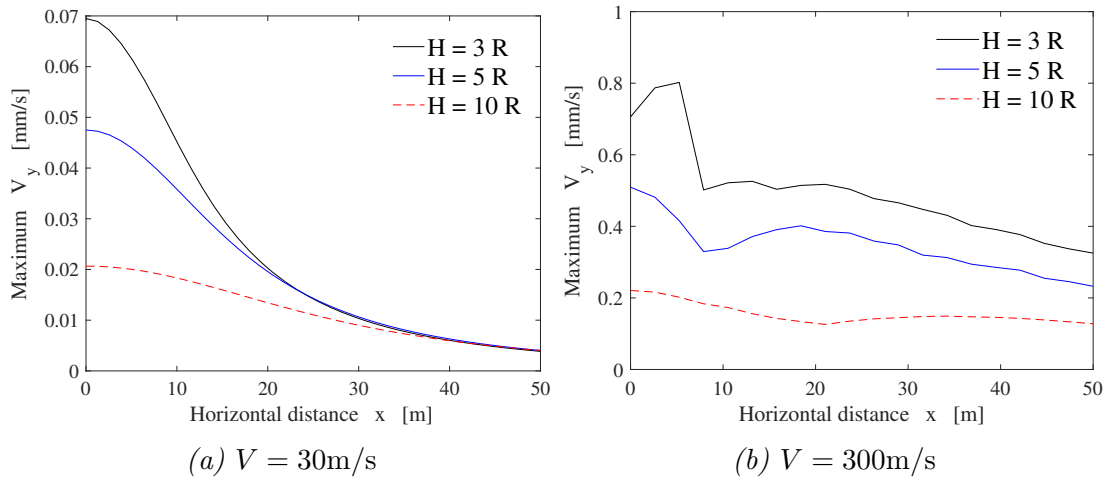


Figure 4.18: Maximum velocity response at the ground surface with varying tunnel depths

Fig.4.18 shows the effect of tunnel depth on the wave attenuation at the free surface from the point A on top of the tunnel to 50 meters away from it, for  $V = 30$  m/s and  $V = 300$  m/s. The maximum vertical velocity is obtained by looking at the velocity time domain response for each point at the surface, and then recording the maximum value. It can be seen that in general an increase of the tunnel depth leads to a decrease of the response at the ground surface, regardless of the hyperloop speed.

For  $V = 30$  m/s, the reduction effect is prominent at the locations near the tunnel but it cannot be observed any more at a larger distance  $y > 40$  m. Because for a hyperloop running at low speeds, the response is quasi-static whose influence is only in the near field. When the distance between the observation point and the tunnel is sufficiently

large, the reduction is not observed any more because the response is in itself trivial at a larger distance  $y > 40\text{m}$ .

For  $V = 300\text{m/s}$ , the reduction effect is equally noticeable both in the near field and in the far field. Because a hyperloop running at high speeds introduce high frequency waves, which are able to travel for a larger distance distance compared to low frequency waves. In the meantime, these high frequency waves are sensitive to the damping, therefore, in case of a deep tunnel, these high frequency waves are damped, causing a significant reduction in the vibration level at the ground surface.

#### 4.4.4.3 Effect of lining thickness

The variation of the tunnel thickness  $t$  is achieved by changing the outer radius  $R_2$  with the same inner radius  $R_1 = 2.75\text{m}$ . Three different values of wall thickness are selected,  $t = 150\text{mm}$ ,  $t = 250\text{mm}$  and  $t = 500\text{mm}$ . The wall thickness should not be chosen to be too large otherwise the thin shell theory is not applicable any more.

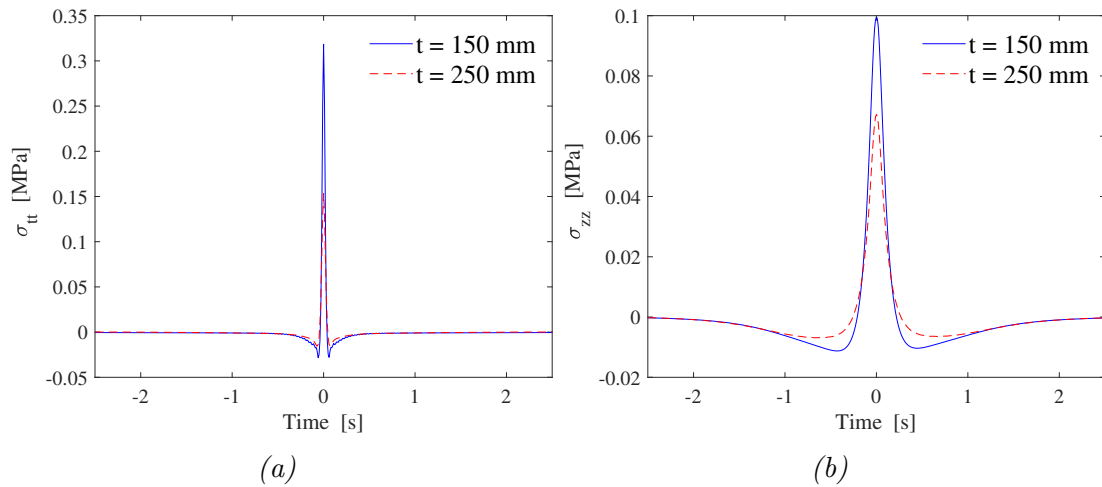


Figure 4.19: Stresses at tunnel invert for different tunnel wall thickness ( $V = 30\text{m/s}$ ): (a) hoop stress; (b) longitudinal stress

Fig.4.19 shows the effect of the lining thickness on the stresses of interest. In general, from a structural point of view, a reduction of the tunnel thickness leads to an increase in the stresses. The increase in the maximum stress level is even almost in direct proportion to the reduction in the wall thickness, since the total force to take remains the same. On the other hand, the duration of the response does not change with different wall thickness. Furthermore, compared to Fig.4.11, the threat of having a thin tunnel wall is more prominent than the case when the hyperloop is running at the Rayleigh wave speed.



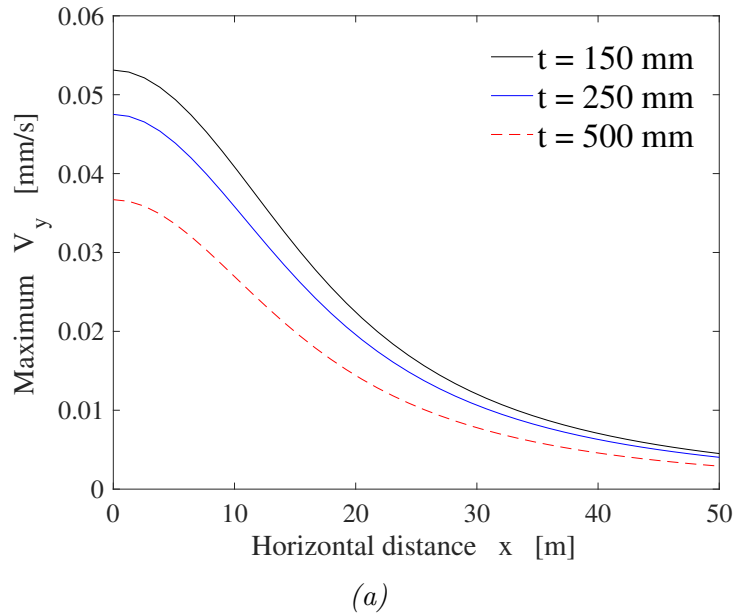


Figure 4.20: Maximum velocity response at the ground surface with varying lining thickness ( $V = 30\text{m/s}$ )

In Fig.4.20, similarly, the effect of tunnel wall thickness on the wave attenuation at the free surface is also shown. A similar reduction effect as the one in Fig.4.18 is observed when varying the lining thickness. In the near field, the variation of the lining thickness has a less influence on the ground surface response than the variation of the tunnel depth. Moreover, it is found that using a thick tunnel wall ( $t = 500\text{mm}$ ) can even reduce the ground vibration at a large distance ( $x = 50\text{m}$ ). This is because the increase of wall thickness increase the tunnel stiffness, the response of the tunnel due to a hyperloop running inside is suppressed.

#### 4.4.5 Full-space approximation

In this part, the half-space is approximately as a full-space. The full-space approximation means the Green's functions for a full-space are used in the procedure of solving the unknown amplitude of the sources, instead of using the Green's functions for a half-space. In this section, only the Green's functions in Eq.(2.15) are employed, while the surface terms such as those in Eq.(2.19) are neglected. The responses using the full-space Green's functions should be equal to those using half-space Green's functions under the condition that the tunnel depth is sufficiently large enough. Because the free-surface is so far away from the tunnel that the free-surface barely has an influence on the response of the tunnel. A great advantage of using the full-space Green's functions is a dramatic reduction in calculation time.

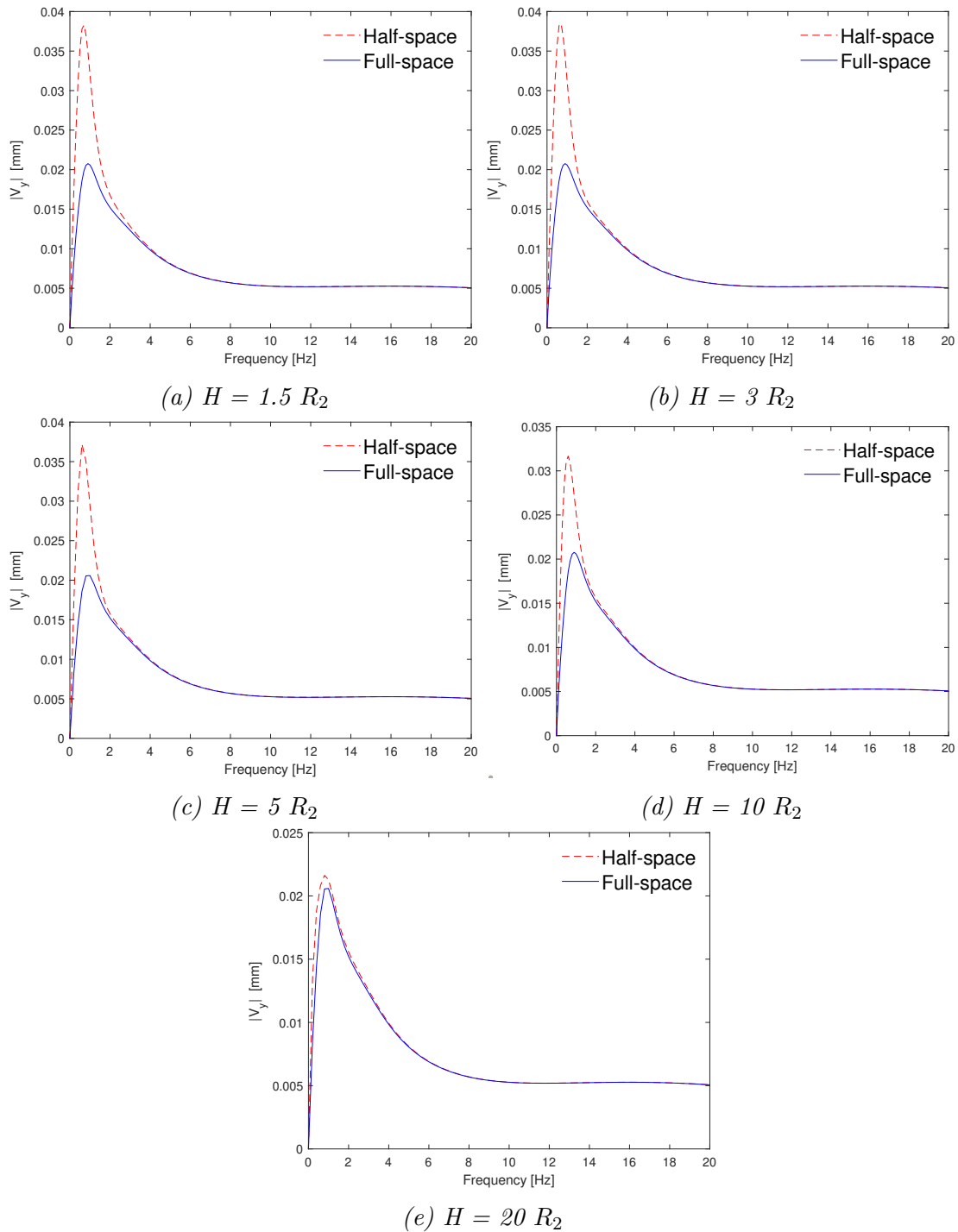


Figure 4.21: Amplitude spectra of vertical velocity at tunnel invert for different tunnel depths ( $V = 72$  m/s)

Figure 4.21 shows the velocity response at the tunnel invert for different tunnel depths ( $V = 72$  m/s). The frequency band is truncated at 20 Hz only for the purpose of having a clear comparison. In order to obtain an accurate time domain response, the frequency should be calculated up to a high frequency where energy is negligible. As can be seen, the responses by using the full-space Green's functions are the same regardless of different tunnel depths. This is logical because the full-space Green's functions are used, and the response should not depend on the burial depth. Secondly, in figure 4.21(e) it is seen that

with a sufficiently large depth ( $H = 20 R_2$ ), the response by using the half-space Green's functions and the one by using the full-space Green's functions are almost the same. The accordance in the response suggests that if the main interest is on a deep tunnel response, one can just apply the full-space Green's functions. By using the full-space Green's functions, the calculation time will take only one-tenth of the one by using the half-space Green's functions. Because when computing the half-space Green's functions, the numerical evaluation of the integrands related to the surface terms consumes a large amount of time.

## 4.5 Summary

In this chapter, the BEM model is employed for the hyperloop problem. A linear elastic homogeneous half-space having the material of soft soils due to a hyperloop running in the embedded tunnel is analysed. The hyperloop pod is considered to have a constant amplitude and a constant velocity. At the lower part of tunnel inside, the gravity force from the hyperloop acting in the radial direction is smeared in the circumferential direction.

As a first step, the convergence tests have shown that the convergence of the velocity response in the tunnel is not as good as that at the half-space surface in cases of high velocities and high frequencies. In most cases, 20 sources and 40 observations are sufficient for calculating the response at the cavity, while at least 40 sources and 80 observations are needed for calculating the responses at the half-space surface.

For the validation of the model, the same material parameters are chosen such that the results are comparable to those from literature. A point load is applied at the tunnel invert instead of pressure for the sake of comparison. Velocity responses at the half-space surface due to a hyperloop running at 30m/s and 75m/s are calculated using the current method, and have good agreements with those from literature.

As a further step, a parametric study has been carried out to study the effect of hyperloop speed, the effect of tunnel depth and the effect of lining thickness on the dynamic response of the system. The standard material parameters are those used in the literature. The hyperloop speed has the most prominent effect. The Rayleigh wave speed in the soil is found to be the critical speed where the maximum response of velocity in the soil is observed. At the half-space surface, the energy in the amplitude spectra of velocity response is confined to low frequency less than 10 Hz even if the hyperloop speed is close to the Rayleigh wave speed of the soil. Localized quasi-static deformation is observed for subcritical cases. Time domain plots of velocity responses have shown an amplification factor of 10 when the hyperloop is running at the Rayleigh wave speed of the soil, compared to subcritical cases. At the tunnel invert, the amplitude spectra have more high frequency content as the speed of the hyperloop increases. The hoop stress and the longitudinal stress at the tunnel invert shoots up 20 % more when the hyperloop is running at the Rayleigh wave speed of the soil compared to subcritical cases. Moreover, the parametric study reveals that the vibration in the system can be effectively reduced by constructing a tunnel with thicker wall and at a larger depth. The depth of the tunnel determines the wave interference between the free surface and the tunnel. Also, a sufficiently large depth ( $H = 20R_2$ ) renders using the full-space approximation feasible, which guarantees the same accuracy and in the meantime saves much computational time.

# Chapter 5

## Dynamic response of an embedded tunnel in a half-space subjected to a Hyperloop pod running in the tunnel by FEM

### 5.1 Finite element model

#### 5.1.1 Model description

The original version of the finite element model had been created by the engineering company Movares [7]. The model is adapted for the calculation of the new problem. The underground tunnel system is modelled as a tunnel embedded in a half-space as shown in figure 5.1.

The finite element model calculates the wave propagation from the tunnel through the soil layers. The area of interest is the part shown in figure 5.1b, where a tunnel is buried in surrounding soil. While the remaining 'U' shape-like parts (marked in different colors) represent the boundary condition at infinity. The edge elements are created to damp out waves radiated away from the tunnel. These boundary conditions allow the energy to disappear from the model without reflections, so that the model behaves like an semi-infinite half-space. For the calculation of the FEM model, a large number of edge elements have to be used to simulate the infinite boundary conditions of the half-space. These elements are not of interest but are necessary for the calculation and consume computational time.

The model was firstly created on a 2D plane and then protruded into a 3D volumn along the longitudinal direction. Note that the model is space-invariant in the longitudinal direction, which means the soil and the tunnel properties remain the same along the tunnel axis. The invariant space provides a prerequisite for the following method to model the hyperloop: the use of an stationary impulse load and a convolution rule. The adopted coordinate system is the same as the one used in chapter 4.

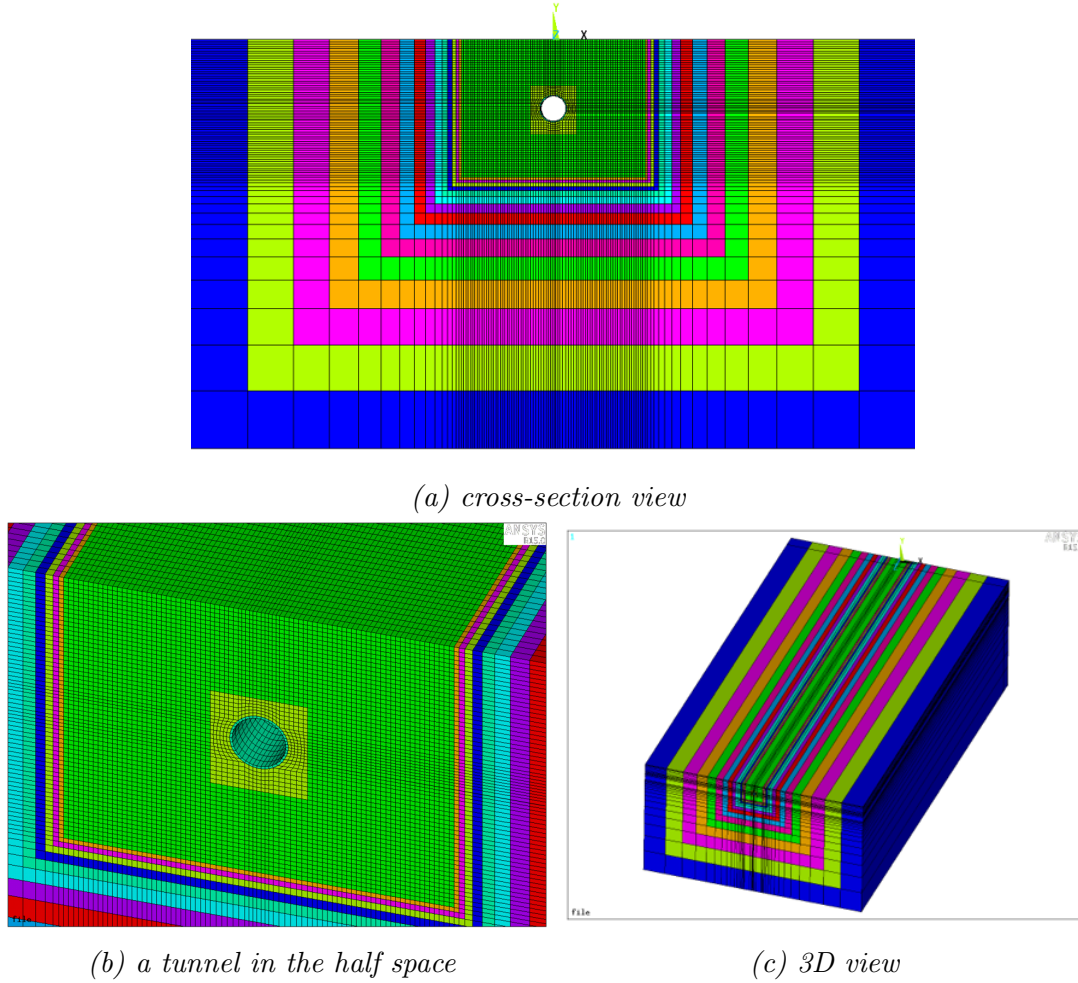


Figure 5.1: Finite element model

## 5.1.2 Model parameters

### 5.1.2.1 Material damping

The material damping applied in the finite element model is the Rayleigh damping which entails an inverse proportional relation with mass damping  $\alpha$  and a linear proportional relation with stiffness damping  $\beta$ . The values of  $\alpha$  and  $\beta$  are determined by the specified damping in each material at the defined lowest and highest frequency. The combined Rayleigh damping  $\zeta$  is

$$\zeta = \frac{\alpha}{4\pi f_L} + \beta\pi f_H \quad (5.1)$$

$f_L$  and  $f_H$  are the pre-defined lowest frequency and the highest frequency (unit in Hz), respectively. At these frequencies, the combined damping is equal to the assigned damping ratio in the layer, which leads to

$$\alpha = 4\pi\zeta_m f_L \quad (5.2a)$$

$$\beta = \frac{\zeta_m}{\pi f_H} \quad (5.2b)$$

where  $\zeta_m$  is a pre-defined damping ratio in each material. The choice of the lowest frequencies  $f_L$  and  $f_H$  depends on the energy distribution in the frequency spectra. In

the following calculations,  $f_L = 5\text{Hz}$  and  $f_H = 30\text{Hz}$ .

For the comparison with the FEM model, the same amount of Rayleigh damping is used in the BEM model. The Rayleigh damping is governed by the mass damping  $\alpha$  and the stiffness damping  $\beta$ , such that the damping in finite element model is diagonal in the modal analysis. The equation of motion in the finite element model is

$$\mathbf{M}\ddot{\mathbf{x}} + \mathbf{C}\dot{\mathbf{x}} + \mathbf{K}\mathbf{x} = \mathbf{f} \quad (5.3)$$

with

$$\mathbf{C} = \alpha\mathbf{M} + \beta\mathbf{K} \quad (5.4)$$

Assuming a time-harmonic relation  $\mathbf{x} = \mathbf{X}e^{i\omega t}$ , the equation of motion is equivalent to using

$$\mathbf{M}^*\ddot{\mathbf{x}} + \mathbf{K}^*\mathbf{x} = \mathbf{f} \quad (5.5)$$

with

$$\mathbf{M}^* = (1 + \alpha/i\omega)\mathbf{M} \quad (5.6a)$$

$$\mathbf{K}^* = (1 + i\omega\beta)\mathbf{K} \quad (5.6b)$$

without a separate damping matrix. In the BEM model, the mass damping is similarly considered by using a complex density, and the stiffness damping by using a complex elastic modulus

$$\rho^* = \rho(1 + \alpha/i\omega) \quad (5.7a)$$

$$E^* = E(1 + i\omega\beta) \quad (5.7b)$$

In the FEM model, radiation conditions at infinity need to be satisfied. In reality, the vibration radiates as the distance to the source increases. Since the model size is limited, reflections will occur at the boundaries if no measures are taken. In order to limit these reflections, damping layers are created at the edges. The edge elements ensure that the waves can leave the model without reflections. The damping in these edge element should be carefully chosen. They are chosen to be sufficiently large such that the waves are totally radiated. The damping value in the edge elements should not be chosen to be too large, otherwise reflections will occur within the edge elements. The damping in the edge elements increases exponentially with the distance to the center area increases.

In the FEM model created by Movares, the number of edge elements depends on the frequency to be damped. And the element size of adjacent edge elements should not be too large. Large elements are needed to damp out low frequencies, however, they may cause reflections of high frequency waves. In the edge elements, the stiffness damping  $\beta$  value increases exponentially while the stiffness  $E$  decrease exponentially. Reflections are prevented with the joint efforts of increasing  $\beta$  and decreasing stiffness  $E$ .

### 5.1.2.2 Elements mesh

The half-space is idealized to be linear elastic isotropic and homogeneous. It consists entirely of three dimensional volume elements. Element solid 164 is used to create the

subsoil model. It is defined by 8 nodes having the following degrees of freedom at each node: translations, velocities and accelerations in the nodal  $x$ ,  $y$ , and  $z$  directions.

Rayleigh waves are the slowest among P waves, S waves and Rayleigh waves. The element size is determined by the number of elements per Rayleigh wave length and the highest frequency as the basis of the element size according to equation

$$\lambda_R = \frac{c_R}{f} \quad (5.8)$$

A study has shown that the results are accurate enough if the number of elements per wavelength is great than 12. In principle, at least 8 elements per wavelength are required. In the  $xy$  plane, elements of the subsoil model has the dimension  $0.5 \times 0.5$  m. Due to computational costs, it's the optimum smallest value. This is equivalent to using 8 elements per wave length, and it is optimum to consider waves with frequency under 20 Hz for a wavespeed  $c_R = 72\text{m/s}$ . And in the longitudinal  $z$  direction, elements are assigned to have a length of 1m.

The embedded concrete tunnel is modeled using element shell 163. Shell 163 is a 4-noded element with both bending and membrane capabilities. The element has 12 degrees of freedom at each node: translations, accelerations and velocities in 3 nodal directions, and rotations about the nodal axes. The Belytschko-Tsay element formulation is chosen which is based on the Mindlin-Reissner assumption, where extra shear deformation is allowed.

### 5.1.2.3 Boundary conditions

At the vertical plane  $z = 0$  perpendicular to the tunnel axis (see figure 5.1a), symmetry boundary conditions are applied. One needs to be careful with the loading at the symmetry boundary because the amplitude in the response will become doubled in the model. Also, the direction of the response at the other half of the model should be taken into account. Displacements at  $-z$  should be symmetric with the one at  $+z$  for displacements in  $x$  and  $y$  direction while displacements in the  $z$  direction should be anti-symmetric, i.e.,

$$u_x(z) = u_x(-z) \quad (5.9a)$$

$$u_y(z) = u_y(-z) \quad (5.9b)$$

$$u_z(z) = -u_z(-z) \quad (5.9c)$$

which equally holds for the velocity response. At the end side on the vertical plane  $z = L$  perpendicular to the cavity axis, where  $L$  is the length of the model, displacements are constrained to be zero. Although one may expect reflection from the end side of the model, the reflection from the end side is however trivial and can be negligible as long as the length of the model  $L$  is sufficiently large.

### 5.1.2.4 Model parameters

The model adopted is shown in figure 5.1. The geometry and material properties are described in the table below. Properties of concrete tunnel to be included in the model are also listed. Unless specified, these parameters are used throughout this chapter.



Inner radius $R_1$	2.75 m
Outer radius $R_2$	3.0 m
Tunnel wall thickness $t$	0.25 m
Tunnel depth $H$	15 m
Internal load amplitude $P_0$	$8 \times 10^4$ N
Elastic modulus of soil $E_s$	$3 \times 10^7$ N/m <sup>2</sup>
Poisson's ratio of soil $\nu_s$	0.3
Density of soil $\rho_s$	1900 kg/m <sup>3</sup>
Damping ratio in soil $\zeta_s$	0.05
Mass damping in soil $\alpha_s$	3.14
Stiffness damping in soil $\beta_s$	$5.30 \times 10^{-4}$
Shear wave speed in soil $c_{s,s}$	78 m/s
Elastic modulus of concrete $E_c$	$2.5 \times 10^{10}$ N/m <sup>2</sup>
Poisson's ratio of concrete $\nu_c$	0.2
Density of concrete $\rho_c$	2400 kg/m <sup>3</sup>
Damping ratio in concrete $\zeta_c$	0.02
Mass damping in concrete $\alpha_c$	1.26
Stiffness damping in concrete $\beta_c$	$2.12 \times 10^{-4}$
Shear wave speed in concrete $c_{s,c}$	2084 m/s

Table 5.1: Material parameters

## 5.2 The modeling of moving loads

The dynamic response of the model induced by the hyperloop is not obtained by directly applying a moving load in the finite element model due to a huge amount of computational time. Instead, because the space is invariant in the longitudinal direction where the hyperloop travels, equivalent response to a moving load is obtained by convoluting stationary impulse responses. This can result in considerable time savings because the model is only subjected to a stationary impulse load. For the convolution, an integration procedure is required in order to obtain the final response. The way to model moving loads originated from a program called *PULSOS* at Movares and is reproduced in the thesis. Results using this method had been validated to agree well with solutions using a 'real' moving load.

### 5.2.1 Stationary impulse loads

A stationary load means the load is applied on a fixed location and the location does not change with time. Also, an impulse load means the time duration of the load is very short. The response of the system due to this load is the impulse response.

The physical meaning of the convolution rule is straightforward: As the hyperloop (represented by a moving load) moves along a certain path, it is equivalent to applying a series of single pulses along the path. In figure 5.2, the horizontal axis denoted by an arrow represents the tunnel in which the hyperloop travels. The response(displacement/velocity/stress) at the receiver point is of interest.

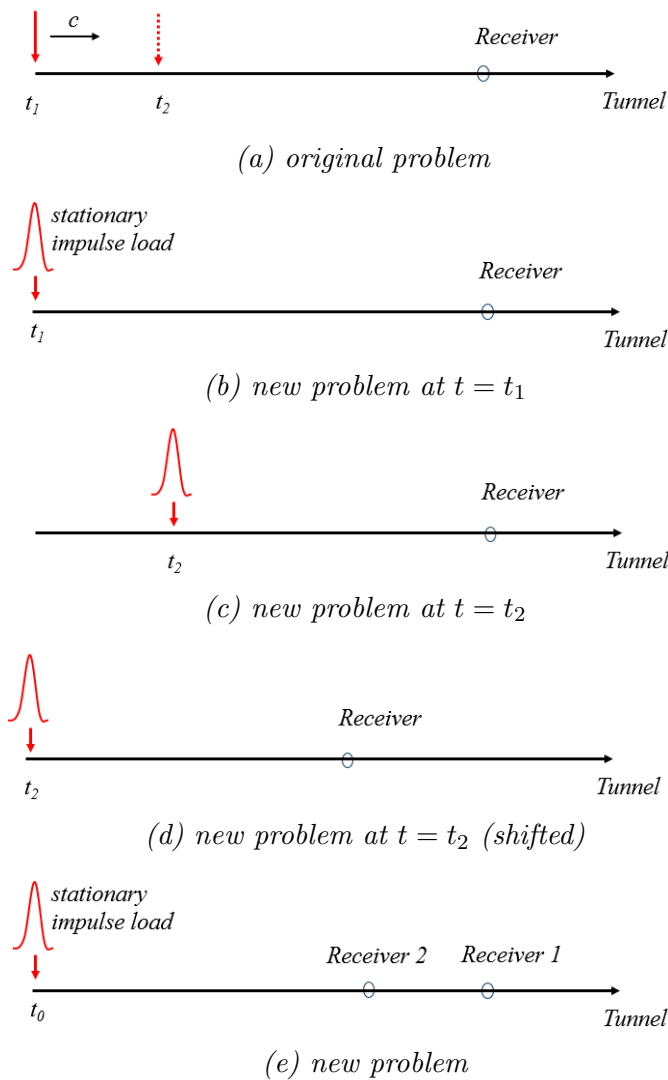


Figure 5.2: Original problem and transformed problem

- (1) As shown in figure 5.2a, a moving load with a constant velocity  $V$  passes the first position at time  $t = t_1$ , and reaches the second position at time  $t = t_2$ .
- (2) Then, the moving load is replaced by applying a first pulse on the first location at time  $t = t_1$  as shown in figure 5.2b and later, applying a second pulse load on the second location at time  $t = t_2$  as shown in figure 5.2c.
- (3) Since the space is invariant along the tunnel, as long as the distance between the source and the receiver remains the same, the response observed at the receiver point remains the same. Both the source and the receiver can be together shifted along the tunnel, figure 5.2c is now represented by figure 5.2d.
- (4) Finally, the original problem in figure 5.2a is transformed to the new problem in figure 5.2e. Only one stationary impulse load is needed and response due to the moving hyperloop can be obtained by synthesizing the responses in receivers located at different positions.

In this way, a considerable amount of computational time can be reduced. There are several important aspects about placing these receivers: First, these receivers should

be placed in the direction of the hyperloop movement. Secondly, these receivers should also be placed at a moderate space interval so that the waves can be properly described. Thirdly, the number of these receivers should be large enough, or the distance between the stationary load and the furthest receiver should be large enough, in order not to lose any information. The ideal case is the response in the furthest receiver is negligibly small. Last but not the least, since we are making use of the impulse response, the duration of these pulses should be short enough to represent an ideal dirac-delta function.

In the FEM model, calculations are carried out in the time domain. The profile of the load is shown in figure 5.3. In figure 5.3a, the stationary impulse load is applied at one of the tunnel ends where the symmetry boundary conditions are applied. The load distribution is the same as the one in the previous chapter, for comparison purpose. The load with a constant magnitude is smeared in the circumferential direction at the lower part of the tunnel. The load exerted on the system has the form

$$p_r(\theta_1, z, t) = \frac{P_0}{\frac{\pi}{2} \times R_1 \times 1} \left\{ H(\theta_1 - \frac{\pi}{4}) - H(\theta_1 - \frac{3\pi}{4}) \right\} \delta(z - Vt) \quad (5.10a)$$

$$p_\theta(\theta_1, z, t) = 0 \quad (5.10b)$$

$$p_z(\theta_1, z, t) = 0 \quad (5.10c)$$

where  $P_0$  represents the magnitude of the gravity force. Equation (5.10) means in the 2D plane  $xoy$ , the gravity force is smeared in the circumferential direction at the lower part of the tunnel within the range  $[\frac{\pi}{4}, \frac{3\pi}{4}]$ , while in the longitudinal direction, it is a point load represented by the Dirac-delta function.

Receivers are placed along the tunnel axis. Due to this pulse, waves will propagate through the soil and along the tunnel. Time histories in these receivers are recorded in the FEM calculation and later used in the convolution. Figure 5.3b shows the load profile, where the maximum amplitude  $A$  corresponds to the actual gravity force from the hyperloop and the total energy is simply the area under the curve. Here, time duration  $\Delta t$  of the impulse load is 0.005 seconds. The amplitude spectrum of the short pulse should remain constant up to a sufficiently high frequency, because the amplitude spectrum of an ideal impulse is a constant over all frequencies. Also, a proper scaling factor is needed

$$E_p = \frac{1}{2} A \Delta t \quad (5.11)$$

The impulse response of the system should be the response directly from the FEM model divided by this factor, i.e.,

$$U_{\text{real}} = \frac{U_{\text{model}}}{E_p} \quad (5.12)$$

where the impulse is assumed to have a unit amplitude. The scaling factor is needed because the integration of an ideal impulse over time should be 1, while in the FEM calculations, the ideal impulse is approximated using a triangle profile which has an actual area. The integration of the approximated pulse over time is equal to  $E_p$ , rather than 1.

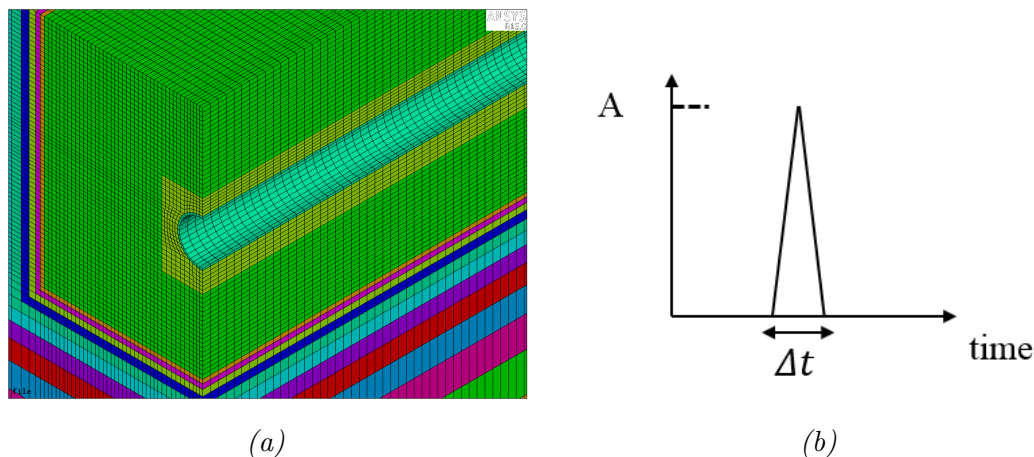


Figure 5.3: Position and time history of the impulse load

Note that the impulse response discussed in this chapter is similar to the Green's functions mentioned in Chapter 2. Earlier, the 2.5D Green's functions are fundamental solutions of a half-space due to a harmonic line load. The impulse response here is expressed in the form of numerical values and does not have an analytical form. The numerical form of impulse response has an advantage because it automatically takes into account all types of waves when a more complex geometry is used, while the analytical form of Green's functions becomes complicated [23].

### 5.2.2 Convolution for constant moving loads

The numerical form of the impulse response is expressed in the following form:

$$G(\mathbf{x}, t; \mathbf{x}_0, \tau) \quad (5.13)$$

where  $\underline{x} = (x, y, z)$  is the location of the receivers and  $\underline{x}_0 = (x_0, y_0, z_0)$  is the location of the excitation;  $t$  is the observation time, and  $\tau$  is the time instant of excitation. Let us now assume the in-plane coordinates are fixed, namely,

$$x = x_0 = c_1, y = y_0 = c_2 \quad (5.14)$$

where  $c_1$  and  $c_2$  in equation (5.14) are constants, so that the impulse response is only a variable with the location in longitudinal direction ( $z$ -direction). Now equation (5.13) can be written as an 1D case:

$$G(z, t; z_0, \tau) \quad (5.15)$$

For a general case, the response of a system in time domain can be computed by convoluting the impulse response of the system with the applied load  $f(z_0, \tau)$ , which is applied on location  $z = z_0$  at time  $t = \tau$ .

$$u(z, t) = \int_{-\infty}^{\infty} \int_{-\infty}^{\infty} G(z, t; z_0, \tau) f(z_0, \tau) dz_0 d\tau \quad (5.16)$$

Therefore, the vibration of any arbitrary position due to an external load can be computed by convoluting the impulse response with the load. In this case, the applied load is a

hyperloop pod, which is a moving load with a constant magnitude and a constant velocity  $V$ . Assuming a unit amplitude, it can be written as

$$f(z_0, \tau) = \delta(z_0 - V\tau) \quad (5.17)$$

Equation(5.16) can be rewritten as

$$u(z, t) = \int_{-\infty}^{\infty} \int_{-\infty}^{\infty} G(z, t; z_0, \tau) \delta(z_0 - V\tau) dz_0 d\tau \quad (5.18)$$

And using the shifting property of the dirac-delta function, integral(5.18) is simplified as

$$u(z, t) = \int_{-\infty}^{\infty} G(z, t; V\tau, \tau) d\tau \quad (5.19)$$

As stated before, since the space is invariant in the longitudinal direction, considering a linear-time-invariant system, equation(5.19) is equivalent to

$$u(z, t) = \int_{-\infty}^{\infty} G(z - V\tau, t - \tau; 0, 0) d\tau \quad (5.20)$$

Equation (5.20) is essentially the mathematical explanation of figure 5.2. By applying one stationary impulse load on location  $z_0 = 0$  at time  $t = 0$ , response at any arbitrary position due to a moving load can be computed by applying this convolution integral. Location of the receivers is found based on different values of  $\tau$ . And of course, the time response history of these receivers should comply with the global time  $t$  by applying a time shift  $\tau$ .

In the end, an integration with respect to  $\tau$  is needed. The physical meaning of  $\tau$  varying from  $-\infty$  to  $+\infty$  is that one needs to consider the situation when the hyperloop has not yet passed the receiver, and after the hyperloop has passed the receiver. In fact, this infinity needs to be truncated at a sufficiently larger value such that the response in the receiver is nearly damped out and has little contribution in the final response. To accurately evaluate the integral Eq.(5.20), two criteria must be satisfied: the truncated  $\tau$  should be larger enough and the step size  $d\tau$  should be small enough.

It can also be seen from equation(5.20) that all points along the  $z$ -direction will experience exactly the same motion, but only with a time delay. This is again because of the invariant space in the longitudinal direction. Therefore, it doesn't matter which point along the  $z$ -direction is looked at. For example, if the receiver is located on  $z = 0$ , equation(5.20) is transformed as

$$u(z, t) = \int_{-\infty}^{\infty} G(-V\tau, t - \tau; 0, 0) d\tau \quad (5.21)$$

Furthermore, if more than one moving loads are to be considered, for example, 2 axles of the hyperloop pod are considered, the moving load expression (5.17) can be easily augmented

$$f(z_0, \tau) = \delta(z_0 - V\tau) + \delta(z_0 - V\tau + L_a) \quad (5.22)$$

where  $L_a$  is the distance between two axles. And the correspond response equation(5.21) will simply change to

$$u(z, t) = \int_{-\infty}^{\infty} G(-V\tau, t - \tau; 0, 0) d\tau + \int_{-\infty}^{\infty} G(-V\tau + L_a, t - \tau; 0, 0) d\tau \quad (5.23)$$

The numerical evaluation of the convolution integral (5.21) is realized in a different manner than normal. To start with, since we place our interest at the origin point with the in-plane coordinates (0,0), then this is our observation point. Time response histories are recorded in the nodes which have the same in-plane coordinates but different out-of-plane coordinate, i.e., (0,0, $L_e$ ), (0,0, $2L_e$ ),  $\dots$ , (0,0, $L$ ), where  $L_e$  is the element size and  $L$  is the length of the model). Secondly, these time response signals are shifted with a time delay  $\tau$ . The time shift  $\tau$  is a different value for each node. And the time shift increment  $\Delta\tau$  is assigned to be equal to the constant time step size in the finite element model. Within the time shift increment  $\Delta\tau$ , the distance which the moving load is able to travel is

$$\Delta L = V \cdot \Delta\tau \quad (5.24)$$

for the case where the moving load has a constant speed. And then, shifted time response histories of each node should have the time in common, which is called the global time. In the end, at each time instant in the global time, an integration is carried out with space  $z$ . This is the idea explained in figure 5.2(a)(b)(c).

The shifting process of the node information (time response histories) is in fact creating a series of short pulses. And the integration that follows is actually synthesizing the contribution from these pulses. In this way, the moving load is modeled as a series of consecutive short pulses.

### 5.2.3 Convolution for accelerating moving loads

One of the advantages of the convolution is that the response due to an accelerating moving load can be found in a very similar manner. The difference between a constant moving load and an accelerating moving load: the moving load travels a different distance within the same time interval. Earlier the distance is a constant, which is now changed based on the relation

$$\Delta L = V_0 \cdot \Delta\tau + \frac{1}{2}a(\Delta\tau)^2 \quad (5.25)$$

for the case where the moving load has an acceleration. In this equation,  $V_0$  is the initial velocity of the current time interval,  $\Delta t$  is the time shift increment and  $a$  is the acceleration of the moving load.

For the accelerating case, the time shift  $\tau$  and its increment  $\Delta\tau$  remains the same as those for the constant moving load case. However, since the distance which the moving load travels is changed, the integration procedure with respect to  $\tau$  changes. It means the pulses are no longer at the same positions as those in the constant moving load case.

In this case, the applied load is a hyperloop pod, which is a moving load with a constant magnitude and a changing velocity  $V$ . Assuming a unit amplitude, the load can be written as

$$f(z_0, \tau) = \delta(z_0 - (V_0 \cdot \tau + \frac{1}{2}a\tau^2)) \quad (5.26)$$

Equation(5.16) can be rewritten as

$$u(z, t) = \int_{-\infty}^{\infty} \int_{-\infty}^{\infty} G(z, t; z_0, \tau) \delta(z_0 - (V_0 \cdot \tau + \frac{1}{2}a\tau^2)) dz_0 d\tau \quad (5.27)$$

And using the shifting property of the dirac-delta function, integral(5.27) is simplified as

$$u(z, t) = \int_{-\infty}^{\infty} G(z, t; V_0 \cdot \tau + \frac{1}{2}a\tau^2, \tau) d\tau \quad (5.28)$$

As stated before, since the space is invariant in the longitudinal direction, considering a linear-time-invariant system, equation(5.28) is equivalent to

$$u(z, t) = \int_{-\infty}^{\infty} G(z - (V_0 \cdot \tau + \frac{1}{2}a\tau^2), t - \tau; 0, 0) d\tau \quad (5.29)$$

By applying one stationary impulse load on location  $z_0 = 0$  at time  $t = 0$ , response at any arbitrary position due to an accelerating moving load can be computed by applying the convolution integral (5.29). In the end, an integration with respect to  $\tau$  is needed.

## 5.3 Results obtained by the FEM

### 5.3.1 Hyperloop a constant speed

#### 5.3.1.1 Impulse responses

Before applying the convolution, the stationary impulse responses of vertical displacement and vertical velocity at the tunnel invert under the loading are shown in figure 5.4 and in figure 5.5, for the case where the tunnel is modeled using solid elements and for the case where the tunnel is modeled using shell elements, respectively.

The responses with different  $z$  coordinates in the tunnel have similar wave forms, because waves are transmitted from the loading position to the end side of the model. Similarly, time histories of displacement or velocity at nodes which are parallel to the tunnel axis are also recorded. In the convolution process, these time histories are shifted according to the moving load speed, and then integrated at every time instant.

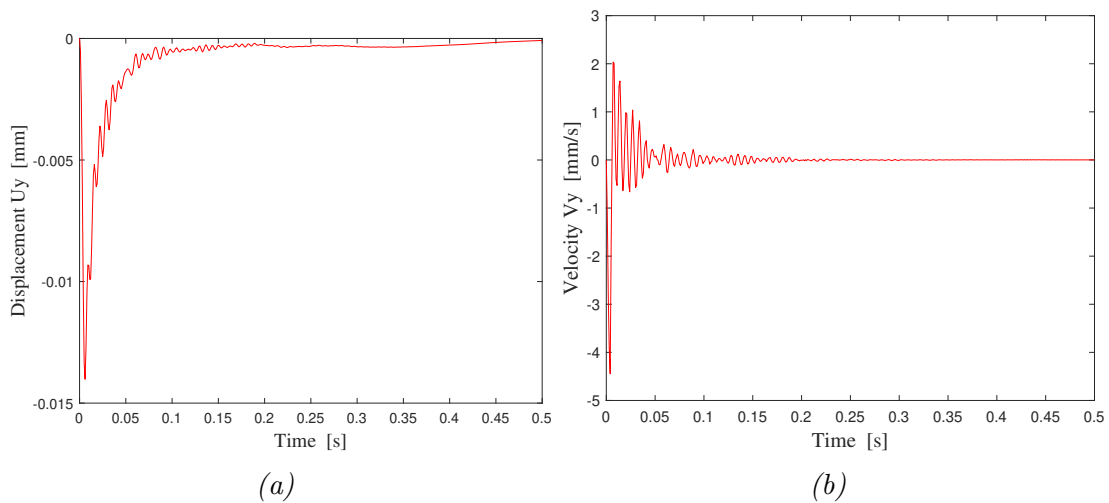


Figure 5.4: Impulse responses exactly at tunnel invert under the load (tunnel modeled using solid elements)

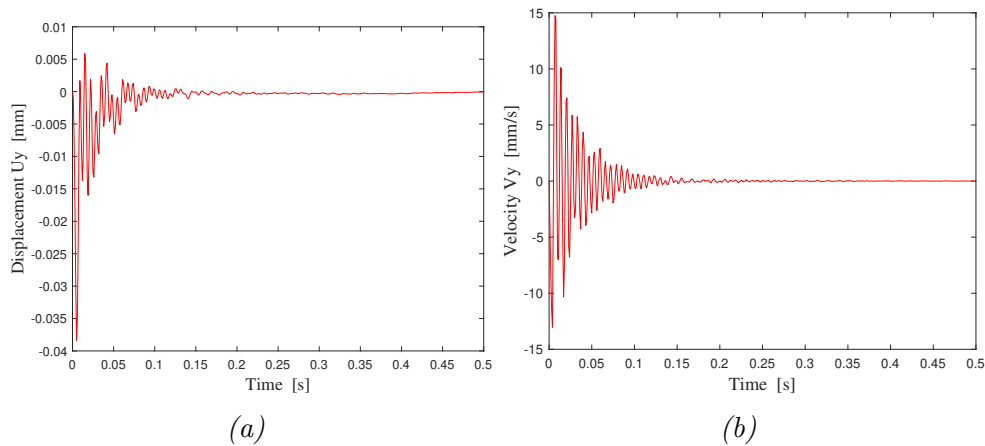


Figure 5.5: Impulse responses exactly at tunnel invert under the load (tunnel modeled using shell elements)

From figure 5.4 and figure 5.5, it is found that the solid elements and shell elements have very different dynamic behaviours. Solid elements behave stiffer than the shell elements, which can be seen from the amplitudes and the deformed shapes. The amplitudes of solid elements are in general smaller than those of shell elements. The short pulse load results in a quasi-static deformation of the solid elements while the response of the shell elements is more oscillatory. Higher frequency content is found in the response using the shell elements.

Figure 5.6 also shows the impulse response of vertical velocity along the longitudinal  $z$  direction  $z < 30$ m, for the case where the tunnel is modeled using solid element and for the case where the tunnel is modeled using shell elements, respectively. It is further proven that the response by using the shell elements has a higher frequency content. In figure 5.6(a), waves are properly described with the element size  $L_e = 1$  m because at least 3 nodes are used to describe waves in one period. However, for figure 5.6(b), element size  $L_e = 0.5$ m is still not enough to describe waves in one period. The element size  $L_e = 0.5$ m is considered to be the minimum element size for an acceptable computational time.

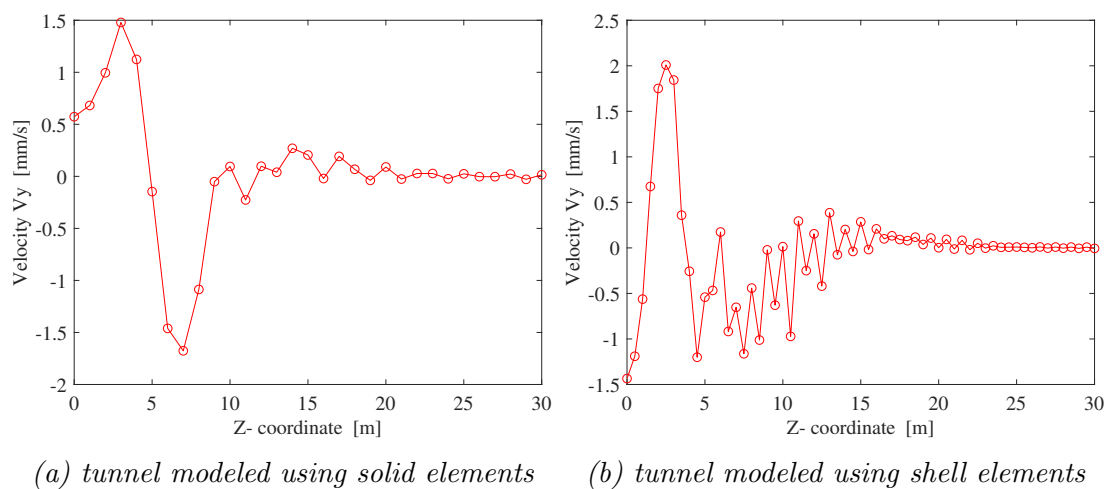


Figure 5.6: Impulse responses at tunnel invert  $z < 30$ m at time instant  $t = 0.012$ s



### 5.3.1.2 Convergence of the convolution

The purpose of this part is to ensure the FEM model produces unique and accurate results. The integral eq.(5.20) or eq.(5.21) stated previously must be converged. The convergence of the integral is mainly influenced by the following factors:

- truncated bound limit of integrals  $\tau_{\max}$  (or total length of the time response history  $T$ )
- step size of integrals  $\Delta\tau$  (or time step size in the time response history  $dT$ )
- element size in the longitudinal direction  $L_e$
- model size in the longitudinal direction  $L$

Figure 5.7 shows the effects of varying these parameters on the response. The response is calculated by using the solid elements to model the tunnel. An example is given for the time domain response of vertical velocity at point A on the ground surface for the case  $V = 75\text{m/s}$ . The response is computed by following the previous convolution principle. Since the observation is placed at  $(0, 0)$ , time instant  $t = 0$  corresponds to the moment when the hyperloop exactly passes the point of observation. For each parameter, 3 different values are chosen for the comparison.

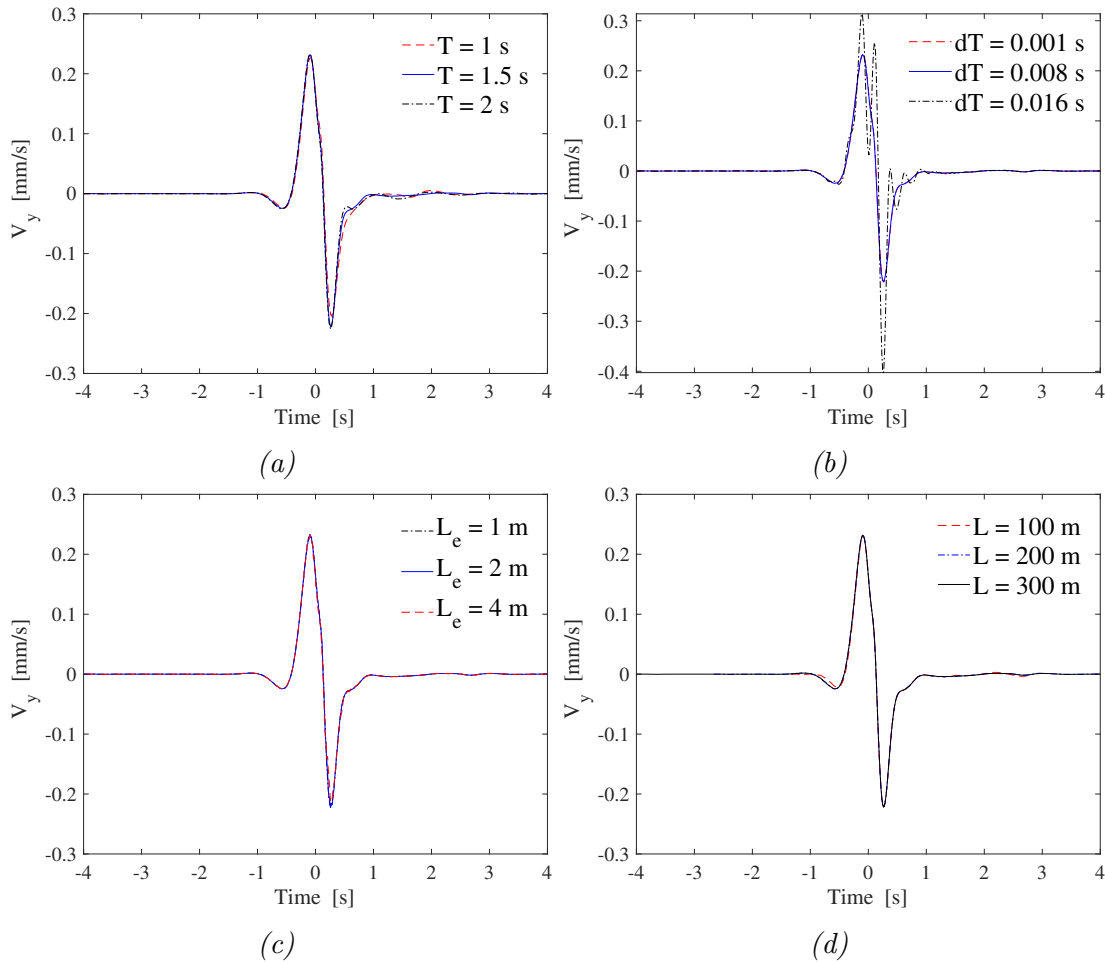


Figure 5.7: Time domain response of vertical velocity  $V_y$  at point A ( $V = 75\text{m/s}$ ) to show (a) effect of time record length; (b) effect of time step ; (c) effect of element size and (d) effect of model length

Figure 5.7(a) shows the effect of truncated bound limit  $\tau_{\max}$  (or time record length). It is clearly shown that a too short record length ( $T = 1\text{s}$ ) does not provide convergence and therefore results in an inaccuracy. On the other hand, too long record lengths ( $T = 2\text{s}$ ) can involve redundant information and therefore produce an artificial wave pattern in the late response ( $t > 0.5\text{s}$ ). This, however, does not change the peak values. Therefore, an ideal time record length should be sufficiently large to provide converged results.

Figure 5.7(b) shows the effect of time step size in the integrals (or the time step size in the time response history). The time step size  $\Delta t$  directly determines the increment of the time shift  $\Delta\tau$  for the time histories for each node. The time step size should be small enough because 'snapshots' are made for the moving load every time step. The time step value used in the following calculations is 0.001s. It is found that a larger value such as 0.008s can still guarantee the same accuracy (for  $V = 75\text{ m/s}$ ). For the current case study, time step size 0.001s is sufficiently small for obtaining a convergence.

Figure 5.7(c) shows the effect of using different element sizes in the longitudinal direction. It is observed that element size in the longitudinal direction will not have a large influence on the final response (for  $V = 75\text{ m/s}$ ). This implies a coarse element mesh in this direction can speed up the calculation and in the meantime guarantee the same accuracy. In this case,  $L_e = 2\text{m}$  can provide converged results.

Figure 5.7(d) shows the effect of using different model lengths. It is stated that the distance between the stationary load and the furthest node should be large enough, in order not to lose any information. The ideal case is the response in the furthest node is negligibly small. A manual trial is needed to determine the location of the furthest node. As shown in figure 5.7(b), 200-meter is the minimum model size to satisfy the convergence requirement. A further reduction in the model length may result in amplitude reduction at the peak values. This is because the number of pulses is not sufficient enough, resulting in a convergence problem. An important hint is: the wave attenuation near the stationary impulse location ( $z < 200\text{ m}$ ) should be well captured, while the waves in the far field ( $z > 200\text{ m}$ ) are negligibly small and rarely make contribution to the final response.

The convergence of the convolution integral is equally good for other cases where the hyperloop speed is as high as 1000 m/s, as shown in figure 5.8.

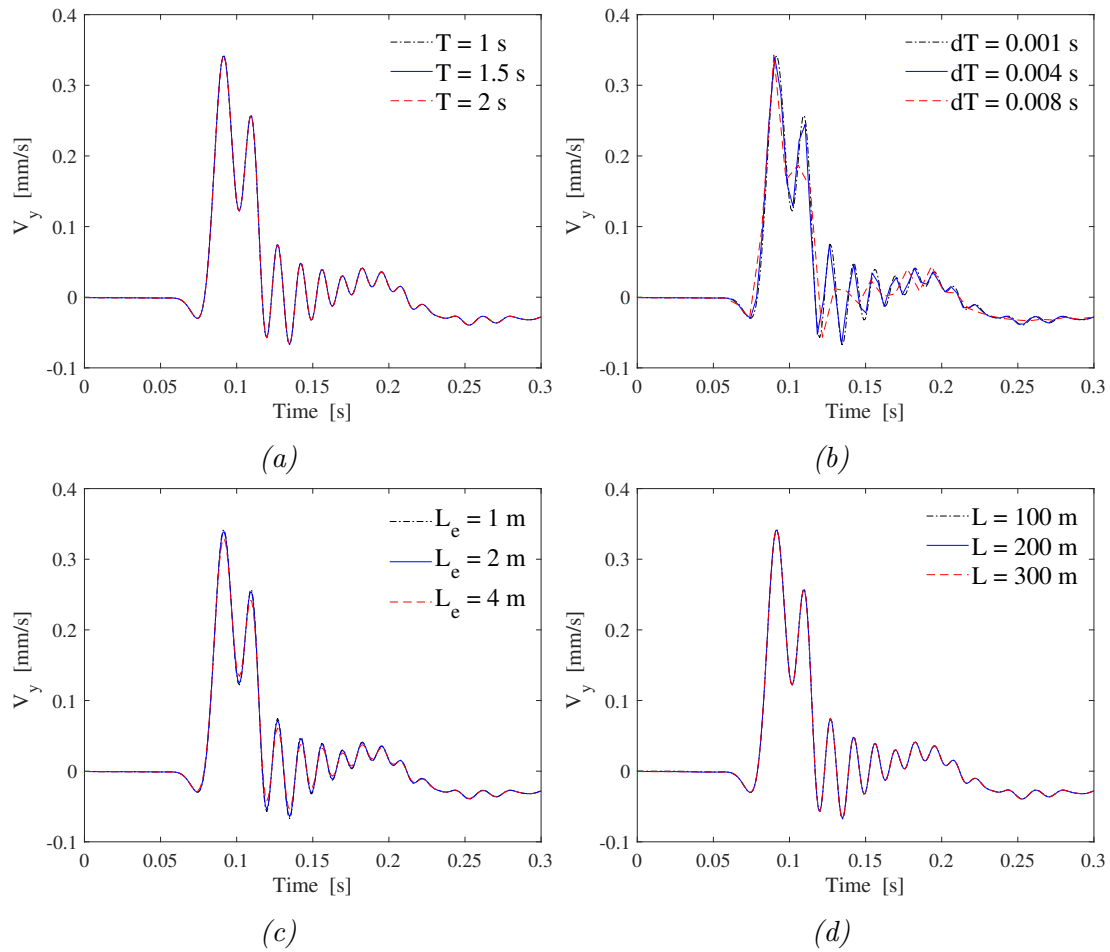


Figure 5.8: Time domain response of vertical velocity  $V_y$  at point A ( $V = 1000\text{m/s}$ ) to show (a) effect of time record length; (b) effect of time step ; (c) effect of element size and (d) effect of model length

In the calculations that follow, the total length of the time response history  $T = 2\text{s}$ , the time step size  $dT = 0.001\text{s}$  and the model size is chosen to be  $200\text{ m}$  long. The element size  $L_e = 1\text{ m}$  in the case where the tunnel is modeled using solid elements and the element size  $L_e = 0.5\text{ m}$  in the case where the tunnel is modeled using shell elements.

### 5.3.2 Comparison between FEM and BEM

a) At point A on the ground surface

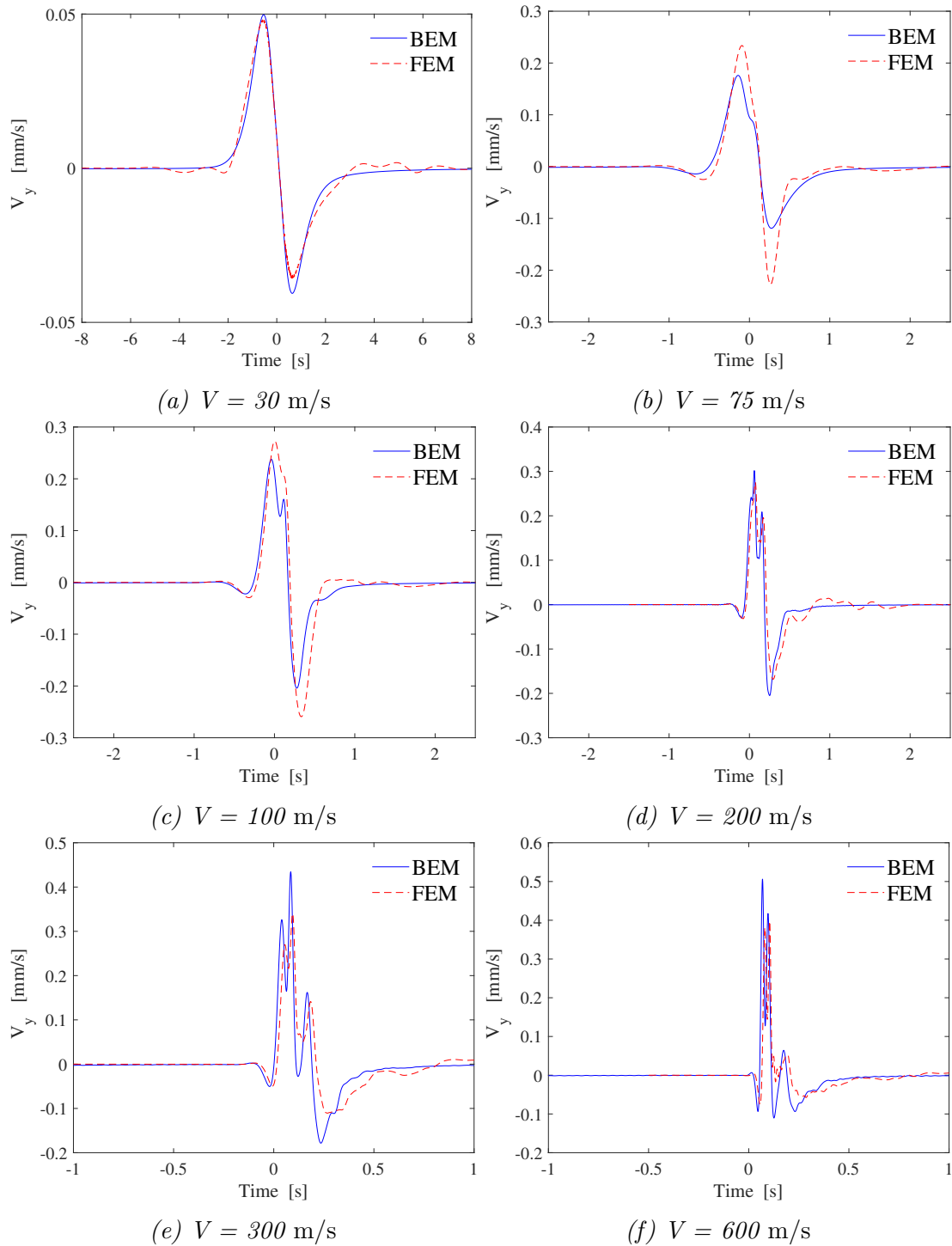


Figure 5.9: Time domain comparison of velocity response at point A for different hyper-loop velocities (FEM using solid elements)

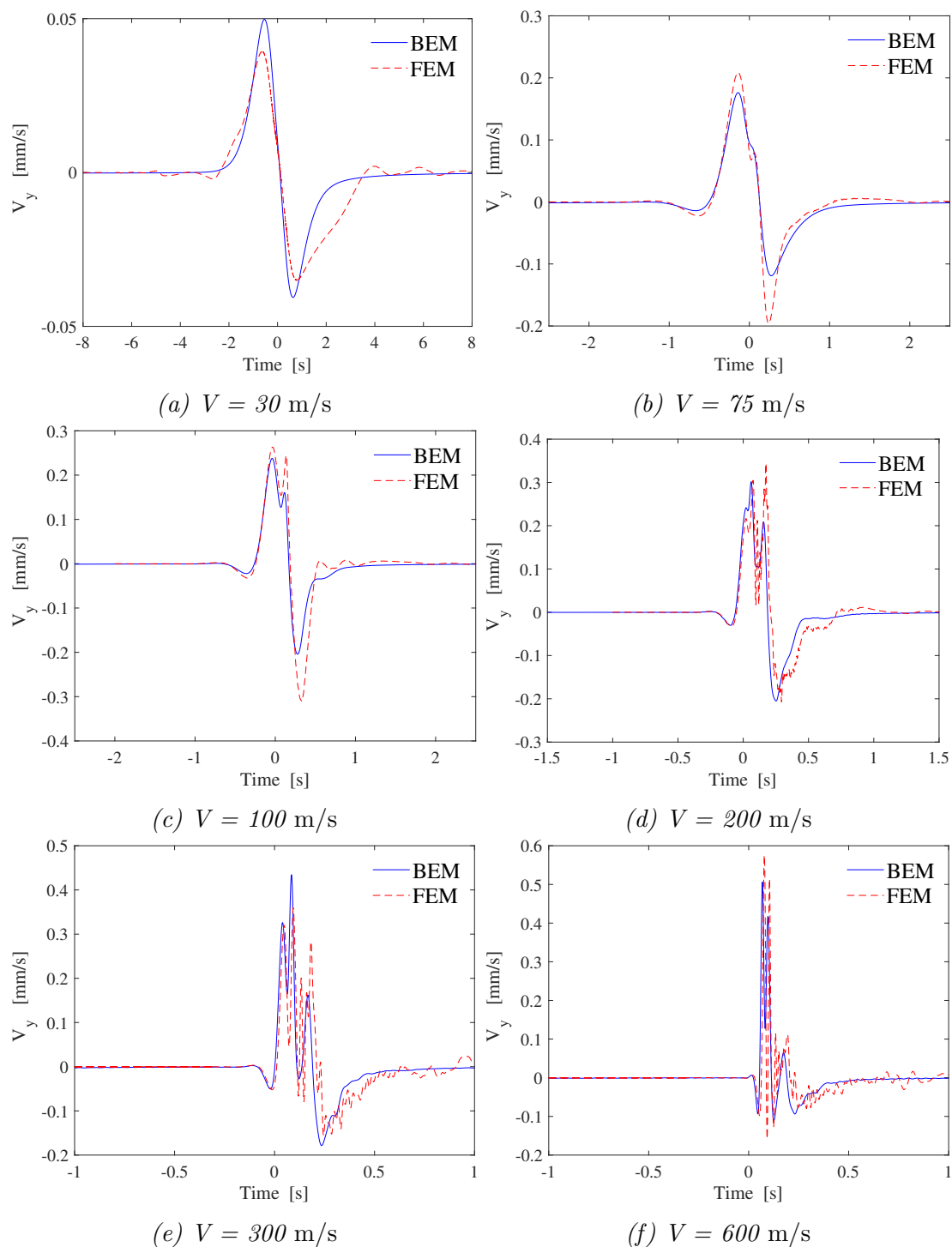


Figure 5.10: Time domain comparison of velocity response at point A for different hyper-loop velocities (FEM using shell elements)

Figure 5.9 and figure 5.10 show the time domain comparison of velocity response at point A for 6 cases,  $V = 30$  m/s, 75 m/s, 100 m/s, 200 m/s, 300 m/s and 600 m/s. Figure 5.9 shows the response where the tunnel is modeled using solid elements while figure 5.10 shows the response where the tunnel is modeled using shell elements. The physical phenomena are clearly shown: 1. with the increase of hyperloop speed, the velocity response at the surface changes from quasi-static deformation to wave-like oscillation because of the strong wave radiation effect at high velocities. More than one peaks start to develop with the increase in the hyperloop speed; 2. the maximum amplitudes of velocity response keeps monolithically increasing when the hyperloop speed increases from  $V = 30$  m/s to  $V = 600$  m/s, even after the hyperloop speed is higher than the Rayleigh wave speed in the soil ( $V = 72$  m/s); 3. The time duration of the velocity response becomes shorter when the hyperloop speed is higher. The first disturbance which the receiver observes is getting later at high hyperloop speeds, compared to low hyperloop speeds. It is worth noticing that for the case  $V = 600$  m/s, there is no response before the time instant  $t = 0$  s.

Judging from figure 5.9 and figure 5.10, results from the BEM are in close agreements with those from the FEM in terms of the wave patterns and in the maximum values. The difference is the largest for  $V = 75$  m/s (close to the Rayleigh wave speed of the soil). For the FEM models, both the solid elements and the shell elements are able to describe the dynamic behaviour of the soil, sharing very similar wave patterns. The comparisons of velocity response using the solid elements are closer to those by the BEM. For high hyperloop speeds  $V = 300$  m/s and  $V = 600$  m/s, using the solid elements is more converged than using the shell elements because curves are shown to be more smooth. A probable explanation is that the high frequency content in the impulse response by the shell elements is difficult to be accurately described by the current element size (as shown in figure 5.6(b)). The lack of convergence results in more bumpy curves for high speeds simply because the shift of the impulse response for high hyperloop speeds is less when compared to low hyperloop speeds, according to Eq.(5.20) and Eq.(5.24). And when the time shift for the impulse response becomes less, the convoluted result relies more on the original shape of the impulse response. We conclude that there is a convergence problem in computing the FEM model, which is related to the impulse response itself, and not to the convolution integral. This problem is more prominent for high hyperloop speeds.

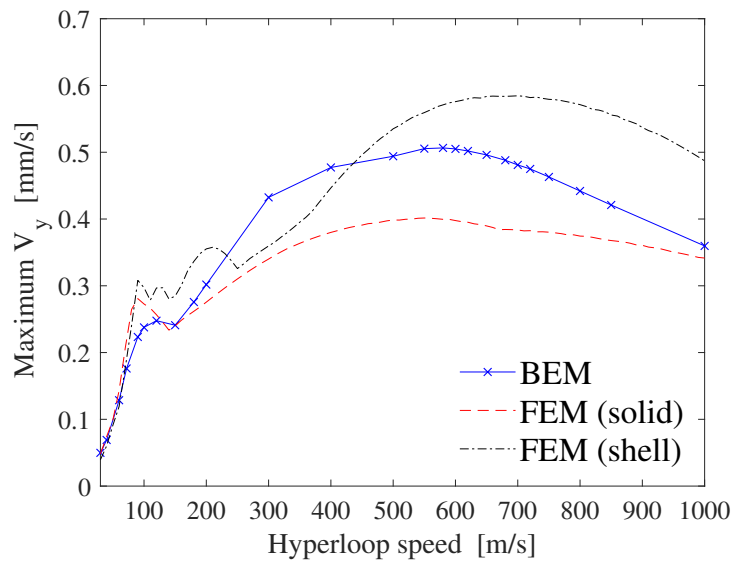


Figure 5.11: Maximum velocity response at point A versus hyperloop speed  $V$

Figure 5.11 gives the maximum velocity comparison for different hyperloop speeds at point A. This involves recording the maximum absolute value in the time domain response for each  $V$  (up to 1000 m/s). The same procedure is carried out for the FEM model and BEM model. As is discussed in figure 5.10, the results from the BEM and those from the FEM using the solid elements are matched better than using the shell elements. The largest difference is observed at critical speed  $V = 75$  m/s. All three models have revealed the same physical phenomenon that the Rayleigh wave speed of the soil ( $V = 72$  m/s) is not the only critical speed. The maximum velocity response in the soil still keeps increasing after the hyperloop speed is higher than the Rayleigh wave speed. At the hyperloop speed  $V = 600$  m/s, a second peak is observed in the maximum velocity response. At this speed, the maximum velocity on the surface can be as high as approximately 0.5 mm/s.

According to a study from Akbarov *et al* on the dynamics of the moving load acting in the interior of an hollow cylinder surrounded with elastic medium [24], the critical velocity of the moving load can be determined through analysis of the dispersion curves of the longitudinal and flexural waves propagating in the tunnel in the direction of the moving load. From the study, it is revealed that the critical velocity is related to the elastic modulus, the density, the Poisson's ratio of the soil and of the tunnel. The critical velocity is also related to the thickness of the tunnel and the moving load distribution pattern. According to Akbarov's study, this critical velocity for a elastic modulus ratio case  $E_s/E_c = 0.01$  can be as low as  $0.4 \times C_{s,c}$  where  $C_{s,c}$  is the shear wave speed in the tunnel. For the current case study, the ratio of elastic modulus  $E_s/E_c = 0.001$ , therefore, we expect the critical velocity to be lower than  $0.4 \times C_{s,c} = 0.4 \times 2084 = 834$  m/s. The critical moving load velocity for the current case study is shown to be around  $V = 600$  m/s by using the current models.

## b) At the tunnel invert

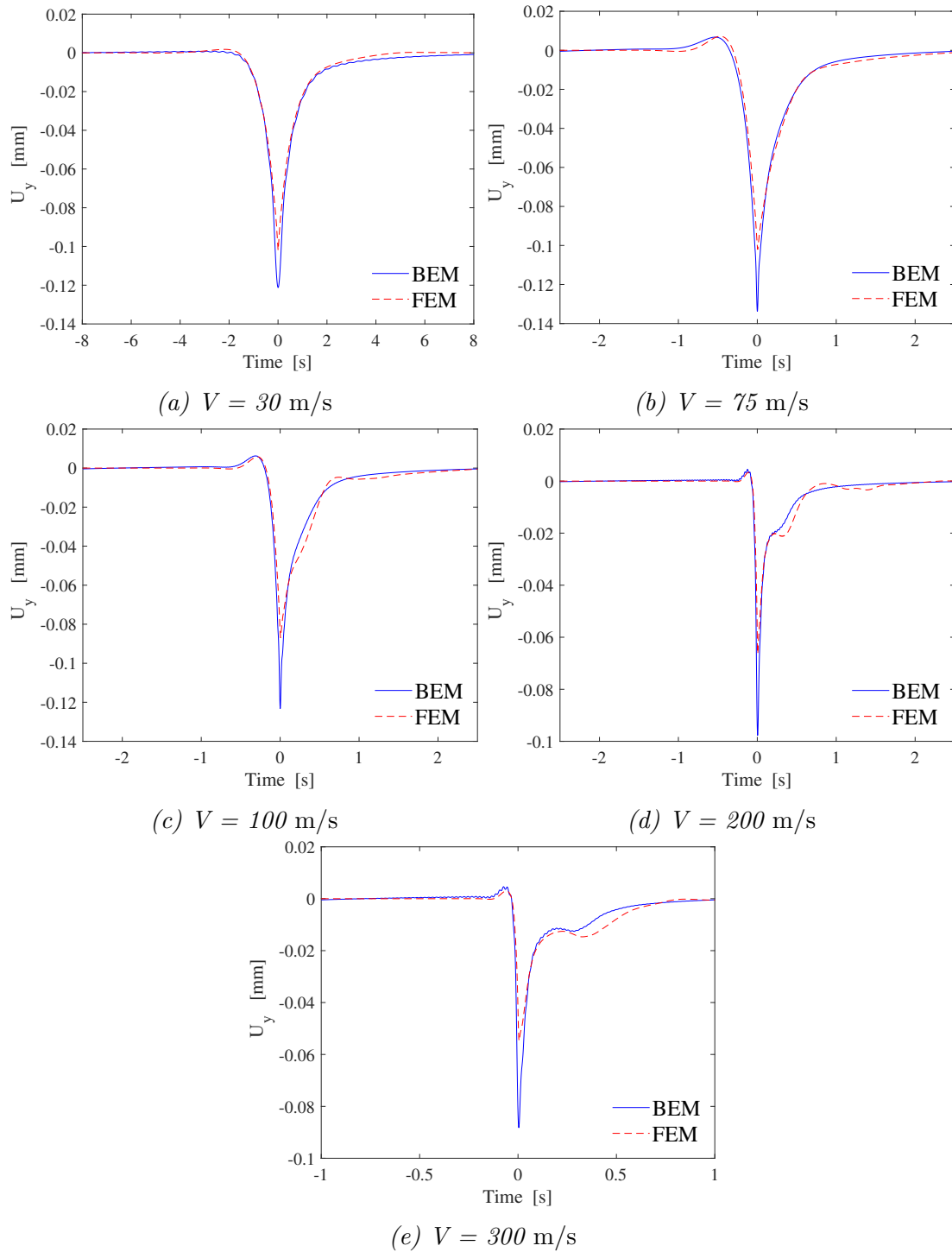


Figure 5.12: Time domain comparison of displacement response at tunnel invert for different hyperloop velocities (using solid elements)



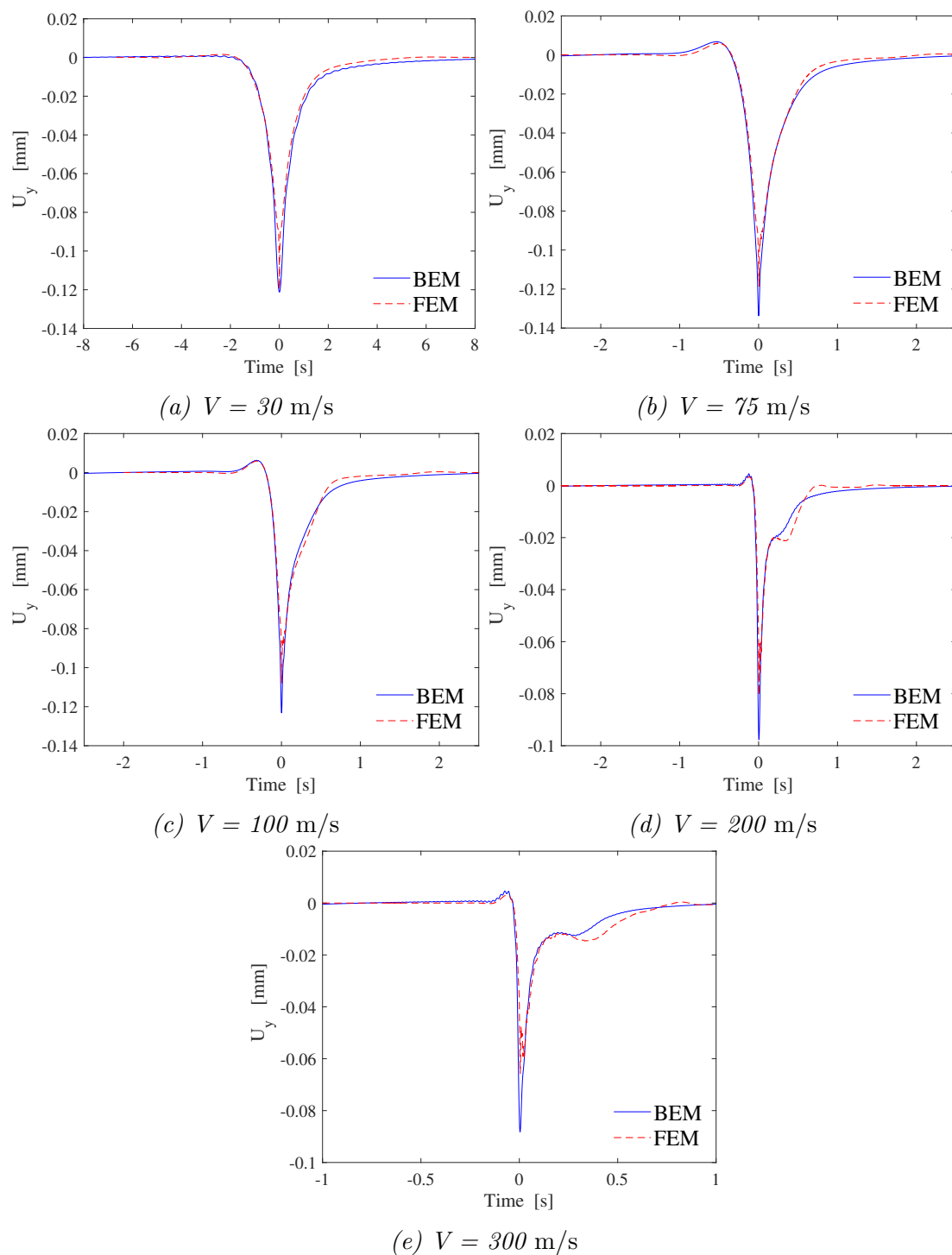


Figure 5.13: Time domain comparison of displacement response at tunnel invert for different hyperloop speeds (using shell elements)

Figure 5.12 and figure 5.13 show the time domain comparison of displacement response at the tunnel invert for 5 cases,  $V = 30$  m/s, 75 m/s, 100 m/s, 200 m/s and 300 m/s. Figure 5.12 shows the response where the tunnel is modeled using solid elements while figure 5.13 shows the response where the tunnel is modeled using shell elements.

For the case  $V = 30$  m/s, the observation point at the tunnel invert experiences a quasi-static deformation which lasts for 4 seconds. At  $t = 0$ , the displacement curves are steep because the observation is located under the loading. Waves are received before and after the load passes the observation point, which is probably due to the bending behavior of the tunnel in the longitudinal direction. The bending behaviour also explains the reason why a compressive stress is observed at the tunnel invert before and after the hyperloop passes the observation point in figure 4.11. Waves in front of the hyperloop are well captured at the time  $t < 0$ . The displacement responses for velocity from  $V = 30$  m/s to  $V = 300$  m/s are quasi-static simply because the bending stiffness of the tunnel is high, which attributes to the large elastic modulus of the soil and the larger concrete wall thickness. Furthermore, the time duration of the response becomes shorter with the increase in the hyperloop speed. Also, the maximum displacement is observed at the Rayleigh wave speed of the soil.

Judging from figure 5.12 and figure 5.13, results from the FEM and those from the BEM are in very close agreements. The largest difference occurs at the Rayleigh wave speed. The comparisons of displacement response using the shell elements are closer to those by the BEM. In the current case study, solid elements tend to give more conservative results and thus behave stiffer, while the shell elements deforms more and tend to give larger results. The dynamic behaviour of these elements are also shown in the impulse responses from figure 5.4 and figure 5.5.

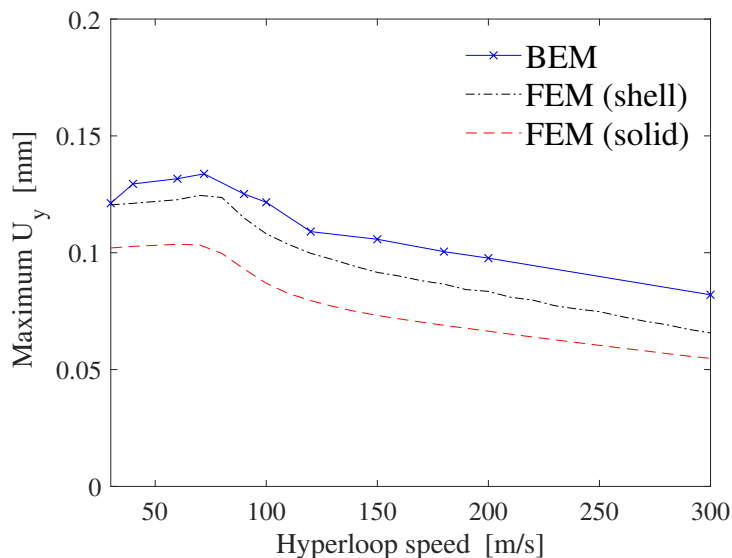


Figure 5.14: Maximum displacement response at tunnel invert versus hyperloop speed  $V$

Similarly as figure 5.11, figure 5.14 gives the maximum displacement comparison for different hyperloop speeds (up to 300 m/s) at the tunnel invert. The maximum displacement is almost constant for speeds lower than 50 m/s because the hyperloop can only excite an eigen field which moves stationary relative to it at low speeds. The deformation value is very close to the static deformation. The curve looks like moderately damped mass-spring system response because for the current case, the bending stiffness of the tunnel is high. Therefore, the resonance of the soil at the critical speed  $V = 72\text{m/s}$  does not influence the tunnel too much. For the three models, a peak in the maximum response can be observed at the Rayleigh wave speed  $V = 72\text{ m/s}$  and for  $V > 72\text{ m/s}$ , the maximum amplitude of displacement decays monotonically.

### 5.3.3 Hyperloop with an acceleration

#### 5.3.3.1 Model description

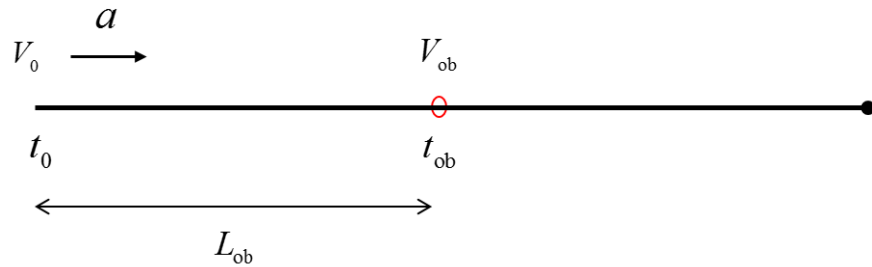


Figure 5.15: Schematic representation of an accelerating hyperloop

In this section, the scenario where a hyperloop with an acceleration passes the Rayleigh wavespeed is discussed, because the displacement response at the tunnel invert is the largest at  $V = 72\text{m/s}$  according to figure 5.14. Results presented follows the calculation procedure discussed in section 5.2.3. Since the hyperloop speed changes with time, the excitation changes with time, therefore, the response is time-dependent. In other words, the response is now transient rather than steady-state. In this section, we consider a constant acceleration, i.e.,

$$a = \text{const.}, V = a \times t \quad (5.30)$$

In figure 5.15, the path at the tunnel invert is represented as an 1D axis. A hyperloop travels from one side of the tunnel to the other side. The tunnel has a length  $L = 600\text{ m}$  in total. The hyperloop has an acceleration value  $a$ , and an initial velocity  $V_0 = 30\text{ m/s}$  at the start point. An observation is placed in the middle of the tunnel axis, meaning that the distance  $L_{\text{ob}}$  to the start point is

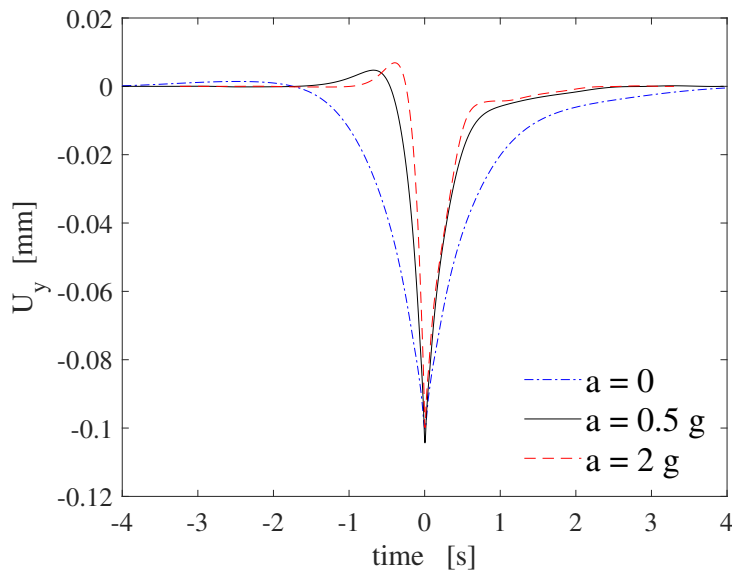
$$L_{\text{ob}} = L/2 = V_0 \cdot t_{\text{ob}} + \frac{1}{2}a \cdot t_{\text{ob}}^2 \quad (5.31)$$

where  $t_{\text{ob}}$  is the time needed for the hyperloop to reach the observation. The velocity of the hyperloop at the observation point is simply

$$V_{\text{ob}} = V_0 + a \cdot t_{\text{ob}} \quad (5.32)$$

### 5.3.3.2 Numerical results

#### Single observer



(a)

Figure 5.16: Time domain response of vertical displacement at tunnel invert due to an accelerating hyperloop

Figure 5.16 shows the effect of different acceleration values on the response at the fixed observation. The tunnel is modeled using solid elements. Note that the time domain signal has been shifted such that  $t = 0$  corresponds to the time instant when the hyperloop exactly passes the observation. Acceleration value  $a = 0$  corresponds to the constant moving load case, meaning that the velocity of the hyperloop is 30 m/s throughout the path.  $a = 0.5 \times g$  corresponds to the velocity at the observation  $V_{ob} = 62\text{m/s}$  and  $a = 2 \times g$  corresponds to the velocity at the observation  $V_{ob} = 98.6\text{m/s}$ .

The waves in front of the hyperloop are different for different accelerations. The increase in acceleration will lead to more compressed waves ahead of the hyperloop. The time duration of the response will be less and the peaks become more steep. More importantly, for  $a = 2 \times g$ , the maximum displacement is smaller than the others. This is because the hyperloop has reached the critical velocity before it actually arrives at the observation point. And we know that the maximum displacement in the tunnel invert corresponds to the Rayleigh wavespeed ( $V = 72\text{ m/s}$ ). Therefore, the maximum response happens at a place in front of the observation point. Responses at other speeds are not as large as at Rayleigh wavespeed, referring to fig.5.14.

To further investigate the effect of acceleration values on the maximum displacement response at the tunnel invert, figure 5.17(a) shows the maximum displacements taken from the peak values as shown in figure 5.14 for acceleration values 0 -  $5 \times g$ . Too large accelerations are not realistic but clearly show the effect of varying accelerations.

Judging from 5.17(a), for  $a < 1.2 \times g$ , the peak values will increase with the increase in acceleration. For larger accelerations  $a > 1.2 \times g$ , a further increase in acceleration will lead to a decrease in the maximum displacement. The most critical scenario is when the hyperloop has a relatively small acceleration ( $a = 1.2 \times g$ ), meaning that it passes the Rayleigh wave speed slowly.

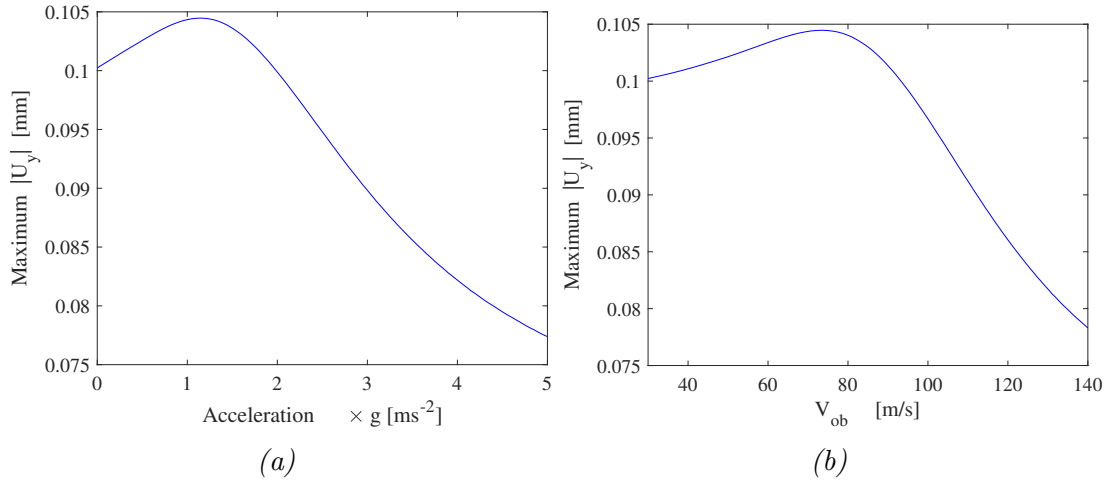


Figure 5.17: Maximum response of displacement at the tunnel invert (a) with varying acceleration and (b) the corresponding velocity at the observation

The reason behind is that for a fixed observation, a hyperloop with a sufficiently large acceleration has reached the critical speed (Rayleigh wave speed in the soil) before it reaches the observation. Figure 5.17(b) shows the corresponding velocity at the observation point. For example,  $V_{ob}$  in figure 5.17(b) corresponds to  $a = 0$  in figure 5.17(a). The maximum displacement in the accelerating case occurs at around the Rayleigh wave speed in the soil (72 m/s), which coincides with the constant moving load case.

### Multiple observers

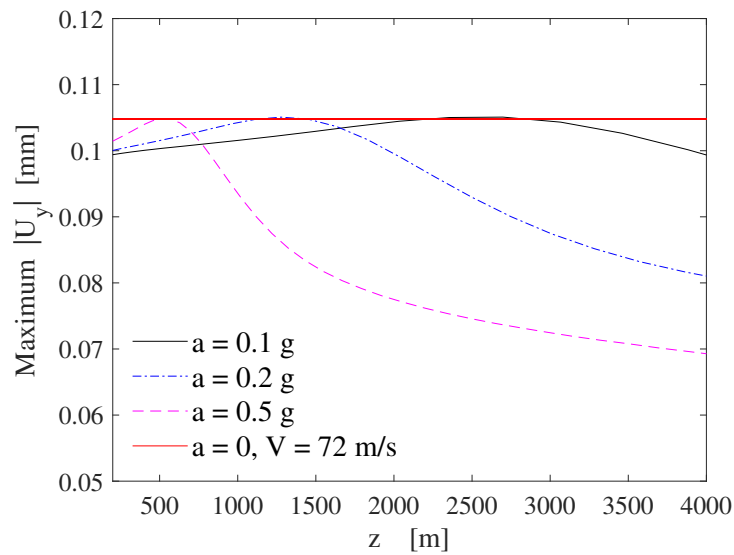
Instead of having one observation present in the middle of the tunnel axis, in this section, multiple observations are present along the path. In this way, the maximum response can be captured at other positions. An hyperloop with an initial velocity  $V = 0$  starts to accelerate from location  $z = 0$  at time instant  $t = 0$ .

Multiple observations are placed on the path. At each of the observation, a time domain response like the one in figure 5.16 will be observed and the maximum value is recorded. Figure 5.18 shows the maximum vertical displacement at tunnel invert due to an accelerating hyperloop. The maximum responses are calculated for acceleration values 0.1g, 0.2g and 0.5g. In figure 5.18, the maximum response caused by a hyperloop traveling at the critical speed (Rayleigh wavespeed) is also shown. It is a horizontal line because the hyperloop moves at a constant speed. Responses are everywhere the same in the observations along the path, but with a time delay.

It can be seen that with a smaller acceleration value, the maximum displacement

caused by the hyperloop lasts for a longer time because the hyperloop is slowly accelerating, and slowly passing the critical speed (Rayleigh wavespeed). The maximum response in the figure corresponds to the critical speed  $V = 72\text{m/s}$  found in FEM model, referring to figure 5.14.

Moreover, the maximum response caused by the accelerating hyperloop does not exceed the maximum response caused by hyperloop traveling at the critical speed (Rayleigh wavespeed). This is because the effect of the hyperloop breaking the Rayleigh wave barrier is transient. The most threatening moment is when the hyperloop travels at the critical speed. The time duration of accelerating and passes the Rayleigh wave speed is short. We conclude that the case where a hyperloop runs at the critical speed is more crucial than the case where a hyperloop accelerates and passes the Rayleigh wavespeed.



(a)

Figure 5.18: Maximum vertical displacement at tunnel invert due to an accelerating hyperloop

## 5.4 Summary

In this chapter, a FEM model is established for analysing the hyperloop problem. A moving load is modelled as a series of consecutive short pulses. Response due to a moving load is obtained by the convolution of impulses response. Therefore, in the FEM model, a concrete tunnel embedded in a half-space is subjected to a stationary impulse load. The distribution of the load is the same as that in the BEM model for the purpose of comparison. Then, the response of the half-space due to a moving load (hyperloop) is obtained by convoluting the impulse responses. The convolution relies on the invariant space in the direction parallel to the tunnel axis.

The convergence of the convolution is ensured by choosing proper parameters which are investigated in chapter 5. Different element types in modeling the tunnel are investigated: solid elements and shell elements. The dynamic behavior of the solid elements and shell elements is found to be distinctive. It is found out that an accurate description of the impulses response is difficult when shell elements are used to model the tunnel.

For comparison with the BEM model, velocity and displacement responses are calculated by the FEM model, using both solid elements and shell elements. Results calculated by all the models are shown to have good agreements with the maximum difference no larger than 20 %. The FEM model has difficulties in the convergence of the impulse response, which can result in an inaccuracy in the response due to very high hyperloop speeds. The convergence of the impulse response can be mitigated by using a very small element size (e.g.,  $L_e < 0.5\text{m}$ ).

Critical velocities are found by considering the maximum responses versus varying hyperloop speeds. An important finding of the current thesis is that the Rayleigh wave speed in the soil is not the only critical velocity which can be seen from figure 5.11. For the hyperloop moving in the tunnel surrounded by soil, a second critical velocity is found which is related to the wave propagation in the tunnel. The second critical velocity is found to be around 600m/s for the current study, which cannot be reached by the hyperloop in reality. Before the hyperloop reaches the second critical velocity, the maximum velocity response on the ground surface keeps increasing with the increase in the hyperloop speed.

Furthermore, by applying the convolution, the response of the system due to an accelerating hyperloop is also investigated. The moment when the hyperloop accelerates and passes the Rayleigh wave speed is considered. The displacements at the tunnel invert are calculated by using different accelerations. The responses due to accelerating hyperloops are not as large as that caused by a hyperloop running constantly at the Rayleigh wave speed in the soil.





# Chapter 6

## Discussions and Conclusions

### 6.1 Result discussions

The dynamic responses at tunnel invert and those on the ground surface due to a hyperloop pod moving in the tunnel have been investigated. The ground is modeled as a three dimensional linear elastic half-space, and the tunnel is modeled to be infinitely long and buried underground. Two methods have been applied to study the phenomena, namely, the indirect boundary element method and the finite element method. In the BEM, the half-space is modeled by elastic continuum and the tunnel is modeled as an infinitely long thin shell, respectively. The hyperloop pod is considered as a constant moving load, acting in the radial direction and uniformly distributed at the lower part of the tunnel. In the FEM, both the ground and the tunnel are modeled as multiple-degree-of-freedom systems (MDOF). The moving load is considered to have the same profile, and is modeled as a series of consecutive short pulses whose responses are later synthesized by means of convolution.

There are two main objectives of the current thesis work:

1. Investigating the dynamic response of the system which consists of a half-space with an embedded tunnel, due to the excitation of a hyperloop;
2. Making a comparison between the boundary element method and the finite element method, in terms of result accuracy and calculation time.

The following research questions have been formed in the introduction part of this thesis:

- (1) what are the dynamic responses of the tunnel and in the ground, especially in the critical cases?
- (2) What are the factors which can influence the responses?
- (3) Which scenario is more crucial, a hyperloop travelling at critical speeds, or a hyperloop that accelerates and breaks the elastic wave barrier?
- (4) What are the performances of the boundary element method and the finite element method?

Each of these questions and its corresponding answers are discussed in this section.

**(1) what are the dynamic responses of the tunnel, especially in the critical cases?**

The term *critical cases* refers to the scenario where the hyperloop is traveling at a speed which causes the maximum response, while at other speeds the response is smaller. For the case study in the thesis, 2 critical velocities are found where maximum responses are observed. The first critical velocity is the Rayleigh wavespeed ( $V = 72\text{m/s}$ ) in the soil, which is related to the resonance of the soil. The second critical velocity is related to the wave propagation in the tunnel (around  $V = 600\text{m/s}$ ).

At the first critical velocity  $V = 72\text{m/s}$ , the amplitude spectra of the vertical displacement at the position of tunnel invert have the main part of energy around zero frequency because of the constant moving load. Amplitude spectra of velocity response at the tunnel invert have wider frequency bands. For the hyperloop speed  $V > 72\text{m/s}$ , waves with higher frequency are generated. The interference of waves between the tunnel and the free surface becomes much more intensive, which can be observed from the response spectra in figure 4.14. Moreover, strong wave radiation effect is observed from the time domain plots of the velocity response in figure 5.9.

The velocity response at the free surface keeps increasing until the hyperloop reaches the second critical speed ( $V = 600\text{m/s}$ ). At hyperloop speed  $V = 300\text{m/s}$ , the maximum velocity on the surface can be as high as  $0.5\text{ mm/s}$ , and at the tunnel invert it can reach  $10\text{ mm/s}$ . Velocity level exceeding  $0.1\text{ mm/s}$  is perceivable to humans. The maximum displacement at the tunnel invert is found to be  $0.12\text{ mm}$ . And the maximum tensile stress at the tunnel invert is less than  $0.2\text{ MPa}$  for the current case study. It is therefore concluded that the deformation caused by the hyperloop is acceptable, however, the velocity response is severe, especially in the tunnel.

**(2) What are the factors which can influence the responses?**

The critical velocities are influenced by the material properties of the soil and those of the tunnel: the elastic modulus, the density, the Poisson's ratio. Also, the thickness of the tunnel and the moving load distribution pattern are of concern. Moreover, the damping in the materials has an influence on the response amplitudes.

In Chapter 4, a parametric study has been carried out to study the effect of hyperloop speed, the effect of tunnel depth and the effect of lining thickness on the dynamic response of the system.

Firstly, the hyperloop speed has the largest influence on the dynamic response of the system. Wave patterns and the amplitudes are related to the hyperloop speed to a large extent. The amplitudes of displacements increase with the increase in the hyperloop speed until the hyperloop reaches the critical speed (Rayleigh wave speed). In the tunnel and at the surface, waves with high frequency content are activated when the hyperloop is traveling at high speeds. The velocity keeps increasing with the increase in hyperloop speeds until the second critical velocity is reached ( $V = 600\text{ m/s}$ ). Moreover, the hoop stress and longitudinal stress in the tunnel are not influenced too much by the hyperloop speed.

Secondly, it is found that the increase in the tunnel depth can effectively reduce the vibration level in the ground and in the tunnel. Because a deep tunnel means a larger

distance between the ground surface and the tunnel. Reflected waves from the surface are damped out before they reach the tunnel. In other words, the wave interference is weaker for deep tunnels.

Thirdly, the thickness of the tunnel wall influences the dynamic behavior in a structural way. A reduction in the cross-section area results in a larger stress. In the meantime, the deformation increases because the stiffness of the tunnel is less. For a thick concrete lining, the vibration level both in the ground and in the tunnel is reduced because of a larger stiffness of the tunnel.

**(3) Which scenario is more crucial, a hyperloop travelling at critical speeds, or a hyperloop that accelerates and breaks the elastic wave barrier**

The elastic wave barrier here refers to the Rayleigh wave barrier. The case that a hyperloop accelerates and passes the Rayleigh wavespeed cannot be more crucial than a hyperloop running constantly at the critical speed  $V = 72$  m/s. At first sight, there are more condensed waves in front of the hyperloop when the hyperloop is accelerating, compared to a constantly moving hyperloop. It might seem logical that an accelerating hyperloop can cause more vibration than a constantly moving hyperloop. However, since the hyperloop speed is changing during the process, the most threatening scenario only lasts for a short period. Once the hyperloop has exceeded the critical speed (Rayleigh wavespeed), the response becomes smaller. On the other hand, for a hyperloop running at the critical speed  $V = 72$  m/s, it constantly gives the most threat. This is the reason why the influence brought by an accelerating hyperloop is transient and cannot be more crucial than a hyperloop constantly running at the critical speed ( $V = 72$  m/s).

**(4) What are the performances of the boundary element method and the finite element method?**

**BEM**

The accuracy of the boundary element method depends on the convergences to an large extent: the convergence of the model which is influenced mainly by the location and the number of sources and receivers; the convergence of the used 2.5D Green's functions where the wavenumber discretization is important; and also the convergence of the shell modes.

The accuracy of the method has been verified by intense case studies. An improvement in the convergence has been made in evaluating the Green's functions surface-related terms. In this way, the boundary integrals can satisfy the boundary conditions better than before. As a consequence, the accuracy of the boundary element method is improved. It is also found that the results are more accurate in the near field of the sources, than in the far field. More importantly, there are no one-for-all models. In case of high frequency excitation, the accuracy is bad if too few number of sources and observations are used, because the limited amount of sources and observations are not enough to describe the dynamic behavior. In this case, more modes of the shell should also be included.

The calculation time is also related to many aspects. The main effort in calculation lies in the numerical evaluation of the Green's functions, especially the surface-related terms.

Since these surface-related terms are approximated using a sufficiently large number of wavenumbers, the discretization decides the time costs. In the calculation, the discretization process is automatically taken into account by using the Gauss-kronrod quadrature numerical integration. Using the full-space approximation where these surface-related Green's functions are left out can reduce a large amount of computational time.

The second main influencing factor is the number of sources and observations, because the Green's functions are calculated for each pair of source and observation. Using more observations and sources can guarantee the accuracy of the results, but increase the time cost on the other hand. The calculation time has been reduced to a half by using half number of the sources.

Moreover, if the time domain response is of interest, the calculation time also depends on the frequency step size and the truncated frequency. The current thesis is carried out using an Intel(R) Core(TM)i7-4810MQ 2.80GHz CPU processor. In the current study, where 20 sources and 40 observations are used, 35 seconds are needed on average to calculate for each frequency. If 40 sources and 80 observations are used, 300 seconds are needed on average to calculate for each frequency. If a 0.1 Hz step size up to 20 Hz are considered, the calculation takes about 16 hours when using the half-space Green's functions. For the same case, the calculation only takes 20 minutes when using the full-space approximation.

## FEM

The results obtained by the FEM have been compared to those by the BEM. Differences and similarities are observed. In general, the FEM model is able to describe the dynamic behaviors of the system but with a maximum 20 % difference when compared to the results from the BEM.

The accuracy of the FEM model depends mainly on two aspects, the convergence of the impulse response, and the convergence of the convolution integral. The convergence of the impulse response is difficult because high frequency waves up to 200 Hz are generated near the stationary impulse loading position. It is difficult to accurately describe these waves, unless very fine elements are used. In the current case study, 0.2 m element size is the minimum element size which gives an acceptable computation cost. It is found out that obtaining accurate impulse responses using shell elements is more difficult than using solid elements.

The influencing parameters on the convergence of the convolution has been discussed using a sensitivity study in Chapter 5. It is concluded that by applying the convolution rule, the results are sensitive to the parameters chosen: element size, model size, length of time response histories and time step size in the histories.

The differences between the results from the two models may come from:

- The convergence problem of the impulse response, which can be mitigated by using even smaller element sizes;
- Element types used in the FEM model. It has been proven that using the shell elements in the FEM model, the displacement response is more similar to that of the BEM, compared to using solid elements;

In terms of calculation time, it takes 12 hours to calculate a FEM model with a 200 m length and an 0.5 m element size in the longitudinal direction, with a total record time 2 seconds and a time step 0.001 s. However, the calculation time can be reduced

by choosing proper values of the parameters discussed in Chapter 5, provided that the convergence of the convolution is met.

## 6.2 Limitations

In the process of establishing these models, concessions and assumptions have been made because of the research scope, restrictions regarding the computational costs, or the compliance with the theories. It is important to keep in mind the limitations in using these models:

- The form of loading in the BEM. A static loading is not possible because of the singularity problem of Green's functions at frequency  $f = 0\text{Hz}$ ; Also, although an external loading on the ground surface is possible, the half-space Green's functions should consider the traction equilibrium at the surface;
- The BEM model is not able to produce response of the system due to an accelerating hyperloop running in the tunnel, or any other transient excitation;

## 6.3 Future recommendations

- The convergence of the models can be further improved. In the FEM, to ensure the accuracy of results for high hyperloop speeds, the convergence of the impulse response should be improved. To do so, even smaller element sizes can be used ( $L_e < 0.5\text{ m}$ ), which will result in a large amount of computational time; In the BEM, to calculate cases for extremely high hyperloop speeds, the number of observations and sources should be increased, and more importantly, the frequency spectrum should be extended to a truncated frequency (up to 500 Hz or even higher) where all the energy is included. Of course, the frequency step size should be small in order to have an appropriate time window;
- The modeling of multiple layers of soil. To do so, the original Green's functions for a homogeneous half-space are not applicable any more, and a completely different set of Green's functions should be applied. The new set of Green's functions should take into account the displacement and stress continuity conditions at the interfaces between adjacent soil layers. Furthermore, the coupling equations for the shell and the layered half-space will become much more complicated;
- A more realistic model of the hyperloop pod can be coupled with the indirect BEM, where the stability analysis of the pod itself can be carried out.



# Bibliography

- [1] Elon Musk. Hyperloop alpha. (*PDF*). *SpaceX*. Retrieved August, 13.
- [2] Yao Kun, Yu Hao-wei, and Wei Dong. Research development of subway vibration impact on environment.
- [3] JA Forrest and HEM Hunt. A three-dimensional tunnel model for calculation of train-induced ground vibration. *Journal of sound and vibration*, 294(4-5):678–705, 2006.
- [4] Christoph Heinemeyer and Markus Feldmann. European design guide for footbridge vibration. In *Footbridge vibration design*, pages 13–30. CRC Press, 2009.
- [5] James T Nelson, Hugh J Saurenman, Ihrig Wilson, et al. State-of-the-art review: prediction and control of groundborne noise and vibration from rail transit trains. Technical report, United States. Urban Mass Transportation Administration, 1983.
- [6] R Paolucci, A Maffei, L Scandella, M Stupazzini, and M Vanini. Numerical prediction of low-frequency ground vibrations induced by high-speed trains at ledsgaard, sweden. *Soil Dynamics and Earthquake Engineering*, 23(6):425–433, 2003.
- [7] W Gardien and HG Stuit. Modelling of soil vibrations from railway tunnels. *Journal of Sound and Vibration*, 267(3):605–619, 2003.
- [8] AA Stamos and DE Beskos. 3-d seismic response analysis of long lined tunnels in half-space. *Soil Dynamics and Earthquake Engineering*, 15(2):111–118, 1996.
- [9] FCP De Barros and JE Luco. Response of a layered viscoelastic half-space to a moving point load. *Wave motion*, 19(2):189–210, 1994.
- [10] FCP De Barros and JE Luco. Diffraction of obliquely incident waves by a cylindrical cavity embedded in a layered viscoelastic half-space. *Soil Dynamics and Earthquake Engineering*, 12(3):159–171, 1993.
- [11] Francisco CP de Barros and J Enrique Luco. Amplification of obliquely incident waves by a cylindrical valley embedded in a layered half-space. *Soil Dynamics and Earthquake Engineering*, 14(3):163–175, 1995.
- [12] Luco JE, HL Wong, and FCP De Barros. Three-dimensional response of a cylindrical canyon in a layered half-space. *Earthquake Engineering & Structural Dynamics*, 19(6):799–817, 1990.
- [13] Tadeu AJB and Kausel Eduardo. Green’s functions for two-and-a-half-dimensional elastodynamic problems. *Journal of Engineering Mechanics*, 126(10):1093–1097, 2000.
- [14] Michel Bouchon. Discrete wave number representation of elastic wave fields in three-space dimensions. *Journal of Geophysical Research: Solid Earth*, 84(B7):3609–3614, 1979.
- [15] A Tadeu, J António, and L Godinho. Green’s function for two-and-a-half dimensional elastodynamic problems in a half-space. *Computational mechanics*, 27(6):484–491, 2001.

- [16] Arthur W Leissa. *Vibration of shells*, volume 288. Scientific and Technical Information Office, National Aeronautics and Space Administration Washington, 1973.
- [17] Lloyd Hamilton Donnell. Stability of thin-walled tubes under torsion. 1935.
- [18] JE Luco and FCP De Barros. Seismic response of a cylindrical shell embedded in a layered viscoelastic half-space. i: Formulation. *Earthquake engineering & structural dynamics*, 23(5):553–567, 1994.
- [19] JE Luco and FCP De Barros. Dynamic displacements and stresses in the vicinity of a cylindrical cavity embedded in a half-space. *Earthquake engineering & structural dynamics*, 23(3):321–340, 1994.
- [20] Mingjuan Zhao, Karel N van Dalen, João M Barbosa, and Andrei V Metrikine. Semi-analytical solution for the dynamic response of a cylindrical structure embedded in a homogeneous half-space. In *International Symposium on Environmental Vibration and Transportation Geodynamics*, pages 369–388. Springer, 2016.
- [21] AV Metrikine and ACWM Vrouwenvelder. Surface ground vibration due to a moving train in a tunnel: two-dimensional model. *Journal of Sound and vibration*, 234(1):43–66, 2000.
- [22] Zonghao Yuan, Anders Boström, and Yuanqiang Cai. Benchmark solution for vibrations from a moving point source in a tunnel embedded in a half-space. *Journal of Sound and Vibration*, 387:177–193, 2017.
- [23] HERKE G STUIT. Experiences in wave propagation and vibration by moving loads. *Learned and Applied Soil Mechanics: A tribute to Dr Arnold Verruijt, TUD*, page 161, 2002.
- [24] SD Akbarov and AN Guz. Axisymmetric longitudinal wave propagation in prestressed compound circular cylinders. *International Journal of Engineering Science*, 42(8-9):769–791, 2004.





# Appendices



# Appendix A

## 2.5D Green's functions for a half-space

The purpose of this section is to provide the full set of the 2.5D Green's functions based on the work of A.Tadeu et al [13][15], which are used throughout the thesis. Displacements in  $x$ ,  $y$  and  $z$  direction due to loads having the form  $p(x, y, z, t) = \delta(x)\delta(y)e^{i(\omega t - k_z z)}$  acting in  $x$ ,  $y$  and  $z$  direction are given. Stresses and strains are derived by the well-known constitutive equations, taking the derivatives of the displacements. The 2.5D Green's functions consist of 2 parts, the full-space terms and the surface-related terms, which are given in the following.

### A.1 Full-space terms

#### A.1.1 Displacements

$$G_{xx}^{\text{full}} = \frac{1}{4i\rho\omega^2} \left[ k_s^2 H_{0\beta} - \frac{1}{r} B_1 + \left( \frac{x - x_0}{r} \right)^2 B_2 \right] \quad (\text{A.1a})$$

$$G_{yy}^{\text{full}} = \frac{1}{4i\rho\omega^2} \left[ k_s^2 H_{0\beta} - \frac{1}{r} B_1 + \left( \frac{y - y_0}{r} \right)^2 B_2 \right] \quad (\text{A.1b})$$

$$G_{zz}^{\text{full}} = \frac{1}{4i\rho\omega^2} [k_s^2 H_{0\beta} - k_z^2 B_0] \quad (\text{A.1c})$$

$$G_{xy}^{\text{full}} = G_{yx}^{\text{full}} = \frac{1}{4i\rho\omega^2} \left( \frac{x - x_0}{r} \right) \left( \frac{y - y_0}{r} \right) B_2 \quad (\text{A.1d})$$

$$G_{xz}^{\text{full}} = G_{zx}^{\text{full}} = \frac{k_z}{4\rho\omega^2} \left( \frac{x - x_0}{r} \right) B_1 \quad (\text{A.1e})$$

$$G_{yz}^{\text{full}} = G_{zy}^{\text{full}} = \frac{k_z}{4\rho\omega^2} \left( \frac{y - y_0}{r} \right) B_1 \quad (\text{A.1f})$$

### A.1.2 Strains and stresses

$$\epsilon_{ij}^l = \frac{1}{2} (G_{il,j} + G_{jl,i}) \quad (\text{A.2a})$$

$$\sigma_{ij}^l = \lambda \epsilon_{\text{vol}}^l \delta_{ij} + 2\mu \epsilon_{ij}^l \quad (\text{A.2b})$$

where  $i, j = x, y, z$  denote the components while  $l$  denotes the direction of the loading. Here, strains components follow from the convention used in mechanics. For convenience, amplitude  $A = \frac{1}{4i\rho\omega^2}$ ;  $\gamma_x = \frac{x - x_0}{r}$ ,  $\gamma_y = \frac{y - y_0}{r}$ .

#### Strains for loads acting in plane ( $l = x, y$ )

$$\epsilon_{\text{vol}}^l = \gamma_l A \left( -k_s^2 k_\beta H_{1\beta} + k_z^2 B_1 + \frac{4}{r} B_2 - B_3 \right) \quad (\text{A.3a})$$

$$\epsilon_{xx}^l = \gamma_l A \left( \left( \frac{2}{r} B_2 - k_s^2 k_\beta H_{1\beta} \right) \delta_{xl} + \frac{1}{r} B_2 - \gamma_x^2 B_3 \right) \quad (\text{A.3b})$$

$$\epsilon_{yy}^l = \gamma_l A \left( \left( \frac{2}{r} B_2 - k_s^2 k_\beta H_{1\beta} \right) \delta_{yl} + \frac{1}{r} B_2 - \gamma_y^2 B_3 \right) \quad (\text{A.3c})$$

$$\epsilon_{zz}^l = \gamma_l k_z^2 A B_1 \quad (\text{A.3d})$$

$$\epsilon_{xy}^l = A \left( \left( \frac{1}{r} B_2 - \frac{1}{2} k_s^2 k_\beta H_{1\beta} \right) (\delta_{xl} \gamma_y + \delta_{yl} \gamma_x) - \gamma_x \gamma_y \gamma_l B_3 \right) \quad (\text{A.3e})$$

$$\epsilon_{xz}^l = i k_z A \left( \left( \frac{1}{r} B_1 - \frac{1}{2} k_s^2 H_{0\beta} \right) \delta_{xl} - \gamma_x \gamma_l B_2 \right) \quad (\text{A.3f})$$

$$\epsilon_{yz}^l = i k_z A \left( \left( \frac{1}{r} B_1 - \frac{1}{2} k_s^2 H_{0\beta} \right) \delta_{yl} - \gamma_y \gamma_l B_2 \right) \quad (\text{A.3g})$$

#### Strains for loads acting out of plane ( $l = z$ )

$$\epsilon_{\text{vol}}^z = i k_z A \left( -k_s^2 H_{0\beta} + k_z^2 B_0 + k_z^2 B_0 + \frac{2}{r} B_1 - B_2 \right) \quad (\text{A.4a})$$

$$\epsilon_{xx}^z = i k_z A \left( \frac{1}{r} B_1 - \gamma_x^2 B_2 \right) \quad (\text{A.4b})$$

$$\epsilon_{yy}^z = i k_z A \left( \frac{1}{r} B_1 - \gamma_y^2 B_2 \right) \quad (\text{A.4c})$$

$$\epsilon_{zz}^z = i k_z A (-k_s^2 H_{0\beta} + k_z^2 B_0) \quad (\text{A.4d})$$

$$\epsilon_{xy}^z = -i k_z \gamma_x \gamma_y A B_2 \quad (\text{A.4e})$$

$$\epsilon_{xz}^z = \gamma_x A \left( -\frac{1}{2} k_s^2 k_\beta H_{1\beta} + k_z^2 B_1 \right) \quad (\text{A.4f})$$

$$\epsilon_{yz}^z = \gamma_y A \left( -\frac{1}{2} k_s^2 k_\beta H_{1\beta} + k_z^2 B_1 \right) \quad (\text{A.4g})$$

## A.2 Surface terms

$$E_b = e^{-ik_{py}|y-y_0|} \quad (\text{A.5a})$$

$$E_c = e^{-ik_{sy}|y-y_0|} \quad (\text{A.5b})$$

$$E_{b0} = e^{-ik_{py}y} \quad (\text{A.5c})$$

$$E_{c0} = e^{-ik_{sy}y} \quad (\text{A.5d})$$

$$E_{b1} = e^{-ik_{py}y_0} \quad (\text{A.5e})$$

$$E_{c1} = e^{-ik_{sy}y_0} \quad (\text{A.5f})$$

Load acting in the  $x$  direction,

$$G_{xx}^{\text{half}} = G_{xx}^{\text{full}} + E_a \int_{-\infty}^{+\infty} \left( A^x \frac{-ik_x^2}{k_{py}} E_{b0} + \left( -ik_{sy} C^x - \frac{ik_z^2}{k_{sy}} B^x \right) E_{c0} \right) e^{-ik_x(x-x_0)} dk_x \quad (\text{A.6a})$$

$$G_{yx}^{\text{half}} = G_{yx}^{\text{full}} + E_a \int_{-\infty}^{+\infty} (-ik_x A^x E_{b0} + ik_x C^x E_{c0}) e^{-ik_x(x-x_0)} dk_x \quad (\text{A.6b})$$

$$G_{zx}^{\text{half}} = G_{zx}^{\text{full}} + E_a \int_{-\infty}^{+\infty} \left( \frac{-ik_z k_n}{k_{py}} A^x E_{b0} + \frac{ik_z k_n}{k_{sy}} B^x E_{c0} \right) e^{-ik_x(x-x_0)} dk_x \quad (\text{A.6c})$$

$$\begin{bmatrix} -2k_x^2 & -k_z^2 & k_x^2 - k_{sy}^2 \\ -2 & 1 & 1 \\ \frac{-k_s^2}{k_{py}} + \frac{2k_{\text{hor}}^2}{k_{py}} & 0 & 2k_{sy} \end{bmatrix} \times \begin{bmatrix} A^x \\ B^x \\ C^x \end{bmatrix} = \begin{bmatrix} -2k_x^2 E_{b1} + (-k_s^2 + 2k_x^2) E_{c1} \\ -2E_{b1} + 2E_{c1} \\ \left( \frac{k_s^2}{k_{py}} - \frac{2k_{\text{hor}}^2}{k_{py}} \right) E_{b1} - 2k_{sy} E_{c1} \end{bmatrix} \quad (\text{A.7})$$

Load acting in the  $y$  direction,

$$G_{xy}^{\text{half}} = G_{xy}^{\text{full}} + E_a \int_{-\infty}^{+\infty} (-iA^y k_x E_{b0} + iB^y k_x E_{c0}) e^{-ik_x(x-x_0)} dk_x \quad (\text{A.8a})$$

$$G_{yy}^{\text{half}} = G_{yy}^{\text{full}} + E_a \int_{-\infty}^{+\infty} \left( -ik_{py} A^y E_{b0} + \left( \frac{-ik_x^2}{k_{sy}} B^y + \frac{-ik_z^2}{k_{sy}} C^y \right) E_{c0} \right) e^{-ik_x(x-x_0)} dk_x \quad (\text{A.8b})$$

$$G_{zy}^{\text{half}} = G_{zy}^{\text{full}} + E_a \int_{-\infty}^{+\infty} (-iA^y k_z E_{b0} + iC^y k_z E_{c0}) e^{-ik_x(x-x_0)} dk_x \quad (\text{A.8c})$$

where

$$\begin{bmatrix} -2k_{py} & \frac{-k_x^2}{k_{sy}} + k_{sy} & \frac{-k_z^2}{k_{sy}} \\ -2k_{py} & \frac{-k_x^2}{k_{sy}} & \frac{-k_z^2}{k_{sy}} + k_{sy} \\ -k_s^2 + 2k_{\text{hor}}^2 & -2k_x^2 & -2k_z^2 \end{bmatrix} \times \begin{bmatrix} A^y \\ B^y \\ C^y \end{bmatrix} = \begin{bmatrix} 2k_{py} E_{b1} + \left( -\frac{k_{\text{hor}}^2}{k_{sy}} + k_{sy} \right) E_{c1} \\ 2k_{py} E_{b1} + \left( -\frac{k_{\text{hor}}^2}{k_{sy}} + k_{sy} \right) E_{c1} \\ \left( -k_s^2 + 2k_{\text{hor}}^2 \right) E_{b1} - 2k_{\text{hor}}^2 E_{c1} \end{bmatrix} \quad (\text{A.9})$$

**Load acting in the  $z$  direction,**

$$G_{xz}^{\text{half}} = G_{xz}^{\text{full}} + E_a \int_{-\infty}^{+\infty} \left( \frac{-ik_z k_x}{k_{py}} A^z E_{b0} + \frac{ik_z k_x}{k_{sy}} C^z E_{c0} \right) e^{-ik_x(x-x_0)} dk_x \quad (\text{A.10a})$$

$$G_{yz}^{\text{half}} = G_{yz}^{\text{full}} + E_a \int_{-\infty}^{+\infty} (-ik_z A^z E_{b0} + iB^z k_z E_{c0}) e^{-ik_x(x-x_0)} dk_x \quad (\text{A.10b})$$

$$G_{zz}^{\text{half}} = G_{zz}^{\text{full}} + E_a \int_{-\infty}^{+\infty} \left( \frac{-ik_z^2}{k_{py}} A^z E_{b0} + \left( \frac{-ik_x^2}{k_{sy}} C^z - ik_{sy} B^z \right) E_{c0} \right) e^{-ik_x(x-x_0)} dk_x \quad (\text{A.10c})$$

where

$$\begin{bmatrix} -2 & 1 & 1 \\ -2k_z^2 & k_z^2 - k_{sy}^2 & -k_x^2 \\ -\left(\frac{k_s^2}{k_{py}} - \frac{2k_{\text{hor}}^2}{k_{py}}\right) & 2k_{sy} & 0 \end{bmatrix} \times \begin{bmatrix} A^z \\ B^z \\ C^z \end{bmatrix} = \begin{bmatrix} 2(-E_{b1} + E_{c1}) \\ -2k_z^2 E_{b1} + (k_z^2 - k_{sy}^2 - k_x^2) E_{c1} \\ \left(\frac{k_s^2}{k_{py}} - \frac{2k_{\text{hor}}^2}{k_{py}}\right) E_{b1} - 2k_{sy} E_{c1} \end{bmatrix} \quad (\text{A.11})$$

The displacements related to the surface terms are listed above. In order to describe the boundary value problem, stresses related to the surface terms should also be derived. Although stresses are derived using equation (A.2), the procedure is much more lengthy and tedious, and therefore not shown here.

# Appendix B

## Free field formulations under incident P waves

The purpose of this section is to provide the three dimensional pressure free wave field with explicit expressions from Zhao's work [20]. The decoupled wave potentials are firstly given, from which the displacement field and the stress field are derived.

Incident compressional waves are denoted as  $\phi_{\text{inc}}$ . The plane wave solutions for incident waves ( $\phi_{\text{inc}}$ ) and the primary reflected waves ( $\phi_{\text{ref}}, \psi_{\text{ref}}, \chi_{\text{ref}}$ ) are given as:

$$\phi_{\text{inc}} = \phi_0 \exp(-ik_x x - ik_z z - ik_{py} y) \quad (\text{B.1a})$$

$$\phi_{\text{ref}} = R_{11} \phi_0 \exp(-ik_x x - ik_z z + ik_{py} y) \quad (\text{B.1b})$$

$$\psi_{\text{ref}} = R_{21} \phi_0 \exp(-ik_x x - ik_z z + ik_{sy} y) \quad (\text{B.1c})$$

$$\chi_{\text{ref}} = R_{31} \phi_0 \exp(-ik_x x - ik_z z + ik_{sy} y) \quad (\text{B.1d})$$

Based on the dimensionless Helmholtz decomposition  $\mathbf{u} = \nabla\phi + \nabla \times \boldsymbol{\Psi}$ , displacement components can be expressed in terms of the 3 scalar potentials  $\phi$ ,  $\psi$  and  $\chi$ .

$$u_x = \frac{\partial\phi}{\partial x} + \frac{1}{k_s} \left( k_s^2 \chi + \frac{\partial^2 \chi}{\partial x^2} \right) \quad (\text{B.2a})$$

$$u_y = \frac{\partial\phi}{\partial y} + \frac{\partial\psi}{\partial z} + \frac{1}{k_s} \frac{\partial^2 \chi}{\partial x \partial y} \quad (\text{B.2b})$$

$$u_z = \frac{\partial\phi}{\partial z} - \frac{\partial\psi}{\partial y} + \frac{1}{k_s} \frac{\partial^2 \chi}{\partial x \partial z} \quad (\text{B.2c})$$

in which

$$R_{11} = \frac{\Delta_{11}}{\Delta_p}, R_{21} = \frac{\Delta_{21}}{\Delta_s}, R_{31} = \frac{\Delta_{31}}{\Delta_s} \quad (\text{B.3a})$$

$$\Delta_p = 4k_{py} k_{sy} k^2 + (2k^2 - k_s^2)^2 \quad (\text{B.3b})$$

$$\Delta_s = \frac{-4k^4 k_z^2}{k_s^2} - \frac{4k_{py} k_{sy} k^2 k_z^2}{k_s^2} + 4k_{py} k_{sy} k^2 + k^2(8k^2 - 4k_x^2) + k_s^2(k_x^2 - 5k^2) + k_s^4 \quad (\text{B.3c})$$

$$\Delta_{11} = 4k_{py} k_{sy} k^2 - (2k^2 - k_s^2)^2 \quad (\text{B.3d})$$

$$\Delta_{21} = 4k_{py} k_x (2k^2 - k_s^2) \quad (\text{B.3e})$$

$$\Delta_{31} = \frac{4ik_{py} k_{sy} k_z}{k_s (2k^2 - k_s^2)} \quad (\text{B.3f})$$



strains and stress can be calculated again using the well-known relation between displacement and strain, i.e.,

$$\epsilon_{ij} = \frac{1}{2} (G_{i,j} + G_{j,i}) \quad (\text{B.4a})$$

$$\sigma_{ij} = \lambda \epsilon_{\text{vol}} \delta_{ij} + 2\mu \epsilon_{ij} \quad (\text{B.4b})$$

Detailed expressions for strains and stresses are very lengthy and therefore omitted.

So far, the stresses related to the potentials can be calculated. However, at the cavity boundary  $r_1 = R_1$ , stresses are expressed in cylindrical coordinates. Therefore, a transformation of stresses from cartesian coordinates to cylindrical coordinates is needed. This can be done using the transform matrix (2.9).

# Appendix C

## Convergence tests

The purpose of this section is to provide a number of convergence tests for different frequencies and different hyperloop speeds. For a couple of scenarios, different number of observations are used and results are compared (Note the the number of sources is the half of observations). This section is provided as a supplement to show that responses are converged up to an extremely high hyperloop speed ( $V = 1000$  m/s).

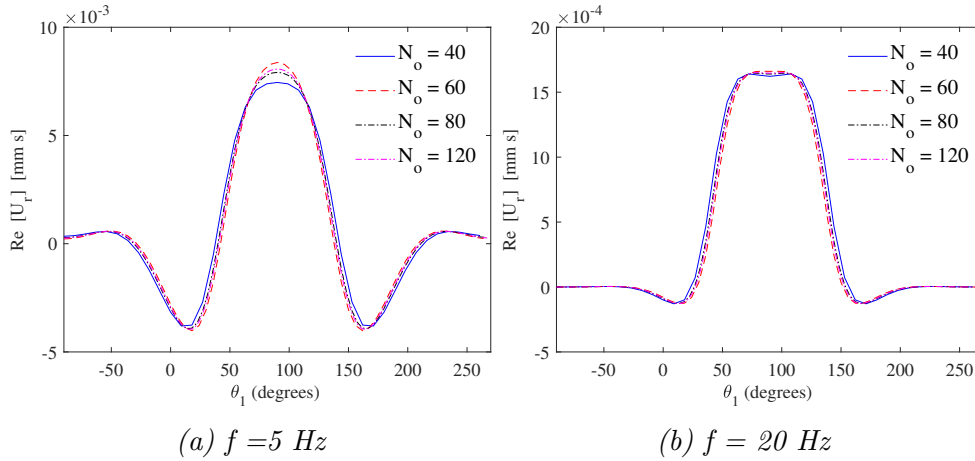


Figure C.1: Convergence tests for the real part of radial displacement ( $V = 50$  m/s)

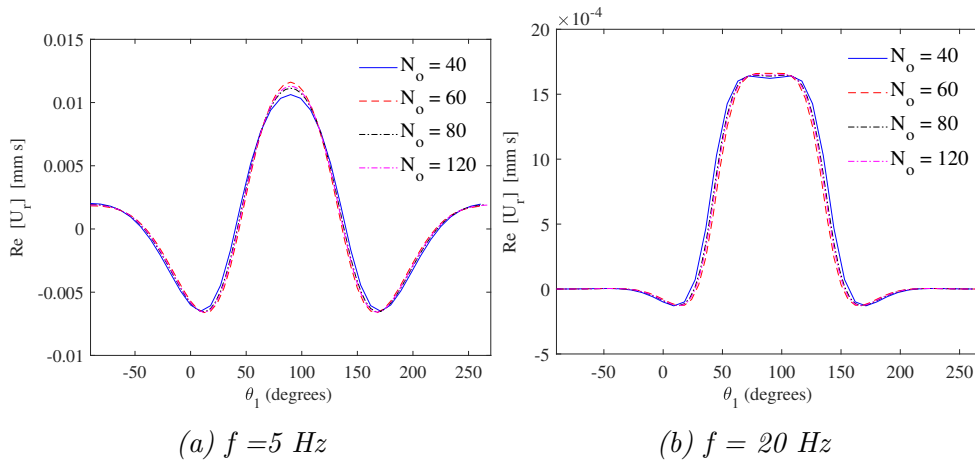


Figure C.2: Convergence tests for the real part of radial displacement ( $V = 75$  m/s)

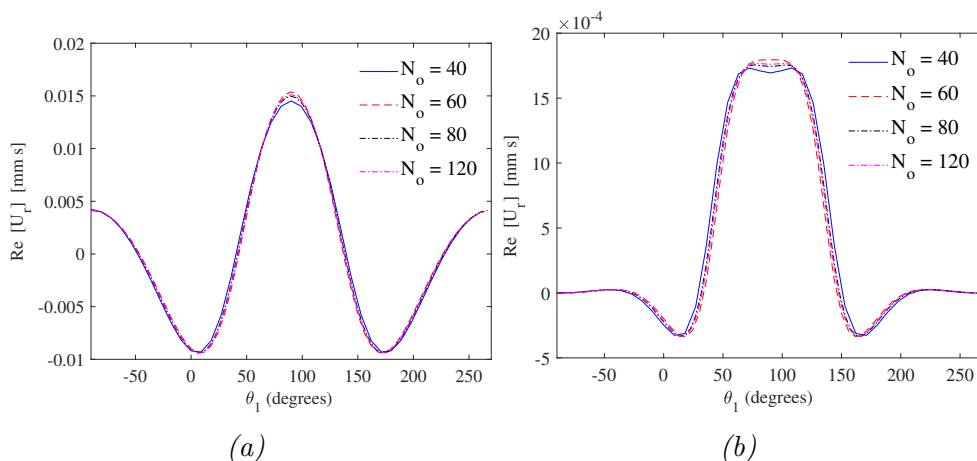


Figure C.3: Convergence tests for the real part of radial displacement frequency component ( $V = 100$  m/s) at frequencies: (a)  $f = 5$  Hz; (b)  $f = 20$  Hz

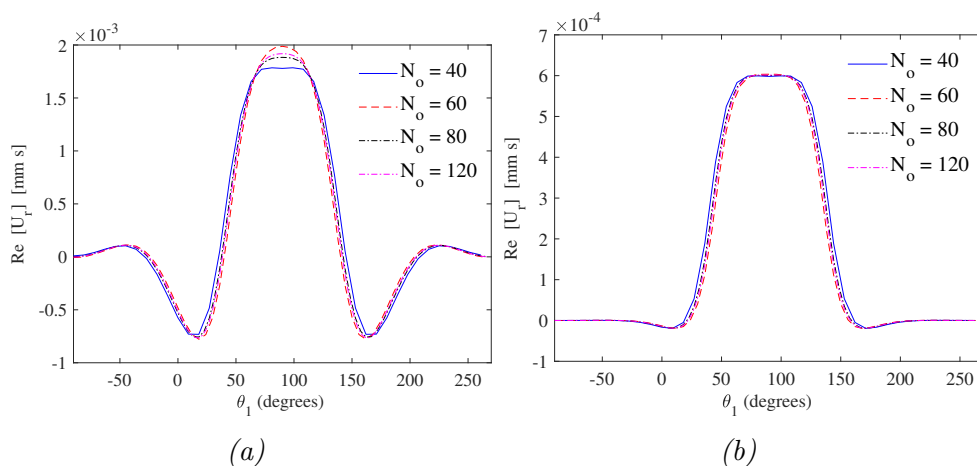


Figure C.4: Convergence tests for the real part of radial displacement frequency component ( $V = 150$  m/s) at frequencies: (a)  $f = 20$  Hz; (b)  $f = 50$  Hz

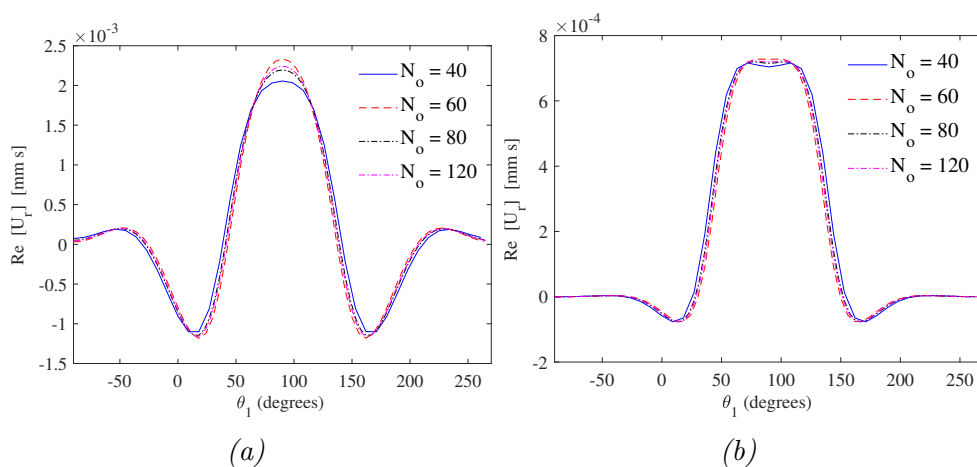


Figure C.5: Convergence tests for the real part of radial displacement frequency component ( $V = 200$  m/s) at frequencies: (a)  $f = 20$  Hz; (b)  $f = 50$  Hz

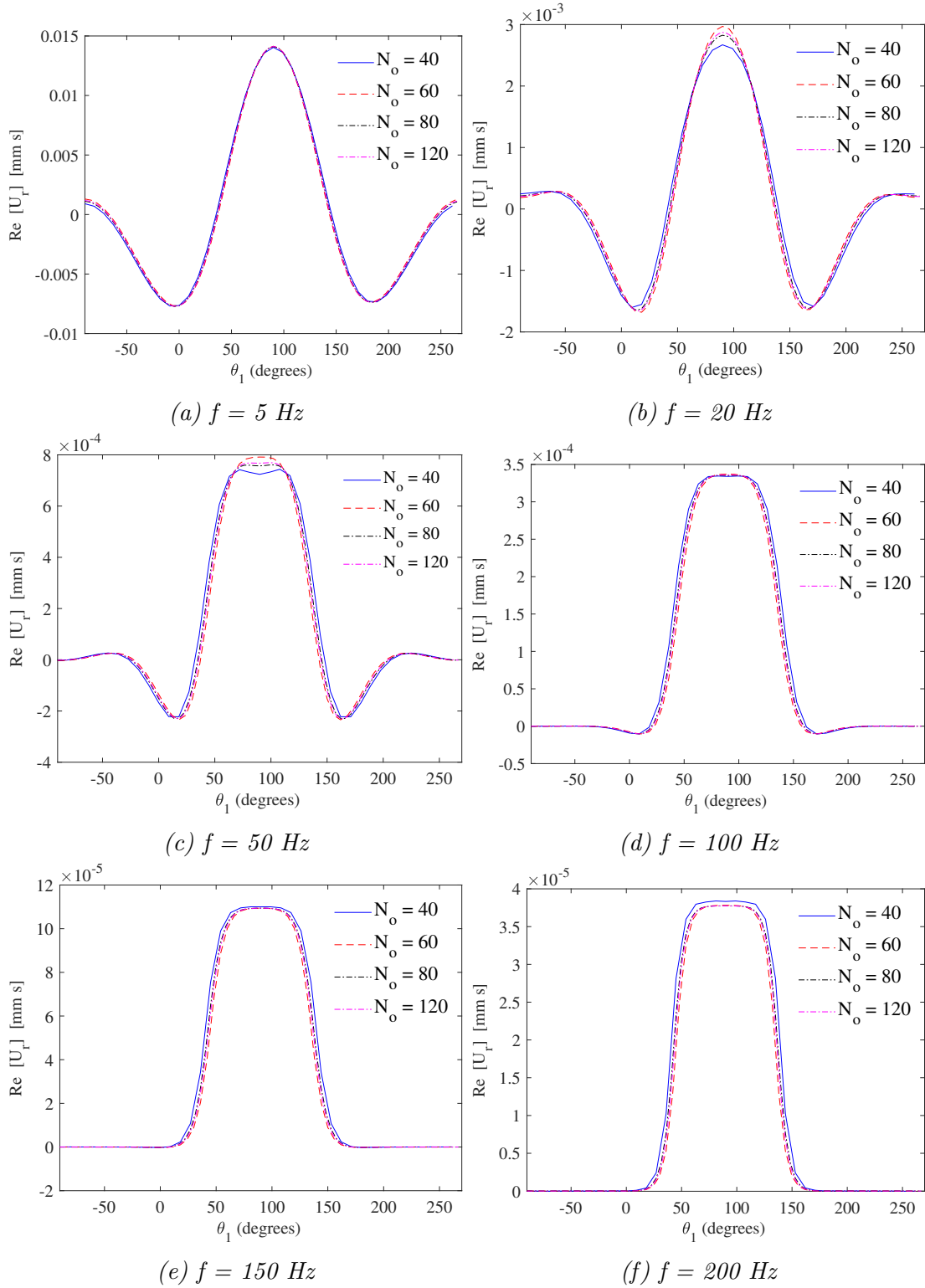


Figure C.6: Convergence tests for the real part of radial displacement frequency component at  $V = 300 \text{ m/s}$

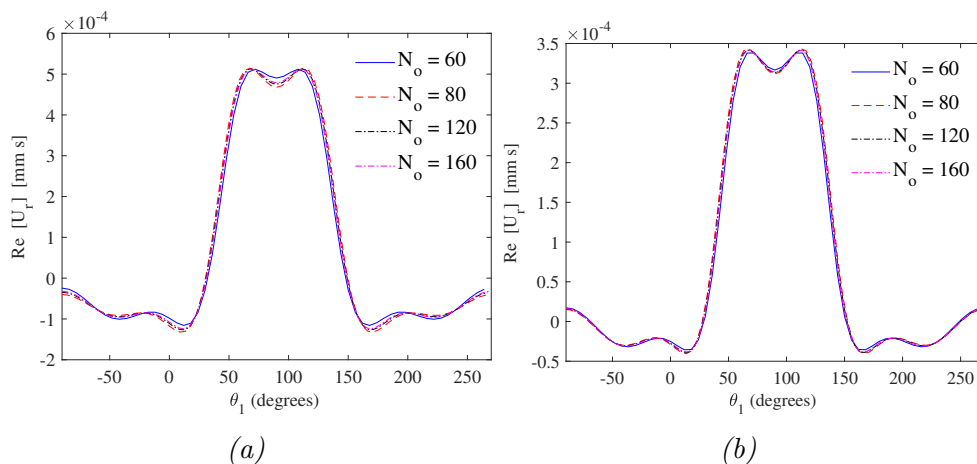


Figure C.7: Convergence tests for the real part of radial displacement frequency component ( $V = 600$  m/s) at frequencies: (a)  $f = 50$  Hz; (b)  $f = 100$  Hz

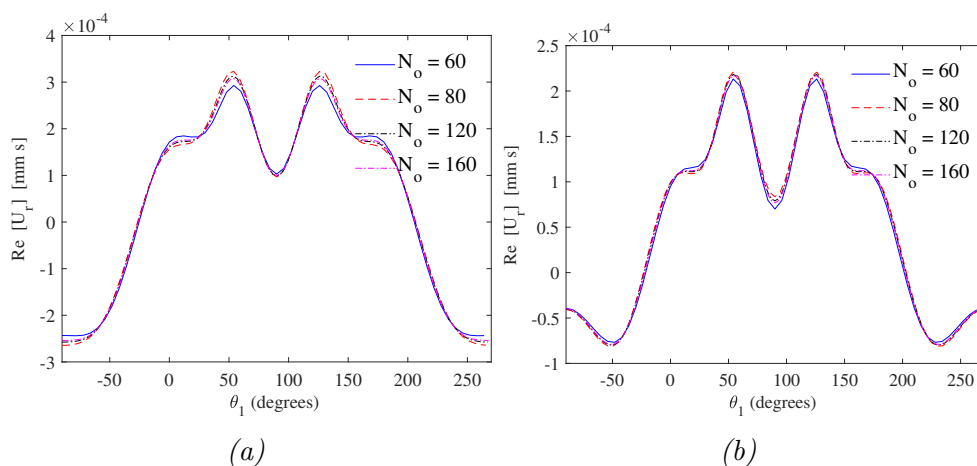


Figure C.8: Convergence tests for the real part of radial displacement frequency component ( $V = 800$  m/s) at frequencies: (a)  $f = 50$  Hz; (b)  $f = 100$  Hz

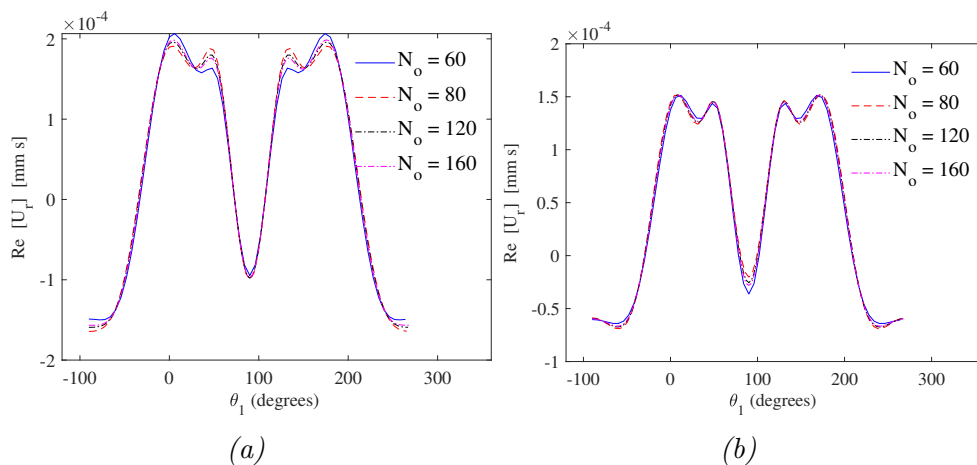


Figure C.9: Convergence tests for the real part of radial displacement frequency component ( $V = 1000$  m/s) at frequencies: (a)  $f = 50$  Hz; (b)  $f = 100$  Hz



